Elucidation of mechanisms in manganese and iron based oxidation catalysis

Angelone, Davide

Elucidation of mechanisms in manganese and iron based oxidation catalysis

Mechanistic insights and development of novel approaches applied to transition metal catalyzed oxidations catalysis

Davide Angelone

university of groningen / faculty of mathematics and natural sciences

The work described in this thesis was carried out at the Molecular Inorganic Chemistry department of the Stratingh Institute for Chemistry, University of Groningen, The Netherlands.

The work reported in this thesis was supported financially by European Research Council (ERC-2011-StG-279549).

European Research Council
Established by the European Commission

Printed by: Ipskamp Drukkers, Enschede, The Netherlands

Cover picture “The Alchymist, in Search of the Philosopher’s Stone, discovers Phosphorus” used with kind permission of the Derby Museums Trust, ©2016 Derby Museums Trust

ISBN: 978-90-367-9303-2 (printed version)

ISBN: 978-90-367-9302-5 (electronic version)

university of groningen

Elucidation of mechanisms in manganese and iron based oxidation catalysis

Mechanistic insights and development of novel approaches applied to transition metal catalyzed oxidations catalysis

PhD thesis

to obtain the degree of PhD at the
University of Groningen
on the authority of the
Rector Magnificus Prof. E. Sterken
and in accordance with
the decision by the College of Deans.

This thesis will be defended in public on

Friday 2 December 2016 at 11.00 hours

by

Davide Angelone

born on 3 July 1981
in L'Aquila, Italy

Supervisor
Prof. dr. W.R. Browne

Assessment committee
Prof. dr. J. Gerard Roelfes
Prof. dr. Christine McKenzie
Prof. dr. Maja Gruden

per Laura

In loving memory

Contents

Chapter 1

In this general introductory chapter several aspects of the theory and practice in (Resonance) Raman spectroscopy applied to molecular inorganic systems will be discussed in the context of the studies reported in this thesis. The aim is not to provide a comprehensive monograph on the subject but to prime key aspects in the mind of the reader.

1.1 Introduction

The characterisation, both of structure and electronic properties, of any molecular system is extremely important in understanding its reactivity. Beyond this, the participation of third parties (catalysts) or other environmental variables (temperature, light, solvent) in determining reactivity adds an extra level of complexity that requires characterisation. In the characterisation of structure and function, spectroscopy plays a central role.

Spectroscopy is the branch of science, which, at its simplest, involves the study of the interaction of light (or as demonstrated by Maxwell undulating electric and magnetic fields) with matter. The various types of spectroscopies can be classified by the energy of the photons or wavelengths / frequency since $E = h\nu = hc/\lambda$ (where λ is the wavelength, c is the speed of light, h is the Plank constant and ν is frequency), although there is considerable overlap between each of the spectral ranges. Each wavelength of light can interrogate a system via a specific physical mechanism that can be correlated, in some cases, to the structure of the molecules contained within the sample. However, the state of the sample is critically important, for instance the microwaves generated from a Klystron tube can be used on a solid sample or frozen solutions, containing unpaired electrons, and nested in a magnetic field (usually ~0.3 T) to measure the Electron Paramagnetic Resonance (EPR) spectrum. However, if the sample is in the gas phase and has a non-zero dipole moment, when it is subjected to a constant electric field, these same microwaves can interrogate the systems rotational energy levels and, combined with the secondary Stark effect, it is possible to obtain structural information.

The previous example is also emblematic of the critical role sample preparation plays in determining the outcome of the spectroscopic measurements. In the following section we will consider some of the most frequently used spectroscopic techniques in this thesis (UV-vis absorption and Raman spectroscopy) together with density functional theory (DFT) which has been used to rationalize the results obtained in spectroscopic studies.

1.2 Introduction to the electronic spectroscopy of Mn and Fe

The interaction of photons with energies in the visible and ultraviolet region (UV-vis) of the electromagnetic (EM) spectrum with molecules leads typically to electronic excitation; i.e. redistribution of electron density and nuclear positions within the molecule to a less stable configuration/state. The absorption bands in the visible and near UV region of metal complexes are dependent predominantly on the nature of the electronic configuration of the metal ions. Therefore the σ- and π-donor strength of the ligand, and possible back-donation, determine the presence and energy of certain transitions. For Mn(II), according to the Aufbau principle, the 3d-orbitals should be half-filled (five electrons) and hence bonding should be weak when in a high spin (sextet) state. A half-filled high spin d-orbital configuration means that d-d transitions are spin and Laporte forbidden and hence Mn(II) complexes are typically colourless save for transitions due to, e.g., π-π*, the ligands in the UV region. In contrast, Mn(III) and Mn(IV) form highly coloured complexes. In the case of Mn(III) complexes the spin state, quintet, triplet or singlet, determines the intensity and energy of electronic absorption bands and the d-d bands are generally weak (Laporte forbidden). Quintet state Mn(III) complexes have only one possible spin allowed transition in an octahedral environment (the most preferred geometry for this

oxidation state), thus only one band should be observed. In some cases the triplet state is most stable for Mn(III) and two or three weak visible bands are observed. In contrast Mn(IV) exists exclusively with quadruplet spin multiplicity, which results in a strong tendency to undergo dimerization thereby benefiting from stabilisation through antiferromagnetic interactions between the d-electrons (around 400 cm^{-1}) and hence several d-d transitions are typically observed in the visible region together with ligand-to-metal charge transfer (LMCT) transitions in the UV region. As will be discussed below and become apparent in later chapters, the predominantly metal centred visible transitions mean that resonance enhancement of Raman scattering is generally only observed upon UV excitation (i.e. into LMCT bands).

In the case of iron, three oxidation states are of most interest under ambient conditions: II, III, IV. The Fe(II) state is characterized by six d-electrons and three multiplicities: singlet, triplet, quintet. The singlet configuration (as we will see) presents two or more strong bands (metal-to-ligand charge transfer, MLCT) in the visible region, while with the triplet and quintet spin configurations the d-d transitions (and MLCT transitions) are considerably forbidden. The Fe(III) oxidation state is similarly to Mn(II), with five d-electrons and the most prevalent spin states are doublet and sextet. d^5 configurations tend usually to be high spin, which leads to forbidden d-d transitions typically in the visible region and LMCT bands in the near-UV region. In the Fe(IV) oxidation state, which is a d^4 system, the predominant spin ground state is triplet, which presents a formally d-d (but with some LMCT character) transition that is broad and relatively weak in the near IR region.

The effect of ligands on Fe and Mn complexes is both to strengthen/weaken charge transfer bands and to determine the spin state of the ions. As we will see in the following chapters, a ligand such as those based on the triazacyclononane core provides essentially only σ-bonding, which provides a strong ligand field to the complex but on the other hand does not provide a set of high energy delocalized electrons necessary to lower the energies of MLCT or LMCT bands; in contrast ligands such as N4Py (which we will meet in chapter 2) has several pyridine moieties, which provides together with a strong ligand field, a reasonably low energy LUMO that can interact with metal centred orbitals leading to low energy charge transfer bands. The CT contribution to an absorption band is, as we shall see below, important in aspects such as fluorescence and resonance enhancement of Raman scattering.

1.3 Inelastic scattering (Raman) spectroscopy

C. V. Raman was the first to report[1] the observation of the phenomenon, which is now called Raman spectroscopy, and received the 1930 Nobel Prize for physics for this discovery. Inelastic scattering of light incident on matter was predicted earlier by A. Smekal[2] and observed at the same time in solids by Landsberg and Mandelstam[3] (and hence the spectroscopy is often referred to as combinatorial scattering spectroscopy in the former Soviet Block).

The origin of Raman scattering can be understood by considering the manner in which light interacts with matter. When a photon passes through matter, one of several interactions can occur;

- If the energy of the photon satisfies the Bohr condition then its energy can be absorbed by the molecule through an electronic transition with the molecule in question entering an excited electronic state.
- If the resonance condition is not satisfied then the other most probable event is that the photon passes through the material with its path disturbed only due to refraction.
- When light interacts with particles that are much smaller in diameter than the wavelength of the light, about one photon in every ten million undergoes Rayleigh or Raman scattering. (Scattering by large spherical particles is described by Mie Theory[4]).

The extent to which Rayleigh and Raman scattering of light occurs is related to the polarizability of an entire or part of a molecule. The polarizability of a molecule can be imagined as the ability of the electron density (of a molecule) to generate a transient dipole moment induced by an (oscillating) applied electric field (incident light). It can be expressed as the amount of charge (C) that can be displaced by a certain distance (m) by a certain electric field (V/m): $C \cdot m^2 \cdot V^{-1}$. Thus, the magnitude (I_{out}) of the Rayleigh and Raman scattering is directly proportional to the square of the induced dipole moment (μ_{ind}), which is equivalent to the polarizability (α) by the incident light's electric field (**E**):[5]

$$I_{out} \propto {\mu_{ind}}^2 = (\alpha \overline{\boldsymbol{E}})^2 \quad \textbf{(Eq. 1)}$$

As a rule of thumb, a qualitative assignment of the intensity of Rayleigh and Raman scattering of particular molecules or bonds can be made on the basis of how loosely the electrons are held by the nuclei. For instance: atoms of larger atomic radius are more polarizable than smaller atoms (due to shielding of the effective nuclear charge by core electrons), and highly polar bonds are less polarizable than covalent bonds. Furthermore, polarizability is not necessarily isotropic – the ability to polarize the electron density in a bond in one direction (along the bond) is not necessarily the same as that orthogonal to the bond axis.[6] Another important variable that influences the intensity of the Rayleigh scattering is the wavelength of the incident light (λ_0), to which it shows an inverse fourth power dependence (as it is a two photon process, $h\nu_{in}$ & $h\nu_{out}$).

$$I_{out} \propto (\lambda_0)^{-4} \qquad \textbf{(Eq. 2)}$$

Although Rayleigh and Raman scattering can be considered as a single physical phenomenon because they have the same physical origin in terms of the interaction of light with matter, there is a key difference. Indeed Raman scattering should not occur if one considers the Born approximation that the nuclei of the molecules do not move during the time that the photon's energy is utilized to generate μ_{ind} before it is returned to the environment (Rayleigh scattering). The vibrations and rotations of the molecules, however, can affect the polarizability of the electrons in the molecules. For each vibrational mode of a molecule we can describe the polarizability α as the sum of the polarizability of the molecule at its energy minimum (α_0) and the change in polarizability due to the vibrational mode of interest ($\alpha_l = (\partial\alpha/\delta x)_{x=0}$) multiplied by $\cos(2\pi\, \nu_{vib}\, t)$, where ν_{vib} is the vibrational mode's frequency and t is the time.

$$\alpha = \alpha_0 + \alpha_I \cdot \cos(2\pi \cdot \nu_{vib} \cdot t) \qquad \textbf{(Eq. 3)}$$

When α_I of a vibrational mode is non zero then Raman scattering occurs at the energy of the incident light ($h\nu_0$) plus or minus the transition energy associated with the vibrational mode ($h\nu_{vib}$).

$$h(\nu_0 \pm \nu_{vib}) \qquad \textbf{(Eq. 4)}$$

The Raman scattering at higher energies than the incident light are referred to as anti-Stokes scattering, while the Raman scatters with lower energies are referred to as Stokes scattering. In figure 2 an energy diagram shows the relation between Stokes and anti-Stokes Raman scattering.

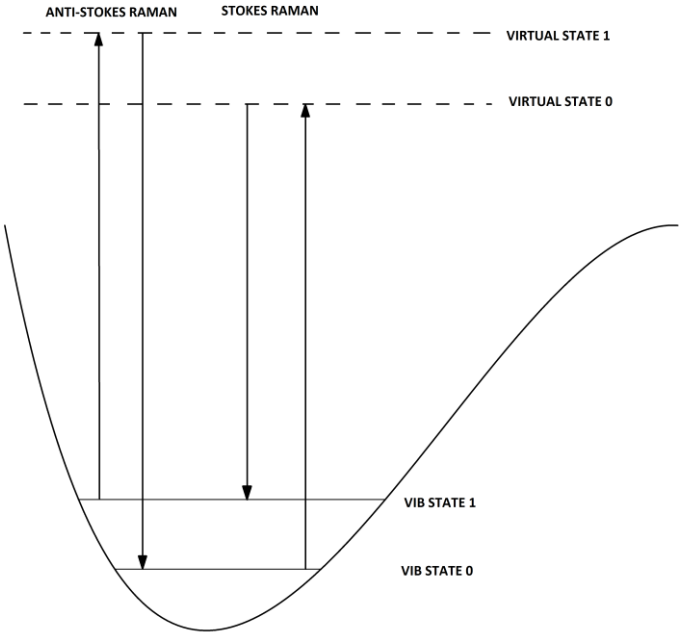

Figure 1. Origin of Stokes and anti-Stokes scattered light.

The polarizability of a molecule can be considered as a scalar, which holds for a molecule of spherical symmetry. However, if the symmetry of the molecule is non-spherical then the polarizability assumes the dimension of a 3 x 3 tensor, which represents the anisotropy of the polarizability. The symmetry of the molecule, then, assumes an important factor in determining the observed Raman scattering, since the more the electric field of the incident light ($\bar{\mathbf{E}}$) is aligned with the maximum value of the polarizability tensor of a certain vibrational mode (α_{vib}) then the greater the intensity of the inelastically scattered light will be. The latter consideration rationalizes why highly symmetric compounds usually show more intense scattering from symmetric vibrational modes than other modes (c.f. Chapter 4: $[Mn_2(\mu\text{-}O_3)(tmtacn_2)]^{2+}$ mode at 700 cm^{-1}). Another property that the polarizability anisotropy lends to Raman scattering is that each mode scatters polarized light with a polarization angle that differs from the angle of incidence of the polarized light.

1.4 Basics of Raman spectrometer design

In the previous section the physical origin of Raman scattering was discussed. How a Raman spectrum is actually acquired is in many respects as pertinent to understanding the spectra obtained. A Raman spectrometer is constituted of a monochromatic light source which, via mirrors and lenses, is focused on or in the sample and the scattered light is collected and then directed via lenses through a notch filter (to remove the more intense Rayleigh scatter) towards the entrance slits of a spectrograph where the light is dispersed and the spectrum ultimately digitized.[7] The general arrangement for a Raman spectrometer is shown in Figure 3. In the following sections, a more detailed description of each component will be given.

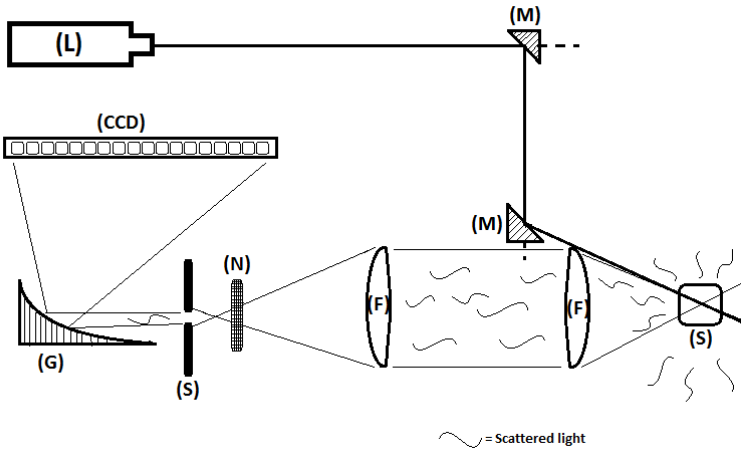

Figure 2. Schematic representation of a Raman spectrometer 135° back scattering configuration. Each component has been labelled with letters in parentheses: (L) Light source, (M) Mirror or Prism, (S) Sample, (F) Planoconvex Lenses, (N) Notch Filter, (S) Slits, (G) Monochromator/Gratings and (CCD) Array detector.

Light source (L). A monochromatic light source is essential for Raman spectroscopy as the shape and width of the laser determines the minimum width and shape of the Raman scattering bands. Typically a laser with a wavelength in the near-infrared or visible region is used, however, increasingly lasers with wavelengths in the ultraviolet region are used. The advent of diode pump solid state (DPSS) and high quality diode lasers have in large part been responsible for the burst in activity in Raman spectroscopy seen over the last two decades as these lasers are usually small and light and highly efficient in terms of power consumption.

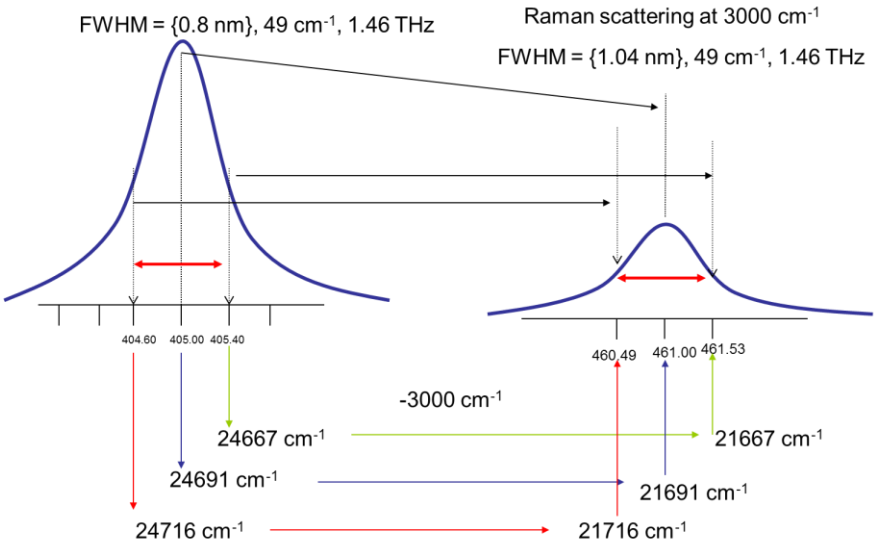

Figure 3. Importance of spectral line shape in excitation source. The light scattered at 405.00 nm will appear at 461.00 nm, but the light scattered from 404.60 nm will appear at 460.49 nm etc. The Raman scattering at 3000 cm^{-1} will appear broader in terms of wavelength but in fact will be the same FWHM in terms of energy (cm^{-1}, Hz etc) and the shape of the band will be directly related to the shape of the laser emission.

Optics (M)(F). The emitted light from the source has to be directed through the sample and the scattered light to the spectrograph, which can be achieved via mirrors (with a special coating or quartz prisms for UV) or optical fibers (mostly used in visible Raman for their versatility) made out of glass with as low as possible fluorescence. When the light reaches the sample it is usually focused via lenses at a specific point in (or on) the sample in order to have the maximum radiant energy density (or irradiance for surfaces) and be collected by overlapping of the confocal volume of the incident light with the confocal volume of the collecting lens.

Notch filter (N). One of the major challenges in Raman spectroscopy is to prevent the inelastically (Rayleigh) scattered and reflected photons from producing overwhelming reflections (stray light) within the spectrometer, which would saturate the detector. Although subtractive double and triple spectrographs were used in the past, in recent years notch filters have attained preeminence in this role.

Spectrograph (S) (G). The spectrograph is the hearth of a Raman spectrometer because it is the component in which photons of different energy are diffracted by a grating at different angles according with their wavelength. The light which enters the spectrograph diverges after it enters the slits **(S)**, and it is this point which can determine the resolution – the wider the slit the lower the resolution but the more light that enters the spectrograph. In the Czerny configuration the light diverges until it hits a convex mirror which collimates the beam as well as direct it towards the grating **(G)**. The grating has a number of ruled lines per length (expressed in grooves per millimeter) which determines its ability to disperse light and hence the achievable resolution. The refracted light is directed toward a second mirror which refocuses it again onto the detector.

Detector (CCD). The dispersed light is directed towards an array of photodiodes or nowadays more commonly a charge-coupled device **(CCD)**. Both of these technologies have a series of photosensitive epitaxial layer areas (pixels) activating diodes or transistors (MOSFETs) which

transfer the charge to a register where it is then converted into a digitized current or voltage signal, respectively. The correspondence between the pixel number and wavelength of light that strikes it is determined using reference compounds such as indene.

Confocality. An important factor that affects dramatically the intensity of the Rayleigh and Raman scattering light collected by the detector is confocality. Since the Raman scattering is a weak phenomenon it requires that the collection of light is maximised. The optical arrangement means that light from an ellipsoid (the confocal volume) is gathered only and hence the signal intensity is directly related to the spatial correspondence between this volume and the path of the laser beam.

1.5 Factors influencing the intensities of the Raman signals

Up to now we have considered only the polarization tensor as a discriminant for the intensity of a certain Raman mode but experimentally other parameters, dependent on "non-ideal" conditions, have to be considered. One of those parameters is the sensitivity of the detector at different wavelengths which is determined by the arrangement of the CCD and especially the contacts on each pixel for readout. Furthermore the absorption of the photons is a prerequisite for detection and the absorption spectrum of silicon limits the spectral sensitivity to less than 1000 nm. If the Raman window is in a region of the spectrum where the sensitivity is decreasing dramatically with increasing wavelength (Figure 5) then it is likely that even very strongly scattering modes at high wavenumber are not observed experimentally.

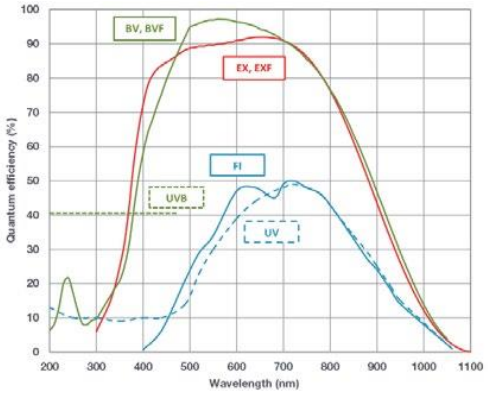

Figure 4. Spectral sensitivity of a typical CCD detector with open (blue) and back illuminated (red/green), image courtesy of Andor Technology©.

One of the major drawbacks of acquiring Stokes Raman spectra is the inherent fluorescence of both the compounds under study and the rest of the material in a sample. In cases where fluorescence occurs in the same spectral region as the Raman scattering, its broadness means that a spectrum can be obtained by baseline subtraction (via polynomial fitting). Indeed considerable effort has been applied to develop algorithms for automating this operation.[8] A limitation arises in this approach due to one of the several sources of noise in a Raman spectrum – shot noise. Shot noise is proportional to the square root of the signal intensity i.e. number of photons that strike the detector. Shot noise does not discriminate between photons arising from Raman scattering and those from fluorescence of course and hence although a baseline correction can recover a spectrum, the noise level will always be higher and hence ultimately the Raman signal will fall below the S/N floor.

A further important experimental parameter is related to the absorption of compounds in the same spectral region as the excitation beam and the Raman scattering. This absorption will lead to a decrease in both the total Raman scattering generated in the confocal volume and will attenuate the Raman signal through absorption of the exiting photons. This situation is a particular problem in resonance Raman spectroscopy (as we will see in the next section). The light incident on the sample, if absorbed, can also cause photodamage, and sample heating/burning. In the case of a spectrum where the incident light is on a steep electronic absorption band the Raman spectrum (if observable) will appear dramatically different but it can be corrected if the absorption spectrum is measured. Applying the relation between absorbance and transmittance, the intensity of the Raman spectrum can be corrected point by point. The following equation shows how to correct each point of the Raman spectrum by multiplying the measured Raman intensity by natural logarithm of the absorbance at the particular wavenumber ($\mathbf{A}_{\omega}$).

$$(\text{Real Raman intensity}) = (\text{Measured Raman intensity}) \cdot e^{A_{\omega}}$$

1.6 Resonant enhancement of Raman scattering cross-section

Experimentally there is no difference between acquisition of a Raman spectrum and a so-called resonance Raman spectrum. Indeed, it is important to underline that, as we will see in detail in the theory section, the Raman scattering is an effect related to the polarizability of a molecule or part of it, whereas resonance enhancement of the Raman spectrum is an effect that, as the word suggests, results in the Raman scattering increasing as the incident light comes into resonance with an electronic transition and results in an enhancement of the Raman scattering due to a vibrational mode coupled with that electronic transition. Sometimes vibrational modes that are not particularly intense in a non-resonant Raman spectrum are subject to a substantial enhancement under resonance with the electronic transition. An example of that can be the seen in Figure 5 in the Raman spectrum of [Fe(II)(o-phenantroline)$_3$]$^{2+}$ recorded with various excitation wavelengths.[9]

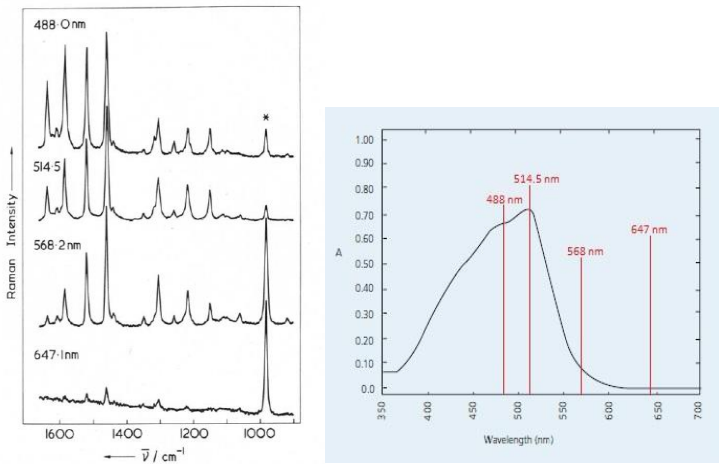

Figure 5. [left] Raman spectra of the [Fe(o-Phen)$_3$]$^{2+}$ ion, 1600-900 cm^{-1} region. Spectral slit width, 2-3 cm^{-1}. * indicates the 983 cm^{-1} reference band of the sulfate ion. [right] UV-vis absorption spectrum of the [Fe(o-Phen)$_3$]$^{2+}$ in the visible region. The vertical lines indicate the excitation wavelength used in the Raman measurements shown on the left.[9]

The spectra show that the enhancement factors can give information about the potential energy surface and geometric distortions that occur upon population of the Frank Condon excited states. It should be noted however, that in order to have meaningful results regarding the enhancement factors the spectra should be corrected for self-absorption and detector response (which differs for each region of the spectrum).[10]

1.7 Density Functional Theory

The results achieved from spectroscopic analysis of chemical systems provide normally a concrete basis for the formulation of possible modes of action or existence of labile intermediates. Theoretical methods developed over the last century could support or disprove the interpretations of experimental data via the calculation of the physical properties of the species under study.

Density Functional theory (DFT) is one of the most widely used computational methods, especially in the field of coordination chemistry, because it offers ease of usage and lower computational costs compared to ab-initio wavefunction calculations. Indeed a very computationally cheap but obsolete method such as Hartree-Fock (HF) scales (formally) by the fourth power of the basis functions (N^4) while DFT scales (formally) with the third power (N^3) and with an accuracy being compared to a second order Møller-Plesset Perturbation Theory (MP2) method.[11]

The challenge of calculating the properties of a molecule, such as thermochemistry, bond energies and distances, polarizability, orbitals' energies and shapes and so on can be achieved by solving the Schrödinger equation of the system.[12]

$$\hat{H}\Psi(\mathrm{N}_{3m}, \mathrm{r}_{3n}) = E\Psi(N_{3m}, \mathrm{r}_{3n}) \qquad \textbf{Eq. 6}$$

Where $\hat{H}$ is the Hamiltonian operator (a mathematical tool that describes the physical properties of the system), Ψ is the wavefunction that describes the system in terms of the coordinates of all 'm' electrons and 'n' nuclei in the system. Once a wavefunction Ψ satisfies the Schrödinger equation and the physical constraints,[a] by being the eigenfunction of it, all its physical properties, such as the system's energy E, of the system can be obtained. The only impediment to finding the eigenfunction Ψ is that at present there is no such analytical method to solve this problem for multielectronic systems and that is why a series of approximations are applied to the problem to obtain the closest representation of the ideal wavefunction. A now ubiquitous approximation in quantum mechanics (QM) is the Born-Oppenheimer approximation, which reduces the coordinates of nuclei to simple parameters in the wavefunction under the assumption that the substantial difference in mass between the electrons and nuclei render the nuclei relatively insensitive towards the interaction with electrons.[13] The second most important approximation in QM is definitely the Hartree Fock approximation, and, although it neglects fundamental properties of the systems (i.e. correlation between electrons), it opened

[a] The area of the squared absolute value of the wavefunction should be normalized since it represents the probability of finding an electron in a certain location and the probability over all space is unity:

$$\iiint |\Psi|^2 dx_1\, dy_1\, dz_1 \ldots dx_m\, dy_m\, dz_m = 1$$

the way to computation of multielectronic molecules. The most difficult effect to calculate in a multielectronic system is the correlation energy: the energy that stabilizes the interaction between two electrons immersed in an electronic cloud.[14] Part of this correlation energy is considered already in the exchange energy (HF) in the case of two electrons having parallel spin, often referred to as Fermi correlation, while the correlation for electrons of opposite spin is not considered in HF; it has to be addressed by considering all the possible Slater determinants (through electronic configurations) of a given molecule. Hence, it is computationally expensive to calculate accurately the energy (or other properties) of a system (molecule). Fortunately it was found (by Kohn and Sham)[15] that the electron density of a multielectronic system could be correlated by a functional (a function which accepts a function as input and gives a value as result) to the energy of the system and other descriptors. Unfortunately the perfect functional that works for every case cannot be found, but models for functionals which can address the problem within a certain accuracy are available and considering also the dynamic and Coulombic correlation in the same functional makes the calculation's duties much lighter for the computer. Functionals such as BP86 or S12g, are extremely good for calculating the ground states of molecules.

1.8 Scope and overall aim of this thesis

The overall goal of the work carried out in this thesis is to gain a deeper and fundamental insight into the nature of the reactivity of transition metal based oxidation catalysts. The approach taken in the thesis is hierarchical, beginning with consideration of the interaction of catalyst, oxidant and substrate theoretically and experimentally. In the four and fifth chapter the concept of understanding catalysis as a chemical system is developed in the study of a manganese catalyst in organic and then aqueous media. The key challenge is to appreciate the effect of feedback in chemical reactions and in the challenge of identifying the actual catalytically relevant species. In both chapters 4 and 5, Raman spectroscopy is a key asset in in-line reaction monitoring of both substrate, oxidant and, through resonance enhancement, the catalyst. Obtaining data in systems of still higher complexity, e.g., biphasic reactions, demands an alternative approach to reaction monitoring and in chapter 6 this challenge is met through the innovative use of experimental aspects of Raman spectroscopy for reaction monitoring.

Chapter outline

In chapter 2, DFT methods are applied to compare and contrast the mechanism by which a non-heme iron catalyst reacts with H_2O_2 and with NaOCl. The chapter highlights the limitations of resonance Raman spectroscopy in characterizing these novel species as well as the opportunities it presents.

In chapter 3 DFT methods are again applied together with experimental data taking into account the concentration of species and their relative rates of reactions to gain an understanding of the reaction between particular non-heme iron complexes and molecular oxygen.

In chapter 4 a combination of UV-vis absorption, resonance Raman and EPR spectroscopies were used to develop a comprehensive model for the chemistry of a well-known dinuclear Mn(IV)-TMTACN based complex in acetonitrile in the presence of carboxylic acids, alkenes and H_2O_2. The

goal of this chapter was to establish the nature of the species involved in H_2O_2 disproportionation and in alkene oxidation.

In chapter 5 attention is turned to the chemistry of this catalyst in water in the oxidation of styrene sulfonate in combination with additives. Insight into the catalytic mechanism is gained through a combination of UV/Vis absorption and (resonance) Raman spectroscopy.

In chapter 6 the challenge of obtaining inline reaction progress monitoring in two phase reactions is tackled through the use of Raman spectroscopy and flow sampling. In this chapter the approach taken and challenges overcome are discussed.

In the final chapter (7) efforts towards the synthesis of the chiral ligand TPTACN are discussed. The ultimate goal is to use manganese complexes of this ligand together with chiral carboxylic acids as a probe in combination with circular dichroism and enantioselective catalysis to establish the nuclearity of the active species towards the oxidation of alkenes.

1.9 References

[1] C. V. Raman, K. S. Krishnan, Nature, **1928**, 121, 501.
[2] A. Smekal, *Die Naturwissenschaften*. **1923**, 11, 43, 873.
[3] G. S. Landsherg, L.I. Mandelstam, *Zeitschrift fur Physik,* **1928**, 50, 769.
[4] G. Mie, *Annalen der Physik*. **1908**, 330, 3, 377.
[5] Lord Rayleigh, "On electromagnetic theory of light" *Phil. Mag*., **1881**, 12, 81.
[6] L. Silberstein, *Philos. Mag*., **1917**, 33, 92.
[7] R. L. McCreery, Raman Spectroscopy for Chemical Analysis, John Wiley &Son, **2000**.
[8] See for example: S. He, W. Zhang, L. Liu, Y. Huang, J. He, W. Xie, P. Wu, C. Du, *Anal. Methods,* **2014**, 6, 4402.
[9] D. P. Strommen, K. Nakamoto *J. Chem. Edu*., **1977**, 54, 474.
[10] T. C. Strekas, D. H. Adams, A. Packer, G. T. Spiro, *Appl. Spectrosc*., **1974**, 28, 324.
[11] D. C. Young, "Computational Chemistry: A Practical Guide for Applying Techniques to Real-World Problems.", Wiley, New York, 2001.
[12] E. Schrodinger, *Physical Review*, **1926**, 28, 6, 1049.
[13] M. Born, J. R. Oppenheimer, *Ann. Phys*., **1927**, 84, 457.
[14] E. Wigner, *Phys. Rev*., **1934**, 46, 1002.
[15] W. Kohn, L. J. Sham, *Phys. Rev. A* **1965**, 140, 4, 1133.

Chapter 2

A Computational Comparison of the Reactivity of non-Heme Fe(II) Complexes with NaOCl and H_2O_2.

Over the last decades, the involvement of Fe(III)-hypohalite, peroxido and hydroperoxido complexes in a myriad of essential enzyme catalysed halogenation and oxygenation reactions has been established and are central to the biosynthesis of natural products and antibiotics and in post translational modification of proteins. The dearth of spectroscopic data available on such hypohalite species, however, precludes their identification in biological systems and is in marked contrast to the body of data available on hydroperoxido species. Recently, our group reported the generation and spectroscopic characterization of nonheme Fe(III)-hypohalite intermediates of possible relevance to iron halogenases and demonstrated that Fe(III)-OCl polypyridyl amine complexes can be sufficiently stable at room temperature to be characterized by a UV/Vis absorption, resonance Raman and EPR spectroscopy and cryoESI-MS. In the present chapter, DFT methods are applied to rationalize the pathways to the formation of these Fe(III)-OCl, and ultimately Fe(IV)=O, species and provide indirect evidence for a short-lived Fe(II)-OCl intermediate. The species observed and the pathways involved are compared and contrasted with the related isoelectronic species generated from hydrogen peroxide.

This chapter was published in part in: A. Draksharapu, D. Angelone, M. G. Quesne, S. K. Padamati, L. Gómez, R. Hage, M. Costas, W. R. Browne, S. P. de Visser, *Angew. Chem., Int. Ed*. **2015**, *54*, 4357–4361.

2.1 Introduction

Halogenation of organic substrates, although relatively rare compared with oxygenation, is a central process in the biosynthesis of many natural products, and in the post translational modification of proteins;[1] typically these reactions are achieved by the activation of otherwise inert C-H bonds. Hence these reactions have attracted attention as they are of immediate interest and relevance to medicinal chemistry and biotechnology. Nature achieves halogenation by hijacking peroxidases and oxygenases to generate (vanadium and heme dependent) haloperoxidases and (non-heme Fe(II) dependent) halogenases, which use H_2O_2 and O_2, respectively.[2,3] The precise operation of this wide range of enzymes is of interest for biology and for the application of biomimetic complexes in C–H activation.

Nonheme iron halogenases have been proposed to react via radical pathways by transferring halide atoms ($X^{\bullet}$), whereas haloperoxidases use X^+ in electrophilically.[1c,3b,4] For example, in the case of the heme haloperoxidases the reaction proceeds via formation of an Fe(IV)=O species, which reacts with a halide anion to form an Fe(III)–OX complex.[1c] The OX^- formed can react directly or dissociates and is protonated to generate HOX near an enzyme bound substrate. In contrast, non-heme iron dependent halogenases are generally considered to generate Fe(IV)=O species, which engage in hydrogen abstraction from alkanes, with chlorination via the transfer of an iron bound chlorine atom equivalent.

Despite these mechanistic frameworks, major gaps remain in our understanding of their catalytic mode of action because of the rarity and the lack of spectroscopic data on species formed during such cycles. The transient nature and especially low steady state concentrations of the proposed reaction intermediates formed during enzyme catalyzed halogenation, such as Fe(II)-OCl, Fe(III)-OCl and, to a lesser extent, Fe(IV)=O, present a considerable challenge to their characterization and hence biomimetic model complexes are essential to the elucidation of the nature of these intermediates.[5] The intermediacy of related Fe(III)-O-IPh species is, however, precedent in the work of McKenzie and coworkers,[6a] and Nam and coworkers[6b,c] whereby the former study included the characterization of the intermediate by crystallography. A heme-Fe(III)-hypohalite was reported by Fujii,[7] Woggon[8] and coworkers, and Banse and coworkers made a tentative assignment of an intermediate as an Fe(II)-OCl species.[9] However, further than these data, the absence of spectroscopy on such species is in strong contrast to the wealth of data assembled regarding heme and nonheme high-valent Fe(IV)=O complexes.[10] This paucity of spectroscopic data limits our ability to identify such species under biologically relevant conditions and evaluate their kinetic competence in halogenations and hence the identification for the first time of the formation of a biomimetic nonheme iron(III)-hypohalite complex, i.e. $[Fe(III)(OX)(MeN4Py)]^{2+}$ (where MeN4Py = 1,1-di(pyridin-2-yl)-*N*,*N*-bis(pyridin-2-ylmethyl)ethanamine and X = Cl or Br) represented a breakthrough.[11] In our recent experimental study it was shown that iron(III)-hypohalite complexes form readily in water at low pH from $[Fe(II)(OH_2)(MeN4Py)]^{2+}$ (Scheme 1)[12,13] when reacted with NaOCl or NaOBr at room temperature. The Fe(III)-OX species was found to undergo subsequent slower conversion to a relatively stable Fe(IV)=O analogue over several minutes.

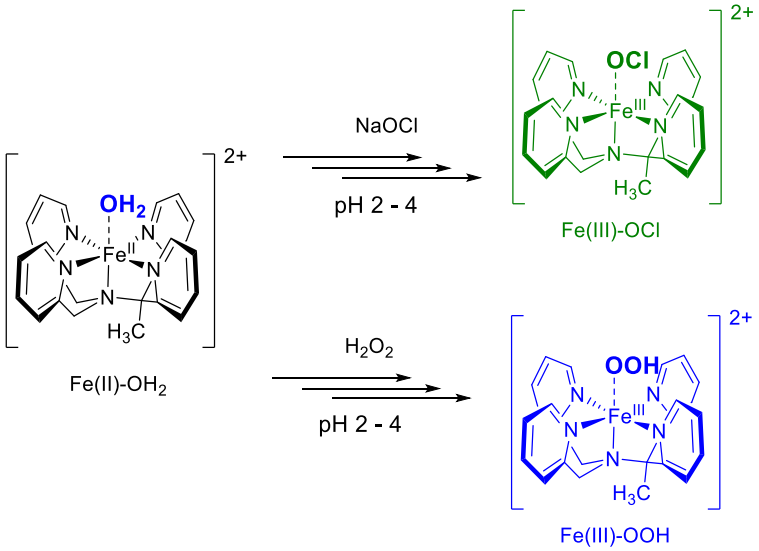

Scheme 1 Formation of $[Fe(III)(OCl)(MeN4Py)]^{2+}$ and $[Fe(III)(OOH)(MeN4Py)]^{2+}$ from $[Fe(III)(OH_2)(MeN4Py)]^{2+}$.

Before discussing computational characterization of this system it is useful to consider the experimental evidence for the formation and loss of the Fe(III)-OCl species. The UV/Vis absorption spectrum of $[Fe(III)(OH_2)(MeN4Py)]^{2+}$ exhibits visible absorption (^{1}MLCT) bands at ca. 387 and 490 nm (Figure 1a), between pH 1 and 6.[12b] Oxidation to $[Fe(IV)(O)(MeN4Py)]^{2+}$ with it characteristic NIR absorption band, NMR spectrum and resonantly enhanced Fe(IV)=O stretching band in its Raman spectrum is observed upon addition of either of the 2-electron oxidants H_2O_2 or HOCl in excess. These changes are consistent with observations made earlier by Banse and coworkers in the reaction of related Fe(II) complexes with NaOCl.[9]

The visible absorption bands of $[Fe(II)(OH_2)(MeN4Py)]^{2+}$ disappeared upon addition of 0.5 equiv. of NaOCl (at pH 2.9) without a significant concomitant increase in absorption at longer wavelengths, e.g., of $[Fe(IV)(O)(MeN4Py)]^{2+}$ (Figure 1), and the formation of the one-electron oxidized complex Fe(III)-OH,[12b,c] was apparent from the weak absorption band at ca. 480 nm and the characteristic EPR spectrum of a low spin Fe(III) complex (Figure 1a, inset), i.e. $[Fe(III)(OH)(MeN4Py)]^{2+}$.[12c] Addition of a further 0.5 equiv. of NaOCl (Figure 2a) resulted in an increase in absorbance at 480 nm (ε = >500 $M^{-1}.cm^{-1}$)[14] followed by a decrease together with a concomitant increase in absorbance at 670 nm (Figure 2b). The latter absorbance is due to $[Fe(IV)(O)(MeN4Py)]^{2+}$.

The intermediate species was assigned as $[Fe(III)(OCl)(RN4Py)]^{2+}$, based on ESI-MS, its resonantly enhanced Fe-O and O-O and O-Cl stretching modes in the Raman spectrum at 473 nm at 580, 653 and 673 cm^{-1} and the rhombic Fe(III) S = ½ signal at 77 K (e.g., 2.17, 2.12 and 1.98 for $[Fe(III)(OOH)(N4Py)]^{2+}$.[13]

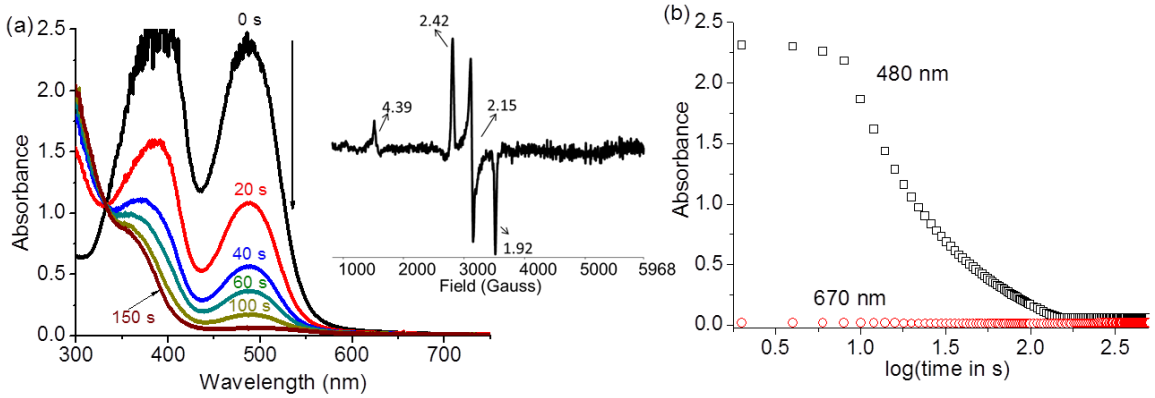

Figure 1 (a) UV/Vis absorption spectrum of $[Fe(II)(OH_2)(MeN4Py)]^{2+}$ (0.5 mM) at pH 2.2 at noted time intervals after addition of 0.5 equiv. of NaOCl at room temperature; inset EPR spectrum obtained from a flash frozen (to 77 K) sample taken at 300 s after addition of NaOCl. (b) Change in absorbance at 480 and 670 nm with log(time). Reproduced from ref [11] with permission. Copyright Wiley (2015).

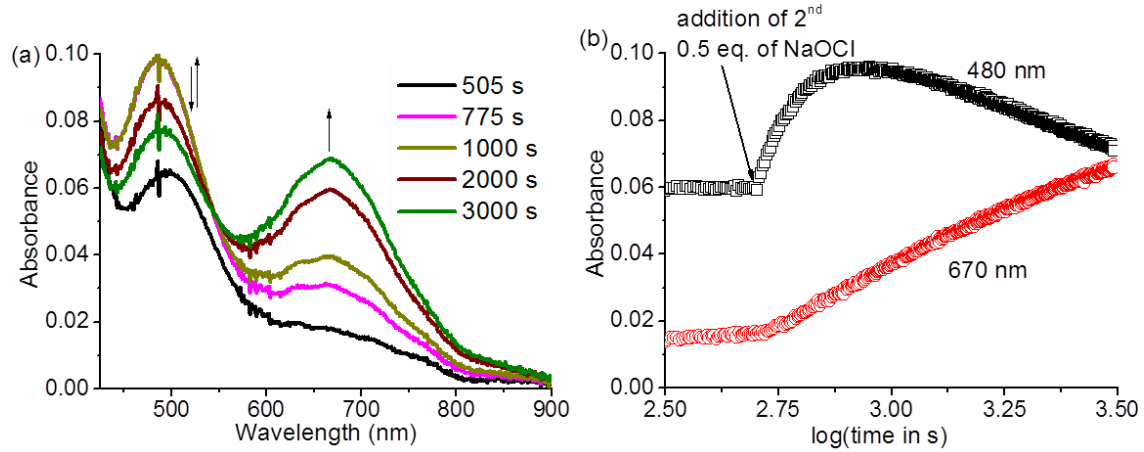

Figure 2 (a) UV/Vis absorption spectrum of $[Fe(II)(OH_2)(MeN4Py)]^{2+}$ (0.5 mM) at pH 2.2 upon addition of a 2nd 0.5 equiv. of NaOCl at room temperature. (b) Change in absorbance at 480 and 670 nm with log(time). Reproduced from ref [11] with permission. Copyright Wiley (2015).

It was apparent from the time dependence of the changes in the UV/Vis absorption spectrum that $[Fe(III)(OCl)(MeN4Py)]^{2+}$ does not form directly upon oxidation of $[Fe(II)(OH_2)(MeN4Py)]^{2+}$ but instead from a relatively slow ligand exchange between the Fe(III)-OH complex and NaOCl. [11,15] The formation of the Fe(III)-OCl species is followed by a slower reaction in which homolysis of the O-Cl bond occurs to yield the relatively stable Fe(IV)=O species. The formation and reactivity of this intermediate Fe(III)-OCl species was confirmed by a combination of cryo-ESI-MS, EPR and resonance Raman spectroscopy.

In this chapter a theoretical analysis and comparison of the reactions between $[Fe(II)(OH_2)(MeN4Py)]^{2+}$ and the isoelectronic 2-electron oxidations H_2O_2 and HOCl is made. In particular the pathways followed to the formation of $[Fe(III)(OX)(MeN4Py)]^{2+}$ species (where OX = OCl or OOH) and the relative ease of homo- and hetero-lytic bond cleavage to form Fe(IV)=O species is explored. The goal of the present study is to determine the relative energies of the various possible spin states of the species proposed to be involved in these reactions and to use calculation of resonance enhancement of their Raman spectra to understand more deeply the electronic structure of the species. These data are essential as a basis for constructing reasonable models for the reactions that take place and in particular alternative pathways.

2.2 Results

Computational studies were performed to gain insight into the electronic features of the complexes and the reaction mechanisms involved in the formation and decomposition of the Fe(III)-OOH and Fe(III)-OCl species. Each structure described here was found through a full geometry optimization and characterized as a local minimum with a frequency calculation. To assist with the interpretation of experimental resonance Raman spectra (rR), we also calculated Raman spectra from the frequency calculations.

DFT calculations on species formed from 1 and 2 in water in Fe(II) and Fe(III) state

The calculation of energy and spin states was begun with an initial survey of functionals. Double hybrid density functionals were found to provide a good description of the equilibrium between HS and LS forms of the Fe(II)-OH_2 complexes, however, as a starting point the actual species present under reaction conditions need to be considered, i.e. Fe-OH_2 or Fe-OH. As the pH used in the HOCl reactions was below 4.5, the Fe(II)-OH_2 species was considered while the Fe(III)-OH (pKa = 1.9)[12b] species is more relevant since the pH used was > 2.3. Calculation on the Fe(II)(CH_3CN) complex shows that it is much more stable than the aqua complexes, consistent with the observation that addition of even 1% by volume of CH_3CN is sufficient to return the complex to the Fe(II)(CH_3CN) state. In this section the energies of various spin states of the species of relevance to the reactions of **1** and **2** with NaOCl and with H_2O_2 are discussed and in particular the prediction of resonance enhancement, as it is a key tool in speciation studies.

DFT calculations on [Fe(IV)(MeN4Py)=O]$^{2+}$

The [Fe(IV)(MeN4Py)=O]$^{2+}$ species was prepared and isolated through chemical oxidation of [Fe(II)(MeN4Py)OH_2]$^{2+}$ in water under acidic conditions.[16] The UV/Vis absorption spectrum shows a characteristic band at 680 nm and its Raman spectrum at λ_{exc} 785 nm and at λ_{exc} 473 nm show resonant enhancement of the [Fe(IV)(MeN4Py)=O]$^{2+}$ stretching mode with the expected $^{16/18}$O isotope shift from 843 to 807 cm^{-1}; i.e. a 36 cm^{-1} shift, which is in good agreement with the calculated shift (37 cm^{-1}), using a two atom approximation. The triplet spin state of [Fe(IV)(O)(MeN4Py)]$^{2+}$ was calculated to be 8.7 kcal/mol more stable than the quintet, while the singlet state lies at far higher energy (31.4 kcal/mol above the triplet state). Hence, for thermodynamic reasons calculation of rRaman spectra for higher spin states was not attempted.

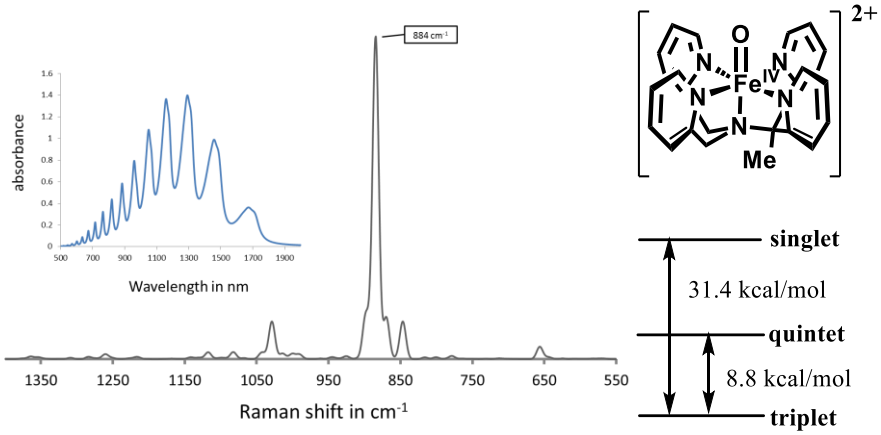

Figure 3 Left: DFT-calculated rR spectrum of the Fe(IV)=O (triplet) species (excited at 911 nm). The mode that shows the greatest degree of enhancement is at 884 cm^{-1} with a mode enhanced to a lesser extent at 845 cm^{-1} (inset: calculated absorption spectrum). The former mode involves primarily an Fe-O stretching displacement. Right: structure and relative spin states free energies.

DFT calculations on [Fe(III)(MeN4Py)-OOH]$^{2+}$

The characterization Fe(III)-OOH species was already reported for RN4Py complex.[17] Roelfes et al. assigned for the [Fe(III)(N4Py)-OOH]$^{2+}$, by rR (λ_{exc} 647.1 nm), a O-O stretching vibration at 790 cm^{-1} and a Fe-O vibrational mode at 632 cm^{-1}. The calculated results instead propose a O-O stretching found at 753 cm^{-1} and a backbone Fe-N vibration at 861 cm^{-1} but the Fe-O stretching appears to be only at 608 cm^{-1} and seems to be enhanced at λ_{exc} 572 nm only (Figure 6). The vibrational modes are underestimated due to the harmonic approximation and the fact that calculations were carried out in the gas phase.

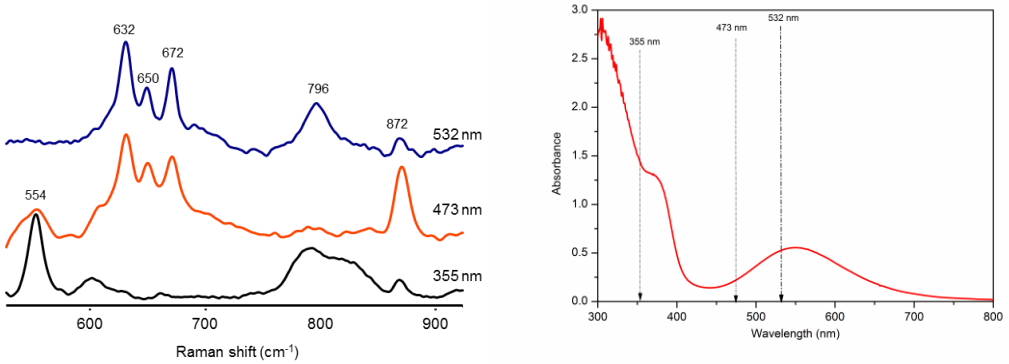

Figure 4 (left) Resonance Raman spectra at various excitation wavelengths of 1 (1 mM) in methanol after addition of 50 equiv. H_2O_2. (right) the corresponding UV/vis absorption spectrum.

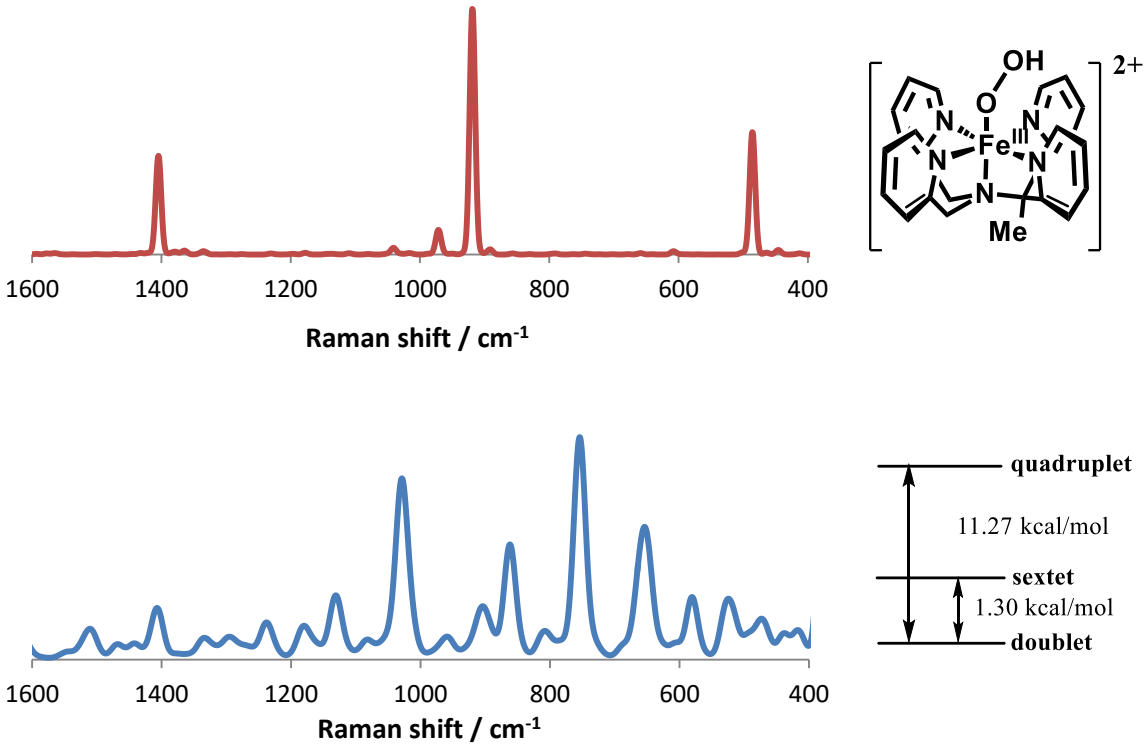

Figure 5 Left: DFT-calculated Resonance Raman spectra of the sextet (red spectrum) and doublet (blue spectrum) spin states of [Fe(III)(MeN4Py)-OOH]$^{2+}$ calculated respectively at 312 nm and 355 nm excitation. Right: structure of the [Fe(III)(MeN4Py)-OOH]$^{2+}$ species and the relative spin states free energies.

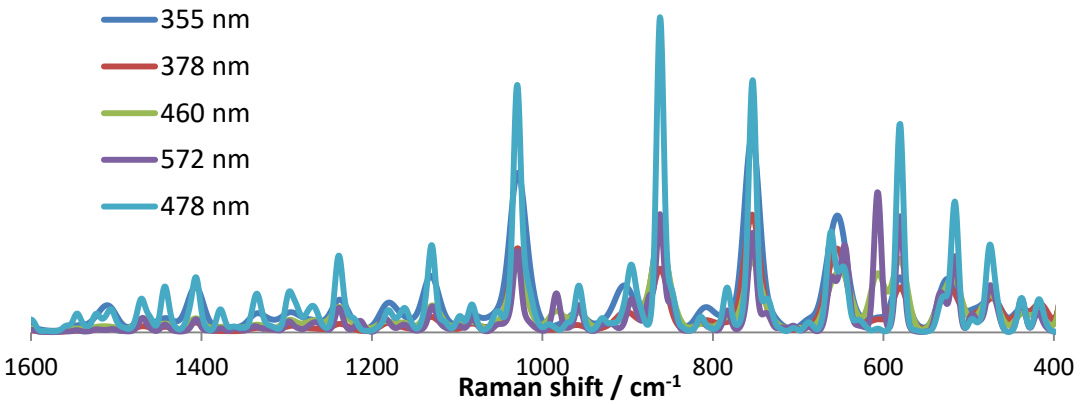

Figure 6 Resonance enhancement DFT simulation of $[Fe(III)(MeN4Py)\text{-}OOH]^{2+}$ at various excitation wavelength: 572 nm (violet), 478nm (azure), 460 nm (green), 378 nm (red) and 355 nm (blue).

The ground spin state of this species is the doublet (Figure 4), however the difference in the free energies (under normal conditions) between the sextet and doublet is only 1.3 kcal/mol in favour of the doublet. The small difference between the high and low spin energies required that both are calculated since the resonance Raman spectrum is likely a representation of either a combination or only one of the two molecular electronic configurations.

DFT calculations of $[Fe(III)(MeN4Py)\text{-}OH]^{2+}$

Calculation of the energies of the various states of the $[Fe(III)(MeN4Py)\text{-}OH]^{2+}$ species is limited by the difficulty in observing the species by resonance Raman spectroscopy. The reason for the lack of enhancement is probably due to the equilibrium between low and high spin states. The calculated free energy difference under normal conditions (SATP) between doublet and sextet is 1.34 kcal/mol. The difference between those two spin states is probably small enough that minor small environmental changes (temperature or pH) are enough to switch the relative abundance of the doublet in solution, which seems to give a stronger enhancement of the Fe-ligands modes. Amongst the enhancement bands, calculated for excitation at 330 nm for the doublet spin state are the a O-H bending mode (859 cm^{-1}), an Fe-O stretching mode at (640 cm^{-1}), and Fe-N(amino) stretching mode (577 cm^{-1}).

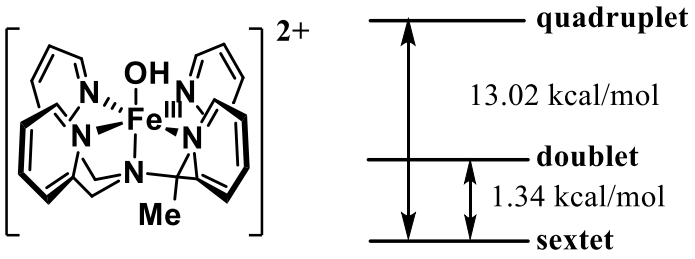

Figure 7 Structure of the Fe(III)-OH MeN4Py complex (left). Relative spin states free energies (right).

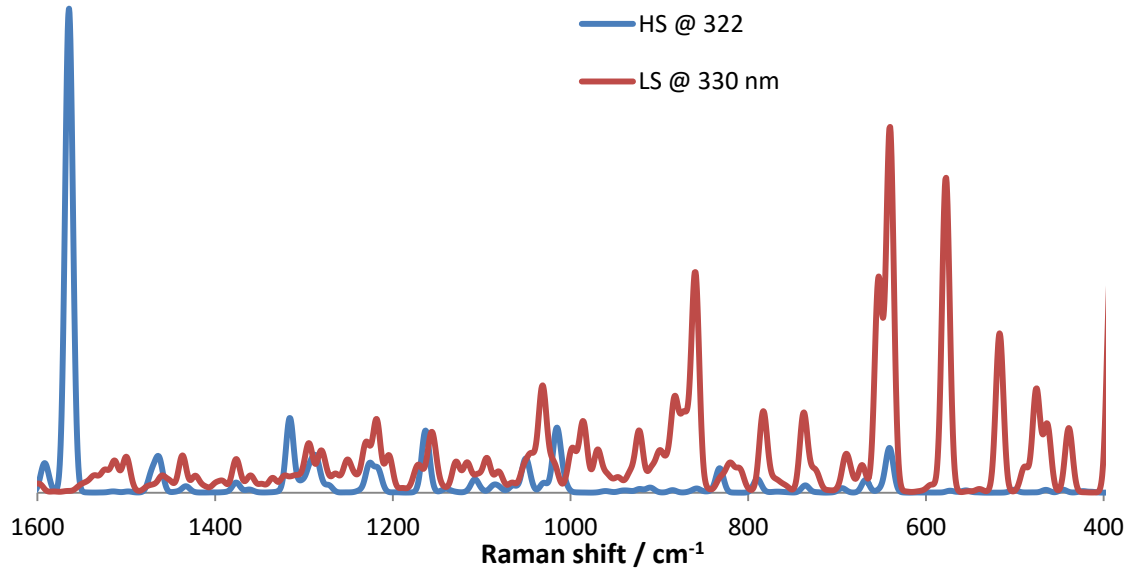

Figure 8 Resonance Raman DFT simulation of [Fe(III)(MeN4Py)-OH]$^{2+}$. The sextet (blue line) and the doublet (red line) were both simulated around the 355 nm region.

DFT calculations of [Fe(III)(MeN4Py)-OCl]$^{2+}$

The intermediacy of the [Fe(III)(MeN4Py)-OCl]$^{2+}$ species means that only resonance Raman data can be obtained for this complex (i.e. since it cannot be isolated in concentrated or solid form then a non-resonant Raman or IR spectrum is not available). A shift of the bands of [Fe(III)(OCl)(MeN4Py)]$^{2+}$ from 653 and 580 cm^{-1} to 628 and 562 cm^{-1}, respectively, was observed experimentally upon ^{18}O labelling. The observed shift of 25 and 18 cm^{-1}, respectively, are close to those expected for an Fe-O bond (29 cm^{-1}) and O-Cl (23 cm^{-1}) modes. The former band is characteristic for an Fe-O stretching mode and the latter that of an O-Cl stretching mode.[7] Notably, the band at 673 cm^{-1} is unperturbed by the use of Na^{18}OCl but undergoes a shift (from 673 to 676 cm^{-1}) when NaOBr was used[18] (Figure 9), which is consistent with the assignment of the band as a symmetric Fe-O-Cl bending mode.

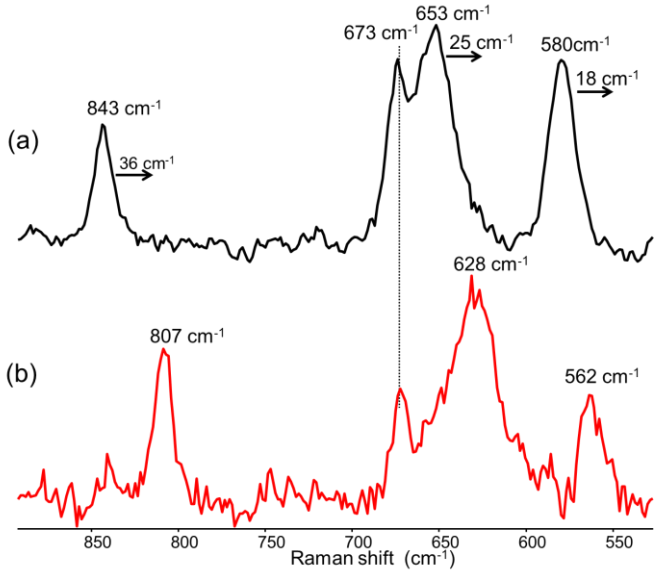

Figure 9 Resonance Raman spectra at λ_{exc} 473 nm of intermediates generated upon the reaction of [(MeN4Py)Fe(II)(Cl)]Cl (4 mM at pH 2.2) with (a) $Na^{16}OCl$ in $^{16}OH_2$ and (b) $Na^{18}OCl$ in $^{18}OH_2$. Reproduced from ref [11] with permission. Copyright Wiley (2015).

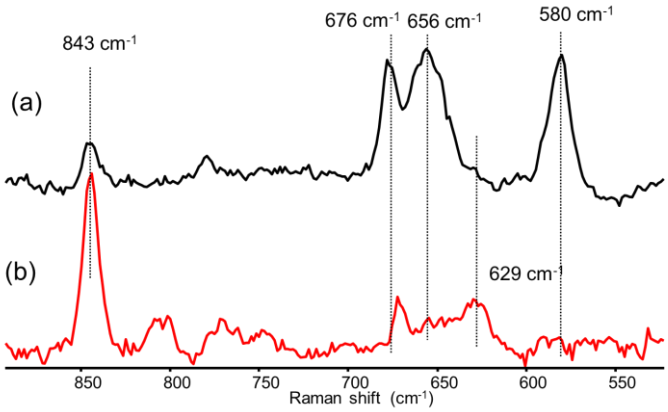

Figure 10 Resonance Raman spectra of [(MeN4Py)Fe(II)(Cl)]Cl (4 mM in H_2O at pH 2.2) with (a) NaOCl and (b) NaOBr at λ_{exc} 473 nm. Reproduced from ref [11] with permission. Copyright Wiley (2015).

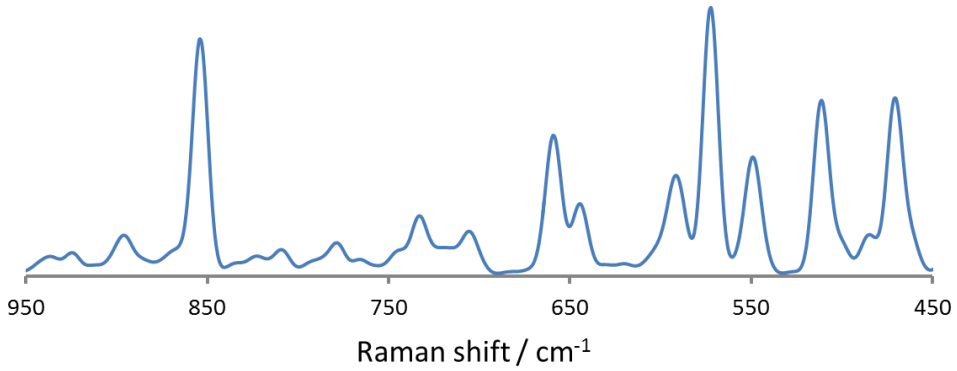

Figure 11 Simulation of the rR spectrum of the Fe(III)-OCl species (excitation at 502 nm). The modes that show the greatest degree of enhancement are: 549 cm^{-1} (O-Cl stretching mode), 572 cm^{-1} (N_{amino}-Fe stretching mode), 592 cm^{-1} (Fe-O-Cl Bending mode), 644 cm^{-1} (symmetric Py-Fe breathing), 658 cm^{-1} (Py ring breathing with minor influence of the OCl moiety), 853 cm^{-1} (N_{amino} bending mode).

The resonance Raman spectrum of [Fe(III)(OCl)(MeN4Py)]$^{2+}$ was calculated by DFT methods (Figure 11). The calculated spectrum shows that although these modes involve a larger part of the complex than the Fe-O-Cl core, the assignment of bands to Fe-O-Cl stretching and bending vibrations is, to a first approximation, reasonable.

In summary, the calculated resonance Raman spectra give only a qualitative description of the system but nevertheless support that the validity of the calculation of the spin state ordering, which is a prerequisite for correct description of reaction mechanisms.

Reaction of [Fe(II)(OH$_2$)(MeN4Py)]$^{2+}$ with H$_2$O$_2$ and HOCl

The formation of the [Fe(III)(OOH)(MeN4Py)]$^{2+}$ and [Fe(III)(OCl)(MeN4Py)]$^{2+}$, and thereafter [Fe(IV)(O)(MeN4Py)]$^{2+}$, upon reaction of [Fe(II)(OH$_2$)(MeN4Py)]$^{2+}$ with H_2O_2 and with NaOCl, respectively, in water[11] was confirmed spectroscopically and is proposed to occur in organic solvents also.[17a] DFT calculations were carried out using models and methods benchmarked and calibrated earlier[19] to provide insight into free energy changes (relative to [Fe(II)(OH$_2$)(MeN4Py)]$^{2+}$, labelled ^{5}**A** in the schemes below for each of the proposed steps in the mechanism that leads to the formation of the Fe(III)-OOH (^{6}**D**) or Fe(III)-OCl (^{6}**D***) and, ultimately, the Fe(IV)=O (^{3}**E**) complexes.

Ligand exchange and initial formation of [Fe(IV)(O)(MeN4Py)]$^{2+}$

The overall mechanism by which these species form is summarised in Scheme 2. The initial step, displacement of water by H_2O_2 and by NaOCl is rapid, consistent with the large driving force calculated for each process. However, the formation of a Fe(IV)=O species has not been observed experimentally, which is understandable considering the extremely large driving force for this latter heterolysis step. Indeed, although the activation barriers to these latter reactions has not been calculated, the reactions are highly exergonic (ca. 30 kcal mol^{-1}), driven largely by the formation of the energetically stable species (OH^- and Cl^-).

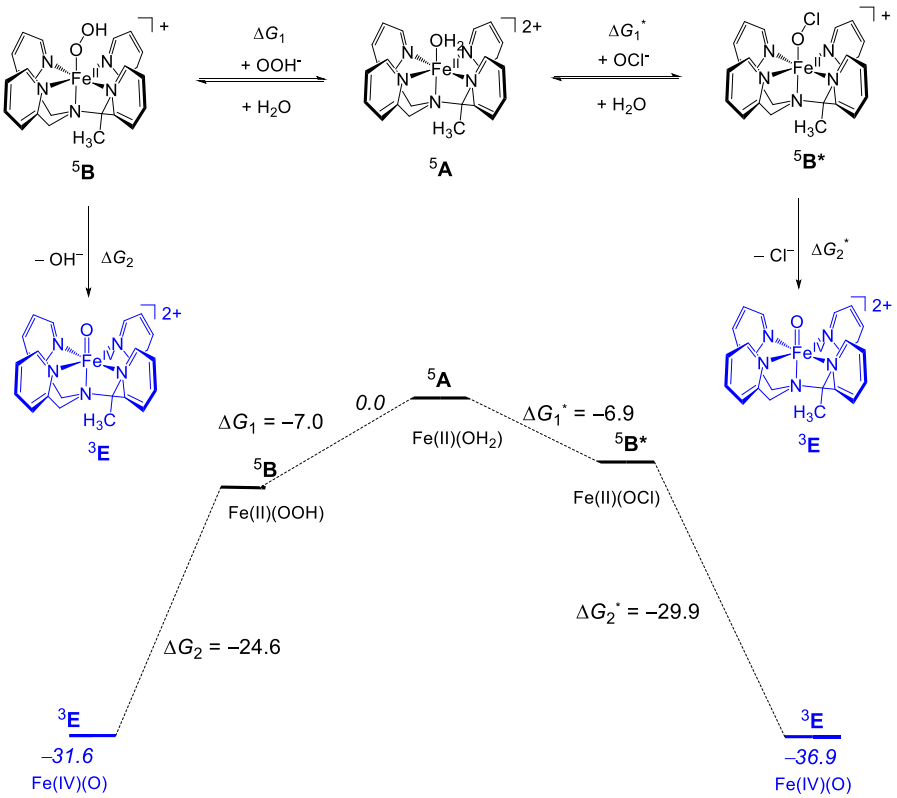

Scheme 2 Reaction scheme showing the formation and decomposition of $[Fe(II)(OOH)(MeN4Py)]^{2+}$ and $[Fe(II)(OCl)(MeN4Py)]^{2+}$ to $[Fe(IV)(O)(MeN4Py)]^{2+}$ and calculated free energies for each step. Data includes dispersion, entropic and solvent corrections and is given in kcal mol^{-1}.

Comproportionation of $[Fe(IV)(O)(MeN4Py)]^{2+}$ with $[Fe(II)(OH_2)(MeN4Py)]^{2+}$

The $[Fe(IV)(O)(MeN4Py)]^{2+}$ formed will, in each case, comproportionate rapidly with $[Fe(II)(OH_2)(MeN4Py)]^{2+}$, a reaction which is most likely diffusion limited (Figure 11) and is also calculated to have a large driving force.

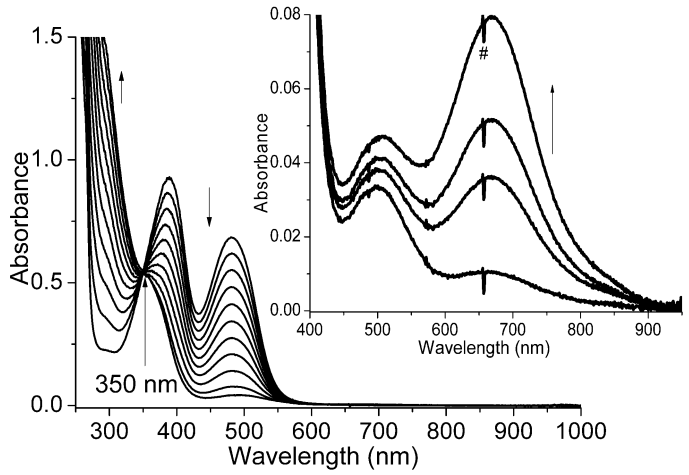

Figure 11 Addition of an aqueous solution of $[(MeN4Py)Fe(IV)(O)](PF_6)_2$ (2 mM, 10 µL per addition) to an aqueous solution of $[(MeN4Py)Fe(II)(CH_3CN)](ClO_4)_2$ (0.25 mM, 1 mL, with stirring) in water (inset: addition of 1 equiv of $[(MeN4Py)Fe(IV)(O)](PF_6)_2$ results in complete disappearance of the absorption bands of the iron(II) complex, further addition of $[(MeN4Py)Fe(IV)(O)](PF_6)_2$ leads to an increase in its characteristic absorption at 670 nm). Spectra are corrected for dilution.

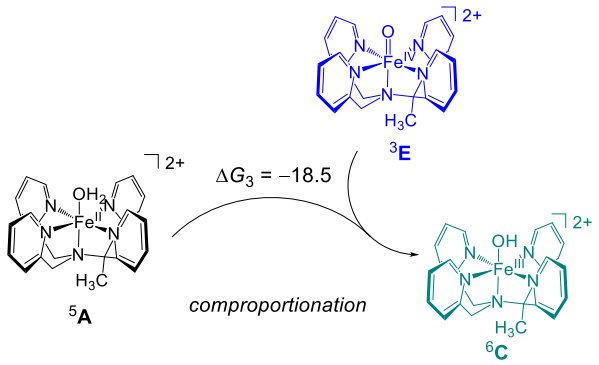

Scheme 3 Comproportionation between [Fe(II)(OH)(MeN4Py)]$^{2+}$ and [Fe(IV)(O)(MeN4Py)]$^{2+}$ and calculated free energies for the reaction. Data includes dispersion, entropic and solvent corrections and is given in kcal mol^{-1}.

Ligand exchange and initial formation of [Fe(III)(OH)(MeN4Py)]$^{2+}$

The reaction between the Fe(III)-OH complex (^{6}**C**) formed and H_2O_2 was calculated to be mildly exergonic (7.0 kcal mol^{-1}), while in contrast the reaction with NaOCl is endergonic (7.0 kcal mol^{-1}). Nevertheless, in both cases the build-up of the Fe(III)-OX species (X = -OH or -Cl) is facilitated by the subsequent highly endergonic homolytic cleavage step (15 and 20.7 kcal mol^{-1}, respectively) that converts the Fe(III)-OOH (^{6}**D**) and Fe(III)-OCl (^{6}**D***) to the Fe(IV)=O species (^{3}**E**). Indeed both species can be observed transiently in solution. The absence of detectable amounts of Fe(III)-OCl above pH 5 (*i.e.* where the concentration of OH^- becomes significant) is in agreement with the conclusion that Fe(III)-OH (^{6}**C**) is in equilibrium with Fe(III)-OOH (^{6}**D**) and Fe(III)-OCl (^{6}**D***) are in equilibrium with each other. Indeed, reaction of the Fe(III)-OH complex ^{6}**C**, prepared independently, with H_2O_2 or NaOCl shows that the Fe(III)-OX species form rapidly to reach an equilibrium with Fe(III)-OH more rapidly than they convert to [Fe(IV)(O)(MeN4Py)]$^{2+}$.[11] The overall reactions are summarized in Schemes 5 and 6 below.

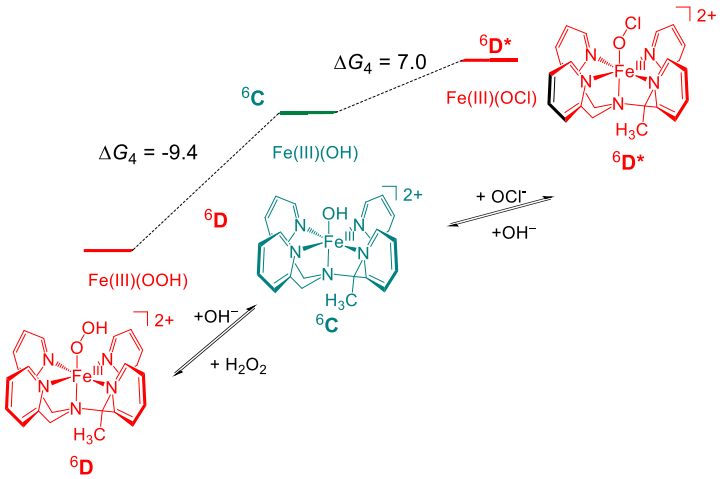

Scheme 4 Reaction scheme showing the formation of and relation between [Fe(III)(OOH)(MeN4Py)]$^{2+}$ and [Fe(III)(OCl)(MeN4Py)]$^{2+}$ and calculated free energies for each step. Data includes dispersion, entropic and solvent corrections and is given in kcal mol^{-1}.

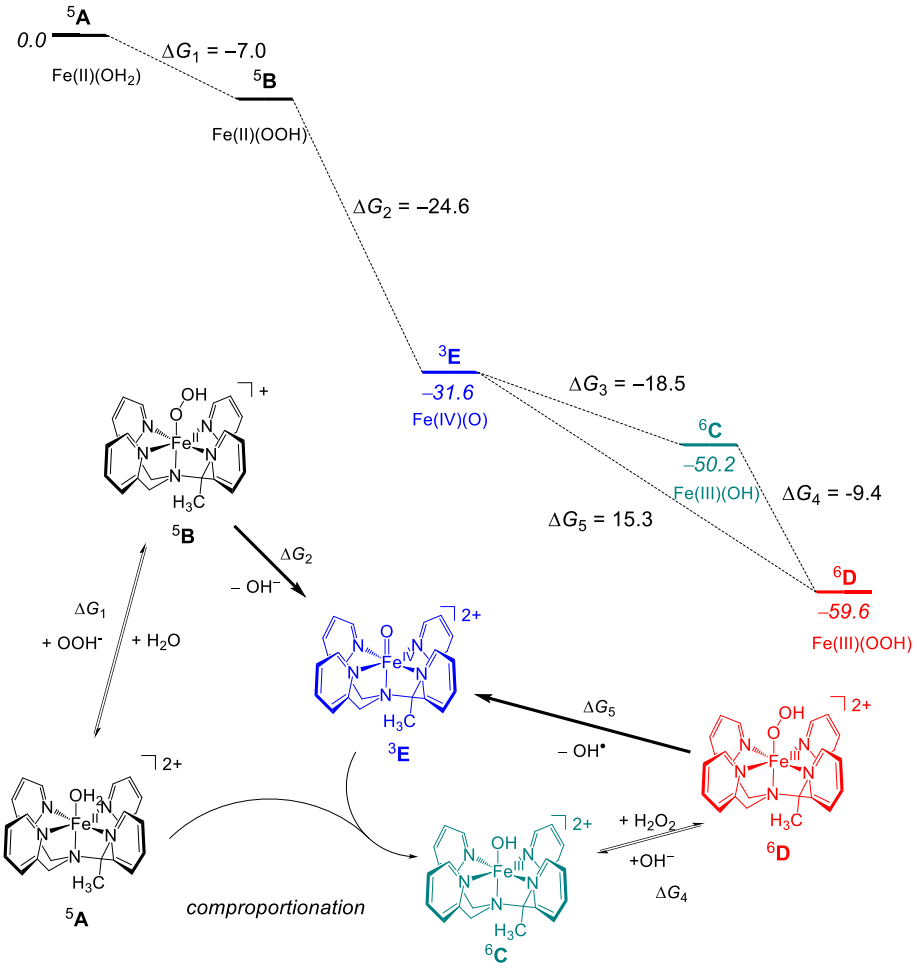

Scheme 5 Reaction scheme showing the formation of and relation between $[Fe(III)(OOH)(MeN4Py)]^{2+}$ and $[Fe(IV)(O)(MeN4Py)]^{2+}$ and calculated free energies for each step. Data includes dispersion, entropic and solvent corrections and is given in kcal mol^{-1}.

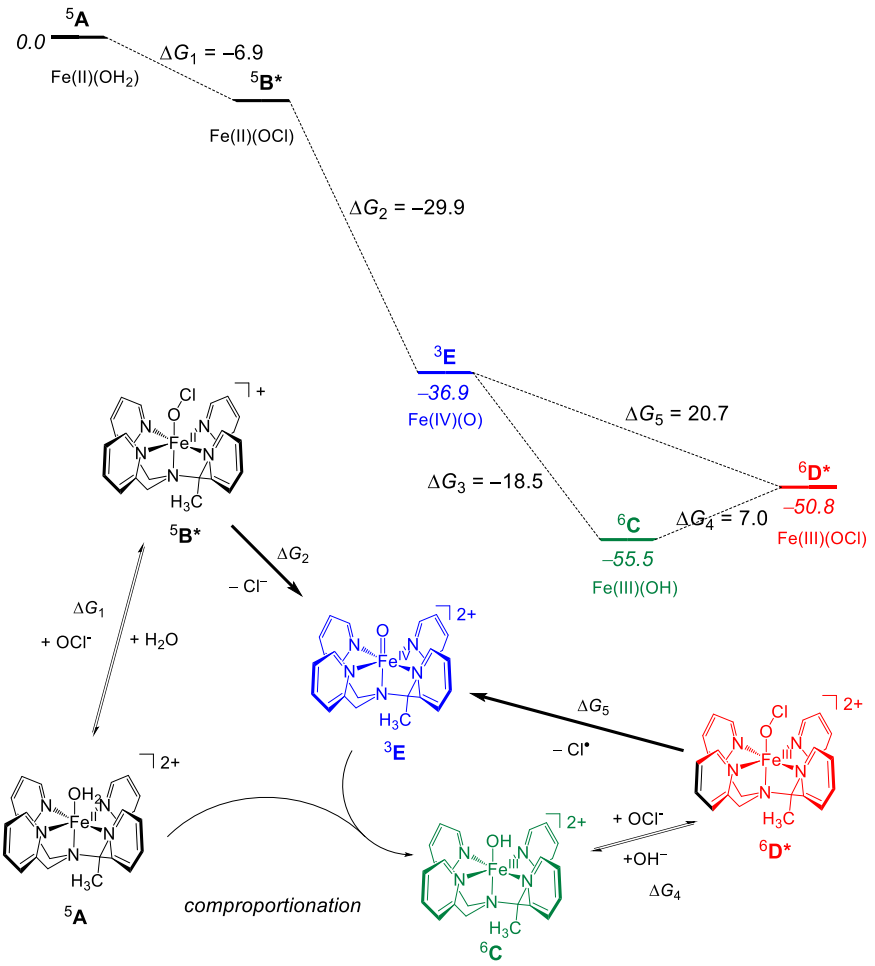

Scheme 6 Reaction scheme showing the formation of and relation between $[Fe(III)(OCl)(MeN4Py)]^{2+}$ and $[Fe(IV)(O)(MeN4Py)]^{2+}$ and calculated free energies for each step. Data includes dispersion, entropic and solvent corrections and is given in kcal mol^{-1}.

2.3 Conclusions

In summary, for the first time a non-heme iron(III)-hypochlorite complex was identified in acidic aqueous solution at room temperature. Importantly, it is found that a non-heme Fe(IV)=O species forms from both an Fe(III)-OOH and an Fe(III)-OCl complex by homolytic cleavage of the O-O and O-Cl bonds. Furthermore, the formation of Fe(II)-OOH and Fe(II)-OCl species initially is energetically plausible given the exorgonicity of the reactions. This reactivity is notable since the reverse reaction, i.e. the formation of hypohalites by reaction of Fe(IV)=O species with halides, is generally viewed as a key step in the halogenation of organic substrates.[1] In the case of iron halogenases the formation of intermediate Cl-Fe(IV)=O species have been proposed in which the Fe(IV)=O moiety abstracts a hydrogen atom followed by attack of the carbon radical formed on the bound chlorido ligand. Hence, the observation of a non-heme Fe(III)-OCl species and of a pathway to a potentially C–H abstracting Fe(IV)=O that involves concomitant formation of an hydroxyl or chlorine radical, holds implications in regard to our understanding of the mechanisms by which iron haloperoxidases and halogenases operate.

Furthermore, although Fe(III)-OCl species can be observed, it is clear that such species are at best transient and may be regarded as spectroscopically analogous to the corresponding Fe(III)-

OH and Fe(III)-OOH complexes. The key differences identified here in the UV/Vis absorption, Raman and EPR spectra provides an important basis of spectral characteristics with which to identify such species if present as actors in the biosynthesis of halogenated natural products.

Overall the mechanisms for reaction of **1** with H_2O_2 and with NaOCl are essentially the same. In each case the initial reaction of the two electron oxidation with **1** is heterolytic cleavage to generate the Fe(IV)=O species. Rapid comproportionation leads to quantitative conversion to the corresponding Fe(III)-OH species. This latter species then coordinates to the oxidants reversibly and undergoes homolytic OO and O-Cl bond cleavage to form Fe(IV)=O species and hydroxyl and chlorine radicals. The relative stability of the Fe(IV)=O species indicates that the reactive species, in terms of substrate oxidation, in each case is the radical formed that opens the path to a rebound mechanism[20] with the Fe(IV)=O species. In the next chapter the reactivity of **1** with oxygen and the formation of similar species will be discussed.

2.4 Experimental Section

Resonance Raman spectra were calculated for the Fe(III)-OCl (doublet) and the Fe(IV)=O (triplet) species using ORCA (version 3.0.2) and the IMDHO method as implemented in the orca_asa program.[21] The procedure used was as follows: The geometry optimization and the Hessian matrix (frequency) were calculated with the Becke88[22] and Perdew86[23] (BP86) DFT functional using Def2-TZVP basis set.[24] The Hessian matrix, generated by the frequency calculations, was used in combination with the TD-DFT [25] calculations, which were performed using the BH and HLYP functional with the TZVPP[24a] basis set for Iron and SV(P)[24a, 26] basis set for C, H, N, O and Cl, to calculate the rRaman enhancements for each normal mode.

All the calculations for energy landscapes and ^{18}O isotope shifts were performed using Density Functional Theory (DFT) with the unrestricted B3LYP method[27] as implemented in the Gaussian 09c program package.[28] Single point calculations with B3LYP-D3[29] were calculated using Jaguar V3.0 Rev 2.[30] All calculations utilized a triple-ζ quality basis set that includes LANL2TZ+(f) on iron and 6-311+G(d,p) on the rest of the atoms.[31] Free energies (ΔG) reported here use UB3LYP-D3 energies corrected with ZPE, thermal and entropic corrections from the frequency calculation at 298 K. The effect of solvent was tested through single point calculations using water as a solvent with the SMD solvation model as implemented in Gaussian.

Further information for the calculated molecules (i.e. coordinates) can be obtained in the supporting information of the article

A. Draksharapu, D. Angelone, M. G. Quesne, S. K. Padamati, L. Gómez, R. Hage, M. Costas, W. R. Browne, S. P. de Visser, *Angew. Chem., Int. Ed*. **2015**, *54*, 4357–4361.

http://onlinelibrary.wiley.com/store/10.1002/anie.201411995/asset/supinfo/anie_201411995_sm_miscellaneous_information.pdf

2.5 References

[1] a) M. Hofrichter, R. Ullrich, *Appl. Microbiol. Biotech*. **2006**, *71*, 276. b) A. Butler, M. Sandy, *Nature* **2009**, *460*, 848. c) F. H. Vaillancourt, E. Yeh, D. A. Vosburg, S. Garneau-Tsodikova, C. T. Walsh, *Chem. Rev*. **2006**, *106*, 3364. d) V. Conte, A. Coletti, B. Floris, G. Licini, C. Zonta, *Coord. Chem. Rev*. **2011**, *255*, 2165.

[2] a) G. W. Gribble, *Acc. Chem. Res*. **1998**, *31*, 141. b) C. S. Neumann, D. G. Fujimori, C. T. Walsh *Chem. Biol*. **2008**, *15*, 99.

[3] a) K. H. van Peè, C. Dong, S. Flecks, J. Naismith, E. P. Patallo, T. Wage, *Adv. Appl. Microbiol*. **2006**, *59*, 127. b) J. L. Anderson, S. K. Chapman, *Mol. Biosyst*. **2006**, *2*, 350. c) M. Sono, M. P. Roach, E. D. Coulter, J. H. Dawson, *Chem. Rev.* **1996**, *96*, 2841.

[4] A. K. Vardhaman, P. Barman, S. Kumar, C. V. Sastri, D. Kumar, S. P. de Visser, *Chem. Commun*. **2013**, *49*, 10926.

[5] a) M. Costas, M. P. Mehn, M. P. Jensen, L. Que Jr, *Chem. Rev*. **2004**, *104*, 939–986; b) S. V. Kryatov, E. V. Rybak-Akimova, S. Schindler, *Chem. Rev*. **2005**, *105*, 2175. c) W. Nam, *Acc. Chem. Res*. **2007**, *40*, 522. d) P. C. A. Bruijnincx, G. van Koten, R. J. M. Klein Gebbink, *Chem. Soc. Rev*. **2008**, *37*, 2716.

[6] a) A. Lennartson, C. J. McKenzie, *Angew*. *Chem*., Int Ed., **2012**, *51*, 6767. b) S. J. Kim, R. Latifi, H. Y. Kang, W. Nam, S. P. de Visser, *Chem. Commun*. **2009**, 1562. c) S. Hong, B. Wang, M. S. Seo, Y.-M. Lee, M. J. Kim, H. R. Kim, T.Ogura, R. Garcia-Serres, M. Clémancey, J.-M. Latour, W. Nam, *Angew. Chem. Int. Ed.* **2014**, *53*, 6388.

[7] Z. Cong, S. Yanagisawa, T. Kurahashi, T. Ogura, S. Nakashima, H. Fujii, *J. Am. Chem. Soc.* **2012**, *134*, 20617.

[8] H. A. Wagenknecht, W. D. Woggon, *Chem. Biol*. **1997**, *4*, 367.

[9] V. Balland, M.-F. Charlot, F. Banse, J.-J. Girerd, T. A. Mattioli, E. Bill, J.-F. Bartoli, P. Battioni, D. Mansuy, *Eur. J. Inorg. Chem.* **2004**, 301. Balland *et el.* noted the appearance of an absorption band at ca. 435 nm upon addition of 100 equiv. of NaOCl to a methanol solution of $[Fe(II)(L_5^n)Cl]^+$ (L_5^2 = N-methyl-N,N,N-tris(2-pyridylmethyl)ethane-1,2-diamine and L_5^3 = N-methyl-N,N,N-tris(2-pyridylmethyl)propane-1,3-diamine) at 0 ^oC prior to the appearance of the expected NIR absorption band of the corresponding Fe(IV)=O species. The authors proposed the intermediate to be an Fe(II)-OCl species.

[10] See, *e.g*., a) J.-U. Rohde, J.-H. In, M. H. Lim, W. W. Brennessel, M. R. Bukowski, A. Stubna, E. Münck, W. Nam, L. Que Jr, *Science* **2003**, *299*, 1037. b) M. R. Bukowski, K. D. Koehntop, A. Stubna, E. L. Bominaar, J. A. Halfen, E. Münck, W. Nam, L. Que Jr, *Science* **2005**, *310*, 1000. c) D. C. Lacy, R. Gupta, K. L. Stone, J. Greaves, J. W. Ziller, M. P. Hendrich, A. S. Borovik, *J. Am. Chem. Soc*. **2010**, *132*, 12188. d) M. Martinho, F. Banse, J.-F. Bartoli, T. A. Mattioli, P. Battioni, O. Horner, S. Bourcier, J.-J. Girerd, *Inorg. Chem*. **2005**, *44*, 9592. e) S. P. de Visser, D. Kumar, (*Eds.*) *Iron-containing enzymes: Versatile catalysts of hydroxylation reaction in nature*, RSC Publishing, Cambridge (UK), **2011**.

[11] A. Draksharapu, D. Angelone, M. G. Quesne, S. K. Padamati, L. Gómez, R. Hage, M. Costas, W. R. Browne, S. P. de Visser, *Angew. Chem., Int. Ed*. **2015**, *54*, 4357.

[12] a) D. Wang, K. Ray, M. J. Collins, E. R. Farquhar, J. R. Frisch, L. Gómez, T. A. Jackson, M. Kerscher, A. Waleska, P. Comba, M. Costas, L. Que Jr, *Chem. Sci*. **2013**, *4*, 282. b) A. Draksharapu, Q. Li, H. Logtenberg, T. A. van den Berg, A. Meetsma, J. S. Killeen, B. L. Feringa, R. Hage, G. Roelfes, W. R. Browne, *Inorg. Chem*. **2012**, *51*, 900. c) A. Draksharapu, Q. Li, G. Roelfes, W. R. Browne, *Dalton* **2012**, *41*, 13180.

[13] The Fe(II) complexes $[Fe(II)(CH_3CN)(N4Py)]^{2+}$ and $[Fe(II)(Cl)(MeN4Py)]^{2+}$ undergo immediate solvolysis in water to form the corresponding $[Fe(II)(OH_2)(N4Py)]^{2+}$ and $[Fe(II)(OH^2)(MeN4Py)]^{2+}$ complexes at pH *ca*. 3, respectively.[12b]

[14] The value is an estimate based on the assumption of a maximum of 40% conversion of the Fe(III) present being in the form of Fe(III)-OCl. The value is consistant with the molar absorptivity of related Fe(III)-OOH complexes. R. Y. N. Ho, L. Que Jr., G. Roelfes, B. L. Feringa, R. Hermant, R. Hage, *Chem. Commun.* **1999**, 2161.

[15] Essentially, the same trend in the time dependence of spectroscopic properties were obtained with the related complex $[Fe(II)(OH_2)(N4Py)]^{2+}$ (where N4Py = 1,1-di(pyridin-2-yl)-*N*,*N*-bis(pyridin-2-

ylmethyl)methanamine, although the corresponding Fe(IV)=O species was found to be less stable (see Figures S1 and S11, for details in ref 11).

[16] A. Draksharapu, "Shedding light on active species in Fe, Ni and Cu catalysis", **2013**, ISBN: 9789036766227.

[17] a) G. Roelfes, M. Lubben, K. Chen, R. Y. N. Ho, A. Meetsma, S. Genseberger, R. M. Hermant, R. Hage, S. K. Mandal, V. G. Young, Y. Zang, H. Kooijman, A. L. Spek, L. Que, B. L. Feringa, *Inorg. Chem.* **1999**, 38, 8, 1929-1936. b) J. J. Mcgarvey, A. Draksharapu, W. R. Browne, Special periodic reports 2013, 44, 68-94.

[18] NaOBr was prepared from aqueous NaOCl and NaBr (Figure S14 of ref **[11]**).

[19] a) A. K. Vardhaman, C. V. Sastri, D. Kumar, S. P. de Visser, *Chem. Commun*. **2011**, *47*, 11044–11046; b) A. K. Vardhaman, P. Barman, S. Kumar, C. V. Sastri, D. Kumar, S. P. de Visser, *Angew. Chem. Int. Ed*. **2013**, *52*, 12288–12292; *Angew. Chem*. **2013**, *125*, 12514–12518.

[20] a) W. Nam, Y.-M. Lee, S. Fukuzumi, *Acc. Chem. Res.* **2014**, 47, 1146. b) L. V. Liu, S. Hong, J. Cho, W. Nam, E. I. Solomon, *J. Am. Chem. Soc.* **2013**, 135, 3286.

[21] (a) T. Petrenko, F. Neese, *J. Chem. Phys*., **2007**, *127*, 164319; (b) T. Petrenko, F. Neese, *J. Chem. Phys*., **2012**, *137*, 234107

[22] A. D. Becke, *Phys. Rev. A*, **1988,** *38*, 3098.

[23] J. P. Perdew, *Phys. Rev. B*, **1986,** *33***,** 8822.

[24] (a) A. Schaefer, H. Horn, R. Ahlrichs, *J. Chem. Phys*. **1992**, *97*, 2571. (b) F. Weigenda, R. Ahlrichs, *Phys. Chem. Chem. Phys*., **2005**, *7*, 3297.

[25] (a) F. Negri, M. Z. Zgierski, *J. Chem. Phys*. 1994, *100*, 1387. (b) K. Gustav, M. Storch, *Int. J. Quantum Chem.* **1990**, *38*, 25. (c) K. Gustav, C. Seydenschwanz, *Chem. Phys. Lett*. **1986**, *123*, 261.

[26] A. Schaefer, C. Huber, R. Ahlrichs, *J. Chem. Phys.* **1994**, *100*, 5829.

[27] (a) A. D. Becke, *J. Chem. Phys*. **1993**, *98*, 5648. (b) C. Lee, W. Yang, R. G. Parr, *Phys. Rev. B* **1988**, *37*, 785.

[28] *Gaussian*-09, Revision B.01, M. J. Frisch, G. W. Trucks, H. B. Schlegel, G. E. Scuseria, M. A. Robb, J. R. Cheeseman, G. Scalmani, V. Barone, B. Mennucci, G. A. Petersson, H. Nakatsuji, M. Caricato, X. Li, H. P. Hratchian, A. F. Izmaylov, J. Bloino, G. Zheng, J. L. Sonnenberg, M. Hada, M. Ehara, K. Toyota, R. Fukuda, J. Hasegawa, M. Ishida, T. Nakajima, Y. Honda, O. Kitao, H. Nakai, T. Vreven, J. A. Montgomery, Jr., J. E. Peralta, F. Ogliaro, M. Bearpark, J. J. Heyd, E. Brothers, K. N. Kudin, V. N. Staroverov, T. Keith, R. Kobayashi, J. Normand, K. Raghavachari, A. Rendell, J. C. Burant, S. S. Iyengar, J. Tomasi, M. Cossi, N. Rega, J. M. Millam, M. Klene, J. E. Knox, J. B. Cross, V. Bakken, C. Adamo, J. Jaramillo, R. Gomperts, R. E. Stratmann, O. Yazyev, A. J. Austin, R. Cammi, C. Pomelli, J. W. Ochterski, R. L. Martin, K. Morokuma, V. G. Zakrzewski, G. A. Voth, P. Salvador, J. J. Dannenberg, S. Dapprich, A. D. Daniels, O. Farkas, J. B. Foresman, J. V. Ortiz, J. Cioslowski, D. J. Fox, Gaussian, Inc., Wallingford CT, **2010**.

[29] S. Grimme, J. Antony, S. Ehrlich, H.Krieg, *J. Chem. Phys*. **2010**, *132*, 154104.

[30] *Jaguar* 7.7, version 7.9, Schrodinger, LLC, New York, NY, **2011**.

[31] P. J. Hay, W. R. Wadt, *J. Chem. Phys*. **1985**, *82*, 299.

Chapter 3

Elucidating the mechanism of O_2 activation by Fe(II) polypyridylamine complexes in water

In this chapter, computational studies are described focused on the elucidation of the mechanisms involved in the activation of O_2 by iron complexes with 1,1-di(pyridin-2-yl)-N,N-bis(pyridin-2-ylmethyl)ethanamine (MeN4Py) and 1,1-di(pyridin-2-yl)-N,N-bis(pyridin-2-ylmethyl)methanamine (N4Py). Mechanistic scenarios involving various complexes are compared in order to understand the effect of the metal ion and its various spin states on the activation of O_2 towards C-H activation.

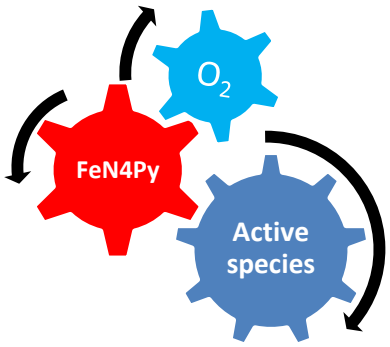

3.1 Introduction

The activation of O_2 is a central reaction in nature, not least in aerobic respiration by living organisms in which it serves as an electron acceptor to form water at the end of the mitochondrial relay or directly by oxygenases and peroxidases to oxygenate organic substrates. The activation of O_2 catalysed by metalloenzymes is key to understanding the mechanism of bioprocesses involving oxygen. Several examples of O_2 activating metal complexes have been recently discovered and studied over the last decades,[1] and have stimulated the design of simpler synthetic structural and functional analogues.[2, 3]

A wide range of important enzyme-catalysed reactions including the biosynthesis of natural products and metabolism of xenobiotics involve the generation of high valent iron species formed primarily by direct reaction of Fe(II) and Fe(III) based enzymes with oxygen. The transient nature of these intermediates, in particular those involving non-heme enzymes, frustrates efforts to observe them and elucidate mechanistic details. It is in this aspect that functional models for biological systems are essential. In recent years, the activation of $^3O_2$ by Fe(II) polypyridylamine complexes has been explored, in particular to understand the factors that determine their activity in achieving substrate oxidation (such as the oxidative cleavage of double strand DNA).[4] In this chapter, a combined experimental and theoretical study is described focused on the reaction of Fe(II)-N4Py complexes with O_2 and the pathways that are involved in achieving substrate oxidation. The major focus is on the generation of superoxide upon reaction of Fe(II) polypyridylamine based complexes with O_2, and in particular the enhancement in reaction rates observed by irradiation with visible light.[3] This will be complemented by state-of-the-art density functional studies using methods[5] that have been proven[5,6] to work well for calculation of spin-state dependent properties which are expected to play a major role.

The activation of O_2 under physiologically relevant conditions by Fe(II) complexes in a manner that mimics the action of Fe-Bleomycin[7] was first reported by Roelfes et al. in 2000.[8] The activity of FeN4Py towards two lines of cancerous cells has been shown to be similar or better compared to Bleomycin.[9] In this system, the Fe(II) complex reacts with O_2 spontaneously to provide oxidising equivalents capable of C-H abstraction and single strand cleavage of DNA. [10]

The mechanism by which the Fe(II) complex catalyses DNA oxidation has been studied experimentally through the effect of scavengers of various types on DNA cleavage. It was apparent that the superoxide radical anion is formed during the reaction between the Fe(II) complex and O_2 (Figure 1).[11] The presence of a reducing agent (dithiothreitol: DTT) the number of DNA cleavage events increases indicating that reduction of the Fe(III) intermediate to the Fe(II) state is a thermodynamic bottleneck. Furthermore the reduction to the Fe(II) state allows it to react with the superoxide formed to produce a reactive Fe(III) hydroperoxido adducts such as those discussed in the chapter 2. In presence of DTT and superoxide dismutase (SOD) the reaction efficiency increases since the thermodynamically advantageous Fe(III) reduction being augmented by the disproportionation of superoxide to O_2 and H_2O_2; the Fe(II) and the peroxide formed in this case can perform efficient oxidation of substrates (Chapter2). When DTT is not present, SOD decreases the number of DNA cleavage events slightly presumed to be due to superoxide disproportionation yielding only half an equivalent of hydrogen peroxide whilst the energy barrier to form the superoxide and Fe(III) remain unchanged. When catalase and SOD are

both present the reactivity of the system towards DNA cleavage is dramatically inhibited, regardless of presence or not of DTT ascribed to disproprortionation of the reactive species formed to water and dioxygen.

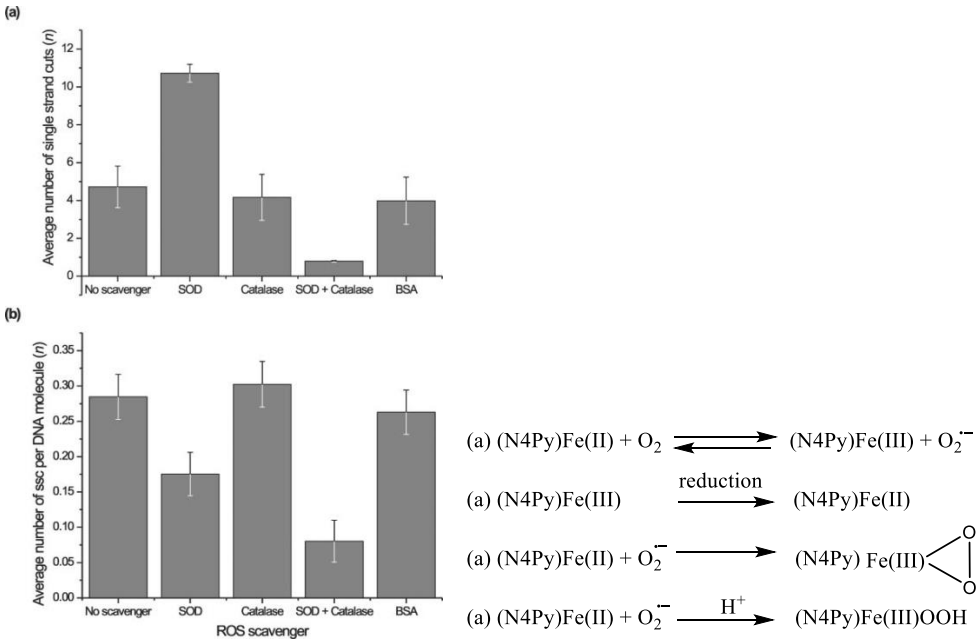

Figure 1 (Left) The effect of scavengers: SOD (for superoxide), catalase (for H_2O_2), BSA (for assessing the innocence of peptides), in the presence (upper) and absence (lower) of DTT (reducing agent). (right) The proposed mechanism deduced from the results of the scavenger experiments. Reproduced with permission from Li et al. [11] Copyright Wiley (2009).

Later studies by Li et al. noted that visible light accelerated DNA cleavage catalysed by an Fe(II) complex of N4py and showed that there is only a minor wavelength dependence on the enhancement even with the addition of photosensitizers such as 1,8-naphthalimide and 9-aminoacridine (Figure 2).[12]

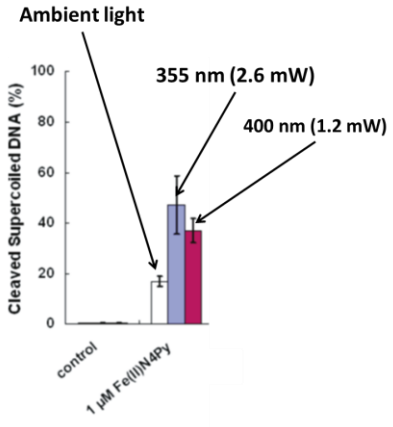

Figure 2 Effect of irradiation on DNA cleavage efficiency (see figure 1 for comparison without light) reproduced with permission from Li et al. [12] Copyright ACS (2012).

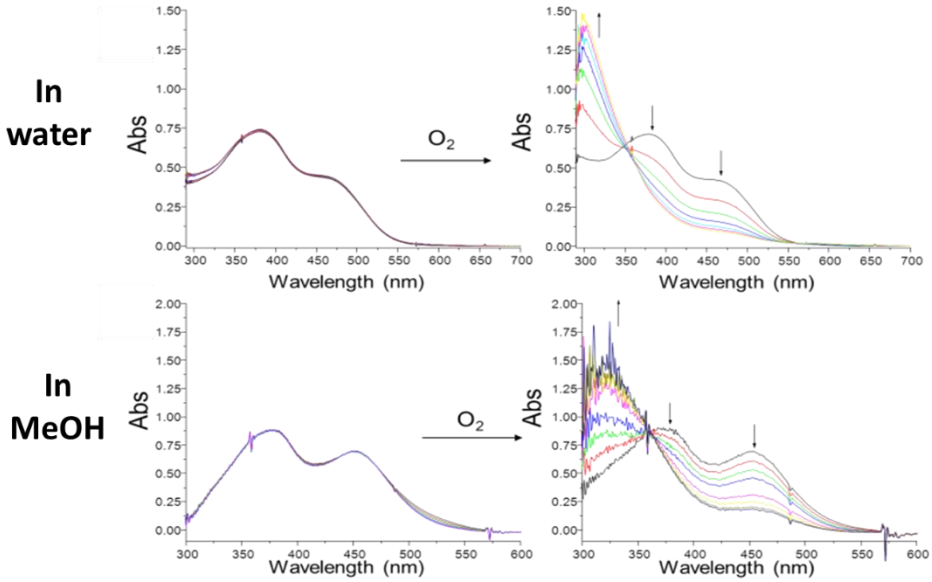

Figure 3 Dependence of changes observed under irradiation before and after oxygenating the solutions of FeN4Py in water (top graphs) and methanol (bottom graphs). Reproduced with permission of the authors.[3]

Draksharapu et al. investigated the effect of light on Fe(II)N4py complexes in methanol, water and dichloromethane. It was shown that, provided that a minimum of water and O_2 were present, irradiation with visible light leads to O_2 activation and formation of the corresponding Fe(III)-N4py complexes (Figure 3). The ability to accelerate the oxidation of Fe(II)N4py with visible light (from 500 nm to near UV) indicates that excitation to ^{1}MLCT states leads to population of excited (d-d*) metal centered states. The oxidation of Fe(II)N4Py proceeds thermally in water also but under irradiation it proceeds relatively rapidly in methanol and dichloromethane yielding formaldehyde in the case of methanol.

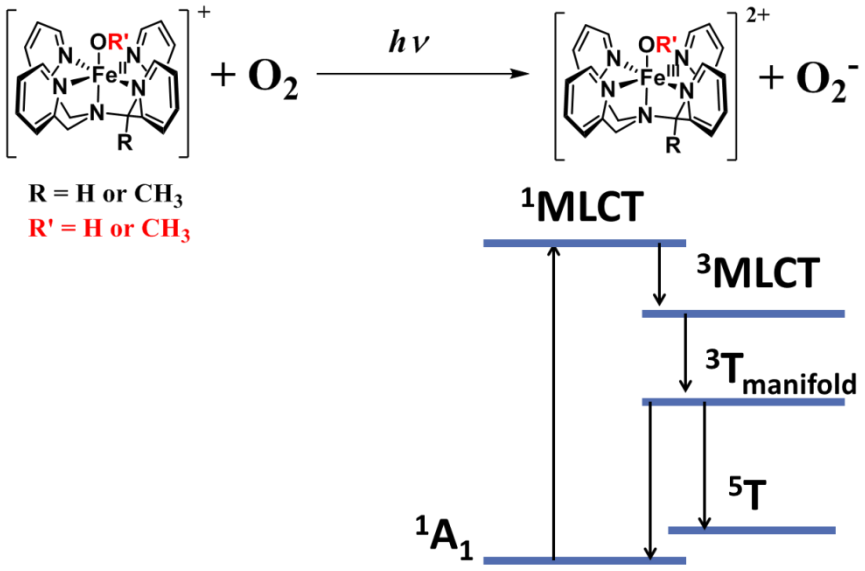

Figure 4 Simplified Jablonski diagram for Fe(II)N4py and overall reaction with O_2 and light.[3]

The mechanism proposed by Draksharapu et al. invoked the formation of superoxide but it was proposed that the acceleration of the reaction with irradiation was due to intersystem crossing

to spin states that favour electron transfer. In this model, the reduction of oxygen to superoxide occurs due to population of a high energy spin state of the Fe(II)N4Py complex from which electron transfer to O_2 occurs.

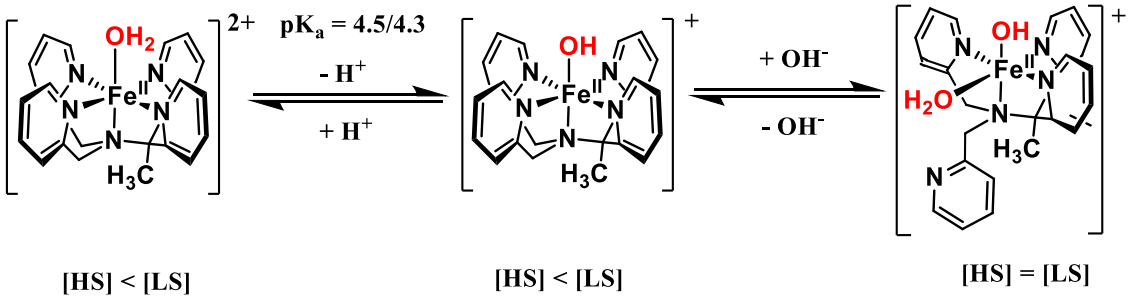

Figure 5 Proposed structures from the work of Draksharapu et al. [2] in water under acidic, neutral and basic conditions and spin state equilibrium positions [HS] = Proportion of complex in non singlet spin state, [LS] = Proportion of complex in singlet spin state.

Draksharapu et al. studied the speciation of Fe(II)N4Py in water at low and high pH and demonstrated that not only are various protonation states involved in the speciation but also the singlet and quintet states are relatively close in energy. Furthermore partial ligand dissociation (loss of a pyridyl) occurs above pH 6.[2] The key questions to be addressed in this chapter is: what is the mechanism by which the Fe(II)-N4Py complexes react with O_2 and especially how light accelerates this process? How does the species formed react with methanol/ribose? Two pathways are considered in this chapter: an outer shell electron transfer and an associative/dissociative (ligand exchange) pathway (Figure 6).

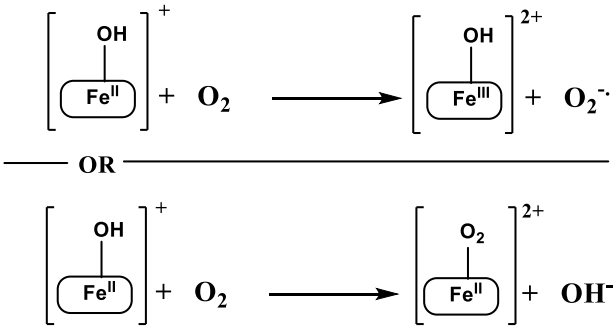

Figure 6 Mechanisms of interaction between the Fe(II)N4Py and O_2 considered in this chapter: outer sphere electron transfer (upper pathway) and inner sphere (ligand exchange, lower pathway).

3.2 Results and discussion

Calculation of spin state energies and excitation spectra for species present in water

The study of the reactivity in water begins with the calculation of spin states and properties of the species present in water according to Draksharapu et al.[2] followed by exploration of possible reaction pathways and energies of the species in various spin states in water with DFT methods. Experimentally it is found that dissolution of FeN4Py-X complexes (where X is the axial ligand and can be acetonitrile or chlorido) in water, solvation leads to the formation of three species (Figure 7) in a pH dependent equilibrium. UV-vis absorption and ^{1}H NMR spectroscopy indicated furthermore that the high spin and low spin states of the complexes lie close in energy. DFT calculations (Figure 7) are qualitatively in agreement with the experimental data. A rapid

exchange in spin state is also thermally reasonably since the triplet state, which constitutes a barrier to the HS ⇔ LS transitions, is also thermally accessible.

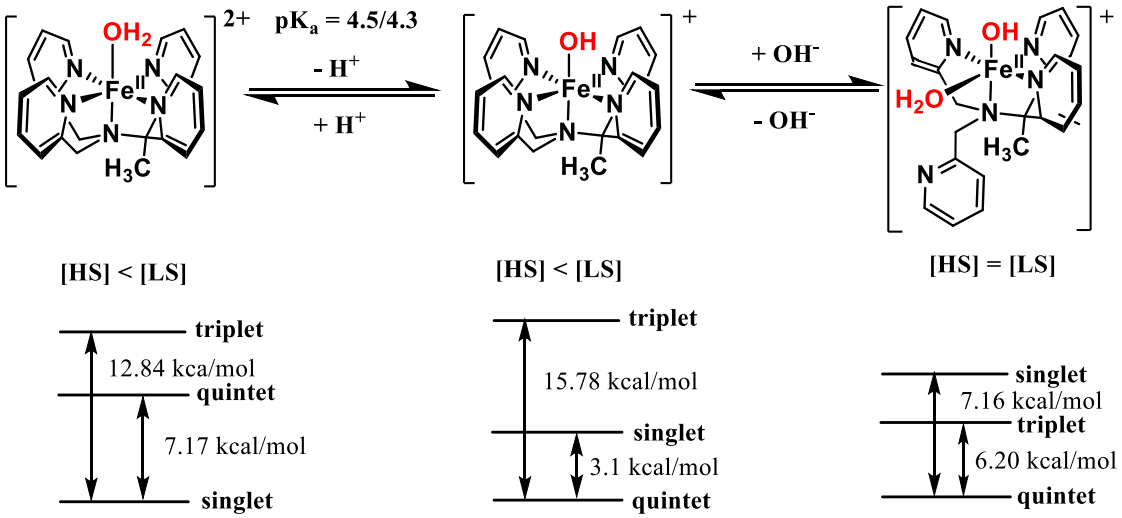

Figure 7 From left to right species present, respectively, from low to high pH in water. Below: energy scheme for three spin states. HF = High Spin, LS = Low Spin.

It is of note that calculations indicate that in the quintet and the triplet states, the species proposed to be present at high pH (aqua hydroxido complex), loses a molecule of water to form a pentacoordinate Fe(II) complex (Figure 8(a)) explaining the dramatic decrease of the triplet state energy level.

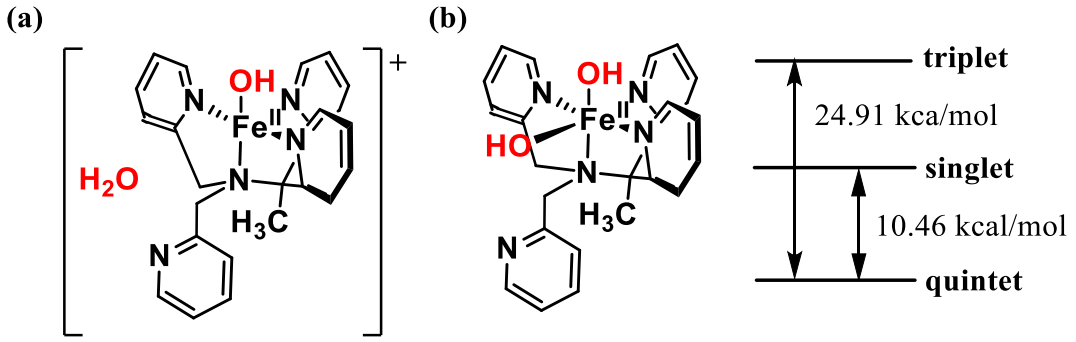

Figure 8 a) Structure of [Fe(II)N4Py-(OH)(H_2O)]$^+$ in the triplet state at high pH. The equatorial aqua ligand is essentially expelled in this state. b) Relative spin state energies for the neutral complex [Fe(II)N4Py-$(OH)_2$].

It is more reasonable that the possible species present in water at high pH could be that shown in Figure 8(b), and indeed the hydroxides are more strongly bound to the Fe(II) ion. The corresponding complex [Fe(II)(MeN4Py)($NCCH_3$)]$^{2+}$, which has the peculiarity that in contrast to the other complexes considered, the singlet state is stabilised by the stronger binding energy of the acetonitrile with respect to water (Figure 9a). Methanol has the opposite effect to acetonitrile, however, and calculations indicate that the low spin state is favoured for this compound (Figure 9b).

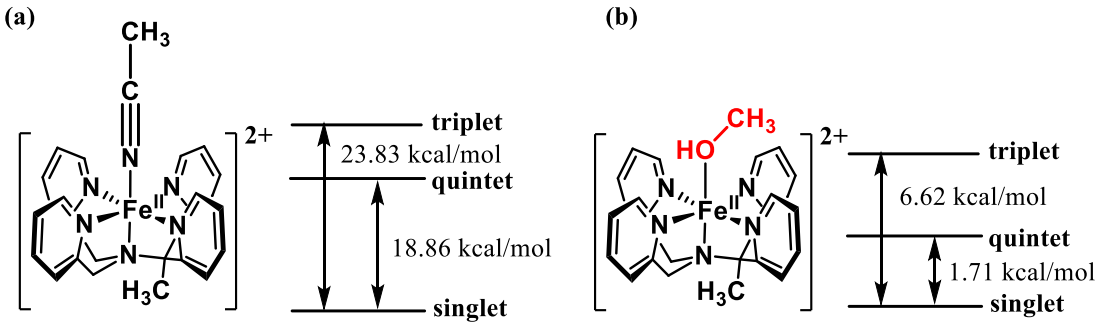

Figure 9 a) Lewis structure of the $[Fe(II)(MeN4Py)(NCCH_3)]^{2+}$ with the relative spin state free energy separation. b) Lewis structure of the $[Fe(II)(MeN4Py)(HOCH_3)]^{2+}$ with the relative spin state free energy separation.

Agreement with ^{1}H-NMR and UV/Vis spectroscopy data is an indication of the accuracy of the DFT prediction regarding the spin states of $[Fe(II)(MeN4Py)(NCCH_3)]^{2+}$.[2]

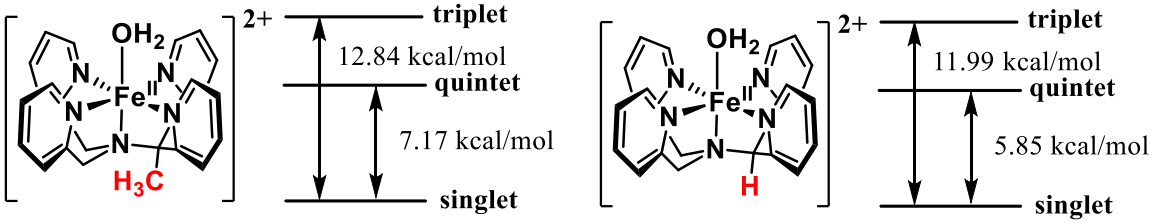

Figure 10 Relative spin state free energy separation for $[Fe(II)(MeN4Py)(NCCH_3)]^{2+}$, and $[Fe(II)(MeN4Py)(OH_2)]^{2+}$, complexes.

The UV/Vis absorption spectra of the Fe(II) complexes of the ligands N4Py and MeN4Py are slightly different, with the latter consistent with a shift of the spin state equilibrium of the complex (in water) in favour of the singlet state. DFT calculations indicate also that the methyl group at the tertiary carbon of the ligand results in a relative stabilization of the singlet spin state for electronic reasons rather than steric effects. The excitation transitions were calculated for the $[Fe(II)(MeN4Py)(OH)]^+$ in the quintet and singlet electronic configuration (Figure 11) and confirm assignment of the experimental spectra. The singlet state has two absorption bands in the visible region with reasonably high oscillator strength whereas the complex in the high spin state does not. The characterization and understanding (with DFT methods) of the various Fe(II)N4Py species in water presents interesting results despite that the number of possible species present in water in equilibrium with each other, dependent on the pH also, especially the relative facile switching between spin states in water.

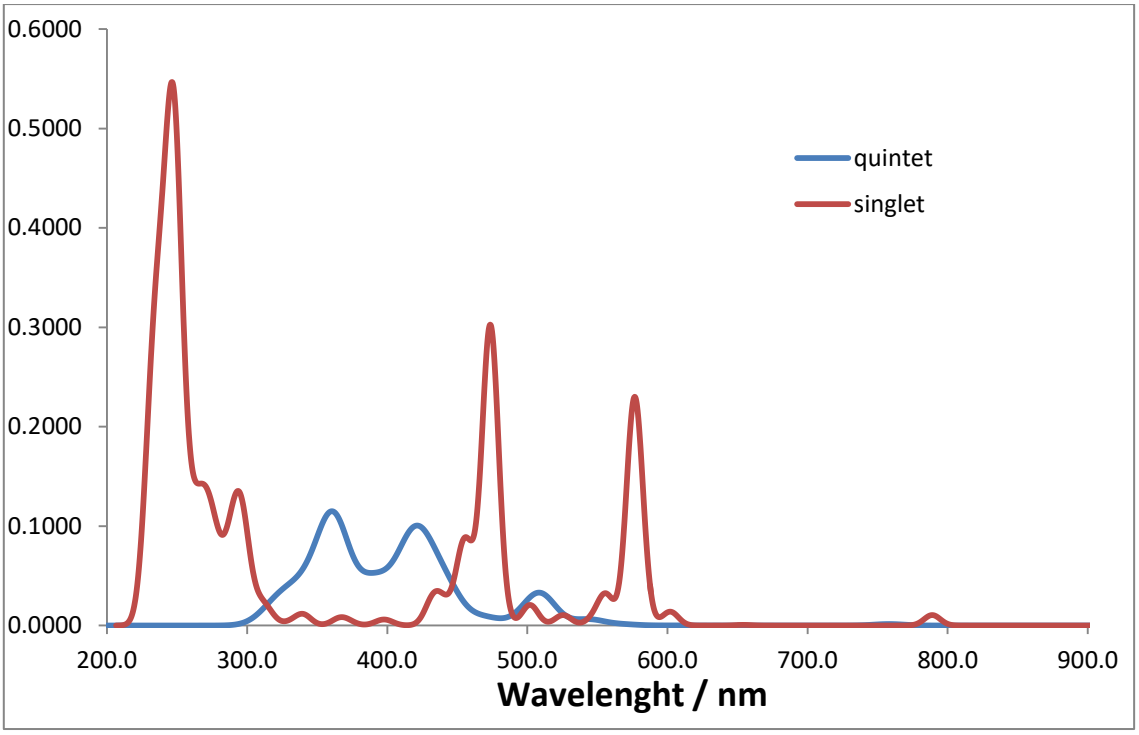

Figure 11 TD-DFT simulation (SAOP/TZ2P) of absorption spectra for $[Fe(II)(MeN4Py)(OH)]^{2+}$, singlet (red line) and quintet (blue line). The Y axis indicates oscillator strength.

Energy landscape for outer sphere electron transfer to O_2 in water:

The reactivity of the Fe(II) complexes of MeN4Py with O_2 can be viewed as either proceeding through outer or inner sphere electron transfer, and both mechanisms were studied computationally. In the case of an outer sphere mechanism the triplet state is thermally accessible for both acidic and neutral species formed in water, which opens the possibility that the triplet is an intermediate state in the singlet/quintet spin transition. Outer sphere electron transfer from the Fe(II) complexes to $^3O_2$ is endergonic by slightly less than 10 kcal/mol from the triplet state, however the steady state population of this state is low when one considers the Boltzmann distribution. Nevertheless, in the triplet state outer sphere electron transfer to oxygen is a reasonable process (Figure 12). Draksharapu et al.[3] proposed that the reaction with oxygen was accelerated under photoexcitation by an increase in the steady state population of the triplet state through ISC from the ^{1}MLCT states. This increase in population makes the reaction more exergonic overall due to the increase in the population of the triplet state. The pK_a for the protonation of the superoxide radical anion is 4.88[13] and hence $[Fe(III)(MeN4Py)(OH_2)]^{2+}$ (pK_a = ~2.5) species formed is capable of protonating superoxide (c.f. Libido rule).

Although $^3O_2$ is considered to be one of the most powerful oxidants available in nature its chemical inertia is hidden in the redox transformation to superoxide. Indeed the Latimer diagram for oxygen (Figure 13) shows that, although the overall standard reduction potential is high 1.22 V and hence should be facile to reduce, the initial reduction has a much more negative standard reduction potential -0.091 V, which is below that of the $[Fe(II)(MeN4Py)(OH)]^{2+}$ and $[Fe(II)(MeN4Py)(OH_2)]^{2+}$ (0.078 V and 0.318 V, respectively).

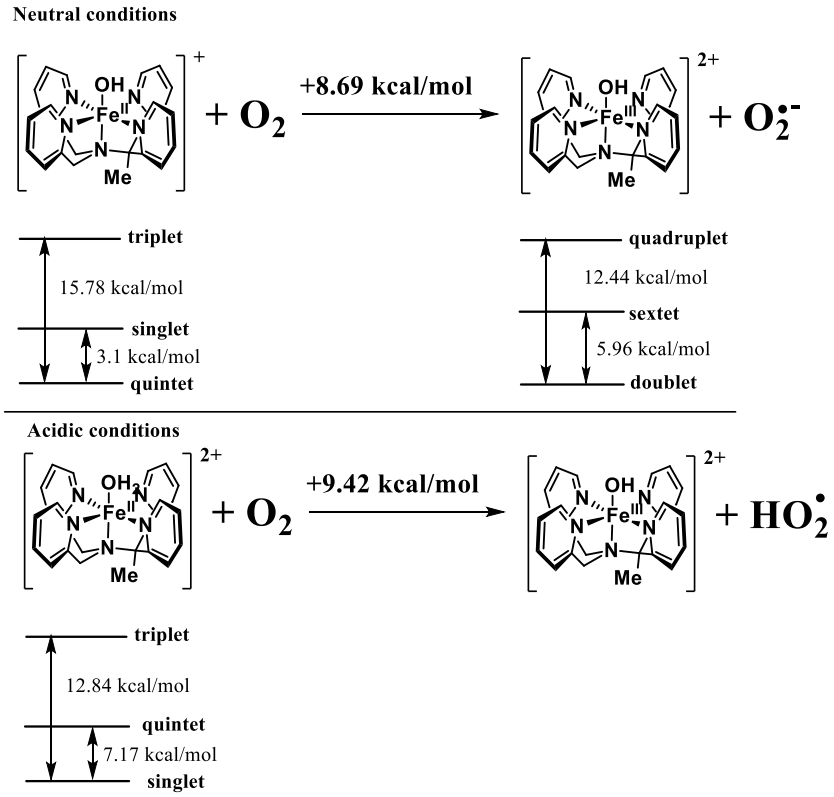

Figure 12 Energetics for the reaction of $[Fe(II)(MeN4Py)(OH_2)]^{2+}$ with O_2 through outer sphere electron transfer in water. The upper scheme is under neutral conditions and the lower is under acidic conditions.

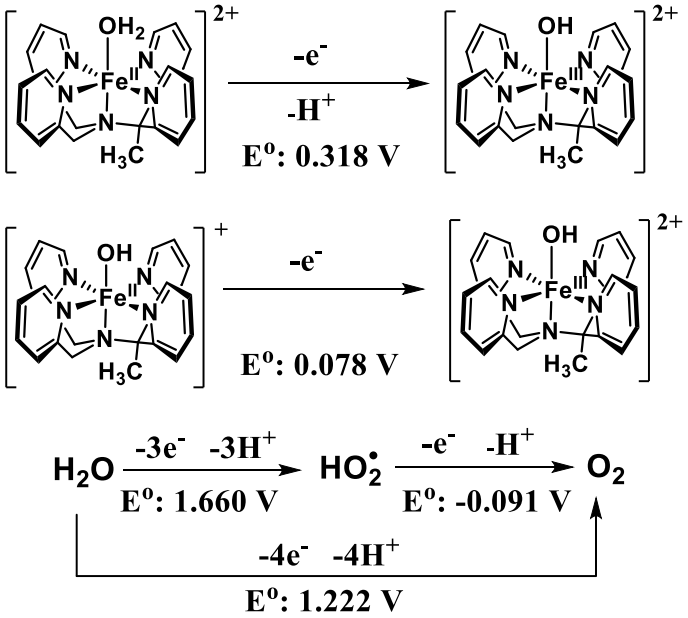

Figure 13 Calculated redox potentials vs SHE of $[Fe(II)(MeN4Py)(OH_2)]^{2+}$, $[Fe(II)(MeN4Py)(OH)]^{+}$ and $O_2/HO_2/H2O$. The calculated values are in agreement with literature values.[2]

Although, thermodynamically the outer sphere electron transfer mechanism is uphill and thereby not obviously feasible without, e.g., photoexcitation, calculations of $^3O_2$ in proximity to $[Fe(II)(MeN4Py)(OH)]^{+}$ reveal certain details that suggest an alternative pathway.

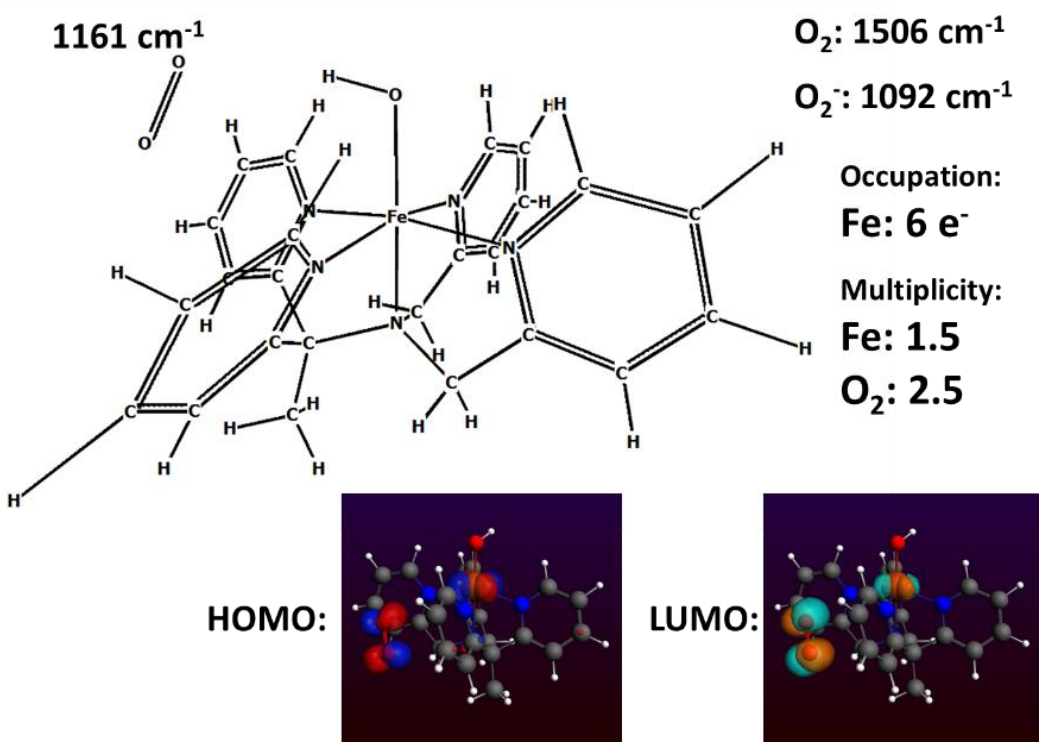

Figure 14 Calculation of O_2 in proximity of an $[Fe(II)(MeN4Py)(OH)]^+$. The frequency of the O=O stretching mode is shown when in proximity to the complex in comparison with superoxide and dioxygen. The spin distribution and the iron ions electronic occupation are also considered. The HOMO (left inset) and LUMO (right inset) orbitals are shown also.

In Figure 14 it is shown that O_2 in proximity of the $[Fe(II)(MeN4Py)(OH)]^+$ provides evidence for charge transfer based on:

- The decrease in the frequency of the stretching mode of O_2 towards that of a superoxide.
- The multiplicities of the O_2 and of the iron ion are intermediate between the reagents and the products.
- There is substantial partitioning of the HOMO and LUMO orbitals across the Fe(II) ion and the O_2.

Hence although electron transfer from the Fe(II) ion to O_2 can be excluded because of the likely thermodynamic barrier from the singlet or quintet ground state, photoexcitation opens this reaction pathway, and the findings reported in Figure 14 opens the possibility of a FeN4Py activated dioxygen encounter complex that provides an alternate pathway.

Energy landscape for dissociative exchange of water with O_2

Since direct electron transfer is unfeasible thermodynamically, a dissociative (ligand exchange) pathway where the axial ligand exchanges for oxygen was considered. Under acidic conditions, the $[Fe(II)(MeN4Py)(OH_2)]^{2+}$ undergoes dissociation of water to form a pentacoordinated species, which costs ca. 21.79 kcal/mol but is compensated by the formation of a more stable oxygen adduct (ΔG -13.09 kcal/mol). This limiting pathway leads to the formation of a Fe(III)-superoxide species (Figure 15). Under neutral or slightly basic conditions the same ligand exchange pathway is energetically expensive (18 kcal/mol), primarily due to lack of protonation.

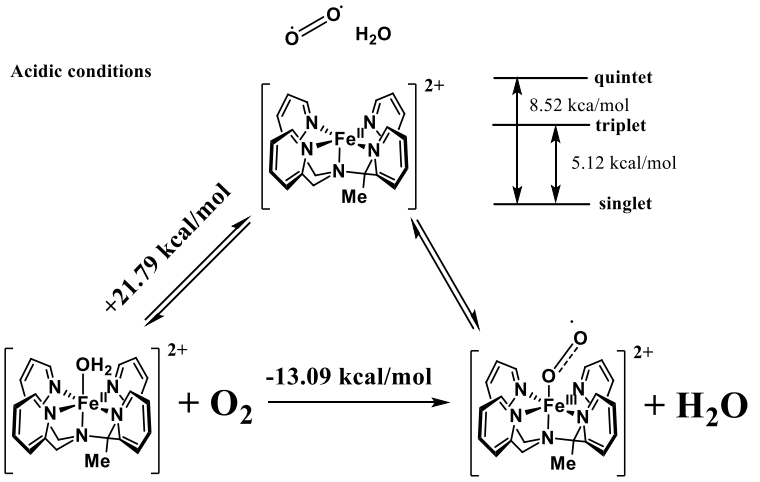

Figure 15 Model for a dissociative pathway. O_2 binds directly to $[Fe(II)(MeN4Py)]^{2+}$ to yield an Fe(III)-superoxido species.

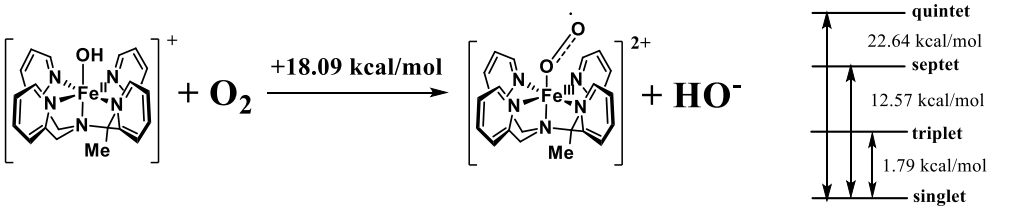

Figure 16 The dissociative pathway modelled starting with the most abundant species in water at pH 7.

The species obtained by ligand exchange presents a complicated electronic structure since it can assume many spin states (from singlet to septet). However, the lower spin states are energetically favoured. The minor difference between singlet and triplet is due to a weak antiferromagnetic coupling between the Fe(III) ion and the superoxide.

Reaction of FeN4Py with O_2 in methanol as a model for ribose oxidation

The formation of methanal was observed following the activation of O_2 by irradiation of $[Fe(II)(MeN4py)(OCH_3)]^+$, which prompted consideration of the reactivity of the proposed Fe(III)-OO species. The calculated reaction proceeding via the formation of the Fe(III) superoxide adduct is, as discussed above for Fe(II)-OH_2, uphill by 13.18 Kcal/mol, possibly due to the partial oxidation of the methoxide concomitant with ligand exchange (Figure 19). The abstraction of a hydrogen atom from the methyl fragment indicates an early transition state (about 2 kcal/mol above the previous intermediate), which suggests that a more realistic transition state involves a 2 electron and one hydrogen atom transfer. However, the hydrogen abstraction results in the electronic configuration of the fragment converges to formaldehyde and the Fe(II) complex relaxes to a singlet state forming the reactive $[Fe(II)(MeN4Py)(OOH)]^+$ with a decrease of circa 27 kcal/mol in free energy (Chapter 2).

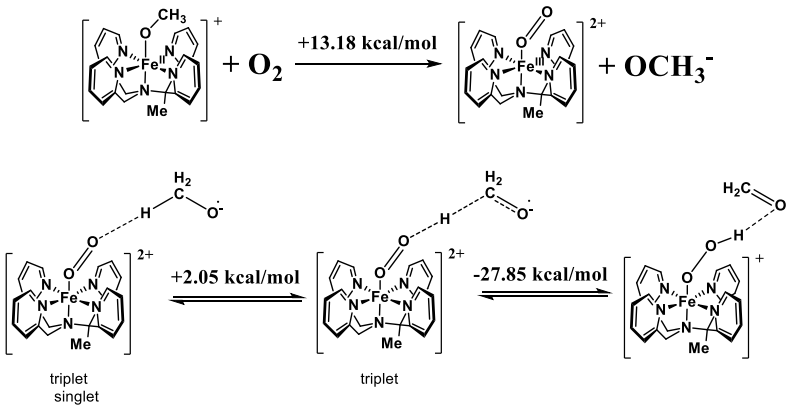

Figure 17 Reaction of the $[Fe(II)(MeN4Py)(OCH_3)]^+$ with O_2 in methanol.

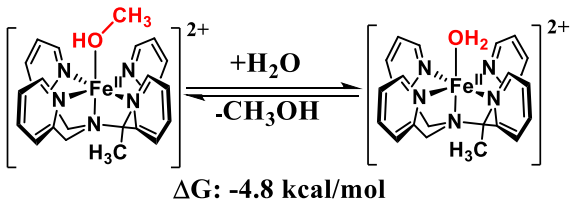

Figure 18 Free energy for exchange of methanol with water in methanol.

The presence of water, however, is noted as being essential for the activation by light to be observed, which indicates that in methanol, water facilitates ligand exchange also with O_2 (Figure 18). The exchanged of a hydroxide for a methoxido ligand is uphill also (ΔG = 3.7 kcal/mol).

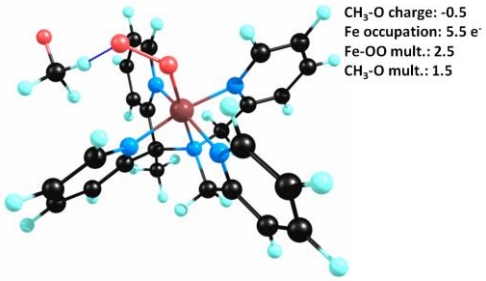

Figure 19 Depiction of the reaction between methanol and $[Fe(II)(MeN4Py)(OO)]^{2+}$ with Mulliken charges and spin distribution at this point indicated.

3.3 Conclusions

In this chapter, two mechanisms for the reaction of Fe(II) MeN4Py complexes with O_2 were explored. The relative energies of the singlet and quintet states of the Fe(II) complexes were found to be similar, in agreement with experimental observations. Notably the energy of the triplet states are sufficiently low to be thermally accessible, albeit that the steady state population is minimal. We have seen in this chapter that although the number of species that can be present in water is large, most probably the species present in the range of pH that is of interest in the context of DNA cleavage present a thermally accessible triplet state that can engage in either outer sphere electron transfer and hence rationalize the photo-enhancement of the reaction. On the other hand the study of possible ligand exchange reactions indicates that an Fe(II)-O_2 adduct may form and can simultaneously react with a methoxy anion. This latter

mechanism would lead ultimately via a Fe(II)-OOH to an Fe(IV)=O equivalent, i.e. two oxidation equivalents as delivered by the drug Fe(II)-Bleomycin. Future studies should focus on the calculation of the ISC probability between singlet, triplet and quintet states and the reactivity of all the species present in water with possible translation to developing alternative pathways for the oxidation of small molecules (methanol) or DNA.

3.4 Acknowledgements

Juan Chen is thanked for providing some of the experimental data discussed in this chapter.

3.4 Experimental

The computations were conducted using the Density Functional Theory (DFT) as implemented in the software package ADF 2014.[14, 15] The basis set used are Slater Type Orbitals (STOs) of quality TZ2P or TDZP which is constitute by a double-ζ basis for the metals and triple-ζ for the other lighter elements.[16, 17] The methods used to achieve reliable calculations of the free energies of the system are the following: Optimization and Themochemistry (using the QUILD[18] program as implemented in the ADF package): BP86-D_3[19, 20], ZORA /TDZP solvated in water unless mentioned otherwise (using COSMO[21]), Electronic Energies: S12g-D_3, ZORA/TZ2P solvated in water unless mentioned otherwise (COSMO). The functional S12g was used due to previous studies which indicated that good results are obtained given in the calculation of the separation in energy of spin states.[5] Density Functional Theory (TD-DFT) using the functional SAOP[22] in combination with TZ2P basis set. The solvent was included through the COSMO dielectric continuum model. In every calculation the core electrons were treated in a non-explicit way using the Frozen Core[14] approximation.

3.5 References

[1] For example see: a) R. P. Hanzlik, D. Williamson, *J. Am. Chem. Soc.,* **1976**, 98, 6570. b) A. Berkessel, J. W. Bats, C. Schwarz, *Angew. Chem. Int. Ed.,* **1990**, 29, 106.

[2] A. Draksharapu, Q. Li, H. Logtenberg, T. A. van den Berg, A. Meetsma, J. S. Killeen, B. L. Feringa, R. Hage, G. Roelfes, W. R. Browne, *Inorg. Chem*., **2012**, *51*, 900.

[3] A. Draksharapu, Q. Li , G. Roelfes, W. R. Browne, *Dalton Trans*., **2012**, 41, 13180.

[4] T. A. van den Berg , B. L. Feringa, G. Roelfes, *Chem. Commun*. **2007**, 180.

[5] M. Swart, *Chem. Phys. Lett.* **2013**, *580*, 166.

[6] J. Prakash, G.T. Rohde, K.K. Meier, A.J. Jasniewski, K.M. van Heuvelen, E. Münck, L. Que Jr., *J. Am. Chem. Soc.* **2015**, *137*, 3478.

[7] S.M. Hecht, Bleomycin: Chemical, *Biochemical and Biological Aspects*, Springer, New York, **1979**.

[8] G. Roelfes , M. E. Branum , L. Wang , L. Que Jr., B. L. Feringa*, J. Am. Chem. Soc.,* **2000**, 122, 11517.

[9] Q. Li, M. G. P. van der Wijst, H. G. Kazemier, M. G. Rots, G. Roelfes, *ACS Chem. Biol.,* **2014**, *9*, 1044.

[10] J. Stubbe, J.W. Kozarich, *Chem. Rev.*, **1987**, 87, 1107.

[11] a) Q. Li, T. A. van den Berg, B. L. Feringa, G. Roelfes, Dalton Trans., **2010**, *39*, 8012. b) R. P. Megens, T. A. van den Berg, A. D. de Bruijn, B. L. Feringa, G. Roelfes, *Chem.–Eur. J.*, **2009**, *15*, 1723.

[12] Q. Li, W. R. Browne, G. Roelfes, *Inorg. Chem*. **2011**, 50, 8318.

[13] B. H. J. Bielski, D. E. Cabelli, R. L. Arudi, A. B. Ross, *Phys. Chem. Ref.* **1985,** 14, 1041.

[14] Baerends et al. (version ADF2016); see also: G. te Velde, F. M. Bickelhaupt, E .J. Baerends, C. Fonseca Guerra, S. J. A. van Gisbergen, J. G. Snijders, T. Ziegler, *J. Comput. Chem.* **2001**, 22, 931.

[15] E. J. Baerends, T. Ziegler, J. Autschbach, D. Bashford, A. Berger, A. Bérces, F. M. Bickelhaupt, C. Bo, P. L. de Boeij, P. M. Boerrigter, S. Borini, R. E. Bulo, L. Cavallo, D. P. Chong, L. Deng, R. M. Dickson, A. C.

T. van Duin, D. E. Ellis, M. v. Faassen, L. Fan, T. H. Fischer, C. Fonseca Guerra, A. Ghysels, A. Giammona, S. J. A. van Gisbergen, A. W. Götz, J. A. Groeneveld, O. V. Gritsenko, M. Grüning, S. Gusarov, F. E. Harris, T. Heine, P. van den Hoek, C. R. Jacob, H. Jacobsen, L. Jensen, E. S. Kadantsev, J. W. Kaminski, G. van Kessel, R. Klooster, F. Kootstra, A. Kovalenko, M. V. Krykunov, E. van Lenthe, J. N. Louwen, D. A. McCormack, E. McGarrity, A. Michalak, M. Mitoraj, J. Neugebauer, V. P. Nicu, L. Noodleman, V. P. Osinga, S. Patchkovskii, P. H. T. Philipsen, D. Post, C. C. Pye, W. Ravenek, J. I. Rodríguez, P. Romaniello, P. Ros, P. R. T. Schipper, G. Schreckenbach, J. S. Seldenthuis, M. Seth, D. G. Skachkov, J. G. Snijders, M. Solà, M. Swart, D. Swerhone, G. te Velde, P. Vernooijs, L. Versluis, L. Visscher, O. Visser, F. Wang, T. A. Wesolowski, E. M. van Wezenbeek, G. Wiesenekker, S. K. Wolff, T. K. Woo, A. L. Yakovlev, *ADF2012.01*, (**2012**) SCM, Amsterdam.

[16] E. van Lenthe, E. J. Baerends, *J. Comput. Chem.,* **2003**, 24, 1142.

[17] D. P. Chong, E. van Lenthe, S. J. A. van Gisbergen, E. J. Baerends, *J. Comput. Chem*., **2004**, 25, 1030.

[18] M. Swart, F. M. Bickelhaupt, *J. Comput. Chem.*, **2008**, 29, 724.

[19] A. D. Becke, *Phys. Rev. A*, 1988, **38**, 3098.

[20] J. P. Perdew, *Phys. Rev. B*, 1986, **33**, 8822. Erratum: *Ibid*. 8834, 7406.

[21] A. Klamt, G. Schüürmann, *J. Chem. Soc., Perkin Trans. 2*, **1993**, 799.

[22] P. R. T. Schipper, O. V. Gritsenko, S. J. A. van Gisbergen, E. J. Baerends, *J. Chem. Phys.* **2000**, 112, 1344.

Chapter 4

Mechanistic links in the *in situ* formation of dinuclear manganese catalysts, H_2O_2 disproportionation and alkene oxidation

The oxidation of substrates, such as alkenes, with H_2O_2 with the catalyst $[Mn(IV,IV)_2(\mu\text{-}O)_3(tmtacn)_2]^{2+}$ (**1**) is promoted by the addition of carboxylic acids by in situ formation of bis-carboxylato complexes of the type $[Mn(III,III)_2(\mu\text{-}O)(\mu\text{-}RCO_2)_2(tmtacn)_2]^{2+}$. The conversion of **1** to these complexes requires a complex series of redox reactions coupled with overall exchange of μ -oxido for μ -carboxylato ligands. Here, we show that the mechanism by which this conversion takes place holds implications with regard to the species that is directly engaged in the catalytic oxidation of alkenes. Using a combination of UV/Vis absorption, Raman, resonance Raman and EPR spectroscopies, it is shown that the conversion proceeds via an autocatalytic mechanism and that the species that engages in oxidation of organic substrates also catalyses H_2O_2 decomposition, with the former process being the faster.

This chapter was published as .D. Angelone, S. Abdolahzadeh, J. W. de Boer, W. R. Browne, *Eur. J. Inorg. Chem*., **2015**, *21*, 3532

4.1 Introduction

The intimate connection between coordination mode and redox state that is observed in multinuclear manganese complexes lies at the core of the ability of biological systems to engage in redox catalysis, the most prominent examples being manganese based catalases,[1] superoxide dismutases[2] and the oxidation of water to molecular oxygen achieved in the oxygen evolving complex of PSII.[3] The coordination chemistry of multinuclear μ-oxido and μ-carboxylato bridged manganese complexes has therefore attracted extensive interest over the last decades due to their bioinorganic relevance[4,5] and their application in selective catalytic oxidations and in bulk oxidation chemistry.[6,7,8] In particular, in regard to catalytic activity of dinuclear manganese based enzymes,[9] there is an intimate connection between the cycle between redox states and changes in coordination mode, not least in regard to switching between μ-oxido and terminal hydroxide and aqua ligands and carboxylate shifts.[1b,10]

Manganese complexes based on the ligand 1,4,7- trimethyl-1,4,7-triazacyclononane (tmtacn), such as $[Mn(IV,IV)_2(\mu\text{-}O)_3(tmtacn)_2]^{2+}$ (**1**) and $[Mn(III,III)_2(\mu\text{-}O)(\mu\text{-}CH_3CO_2)_2(tmtacn)_2]^{2+}$ have received notable attention since the first reports by Wieghardt and coworkers,[11,12] in part due to their remarkably versatile redox dependent coordination chemistry and the discovery in the mid-1990s of their catalytic activity in the oxidation of organic substrates and stains.[13] A major drawback faced in using these complexes as oxidation catalysts, however, was the excessive disproportionation of H_2O_2. In the late 1990s, a fruitful search of potential additives led to the discovery that oxalate/oxalic acid,[14] ascorbic acid,[15] and more recently alkyl and aromatic carboxylic acids at co-catalytic levels[16,17] could suppress H_2O_2 disproportionation. Indeed, carboxylic acids, such as CCl_3CO_2H, enabled near complete efficiency in oxidant.[18]

Although the actual mechanisms by which oxalic and ascorbic acid enhance the activity of **1** towards selective oxidation of organic substrates remains unclear,[14,15,19] in the case of aliphatic and aromatic carboxylic acids it is clear that under reaction conditions **1** undergoes quantitative conversion to complexes of the type $[Mn(III,III)_2(\mu\text{-}O)(\mu\text{-}RCO_2)_2(tmtacn)_2]^{2+}$ through a complex series of redox and ligand exchange reactions (Scheme 1).[18] The presence of carboxylic acids resulted in suppression of disproportionation of H_2O_2, presumed to be by acting as a source of protons. Furthermore, it is apparent from the dependence of the selectivity of **1** (in regard to the epoxidation *vs*. *cis*-dihydroxylation of alkenes) on the sterics of the carboxylic acids[17] used and the observation of enantioselective oxidation with chiral carboxylic acids,[20] that the active catalytic species bears carboxylato ligands.

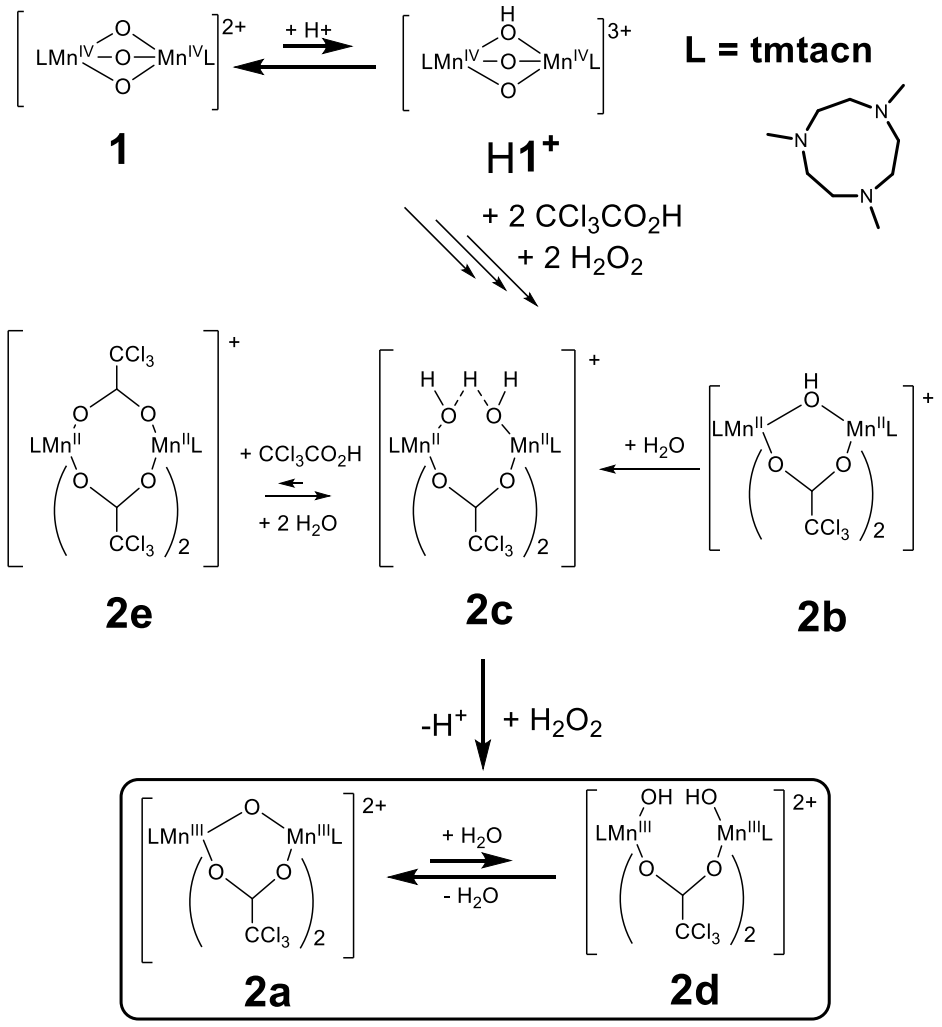

Scheme 1 Overall reaction of 1 with CCl_3CO_2H and H_2O_2 leading to the formation of 2a.[18]

Identification of the species that actually engages in oxygen transfer to the organic substrates, however, is challenging since the dominant species (>95%)[17] present under reaction conditions are of the type $[Mn(III,III)_2(\mu\text{-}O)(\mu\text{-}RCO_2)_2(tmtacn)_2]^{2+}$ with catalytically inactive Mn^{2+} ions present also. A key feature of the reactions involving **1** with carboxylic acids is that there is a substantial delay between the addition of H_2O_2 and the initiation of the conversion of **1** to, for example, $[Mn(III,III)_2(\mu\text{-}O)(\mu\text{-}CCl_3CO_2)_2(tmtacn)_2]^{2+}$ (**2a**). Furthermore, the sigmoidal, rather than exponential, shape of the curve indicated that the reaction is autocatalytic, i.e. an unknown species (**2x**) formed upon reduction of **1,** is itself involved in the further reduction of **1**.

In addition to the processes involved in the conversion of **1** to **2a**, an open question remains as to the initiation of the reaction. Since the species (**2x**), which is responsible for the autocatalysis, is formed only upon reduction of **1** then it is probable that the initiation step is either a spontaneous reduction event or triggered by other species. In this contribution, we explore the conversion of **1** to **2a** in detail using a combination of UV/Vis absorption, EPR, Raman and resonance Raman (rR) spectroscopies with the aim of elucidating the series of reactions that convert **1** to **2a** and in establishing whether or not the species involved during this process are of relevance to the catalysed oxidation of organic substrates also.

4.2 Results

UV/Vis absorption, FTIR, Raman and resonance Raman spectroscopy of 1 and 2

The synthesis and characterization of complexes **1**, **2a** and **2b** were described earlier.[11,12] The $Mn(II,II)_2$ complex **2b** does not show substantial UV/Vis absorption.[13] The $Mn(III,III)_2$ complex **2a**[12] and $Mn(IV,IV)_2$ complex **1**[11] both show strong absorption in the UV and visible regions (Figure 1). The visible absorption bands of **1** and **2a** are assigned to metal centred transitions, while the bands < 450 nm are assigned to ligand to metal charge transfer bands (vide infra).

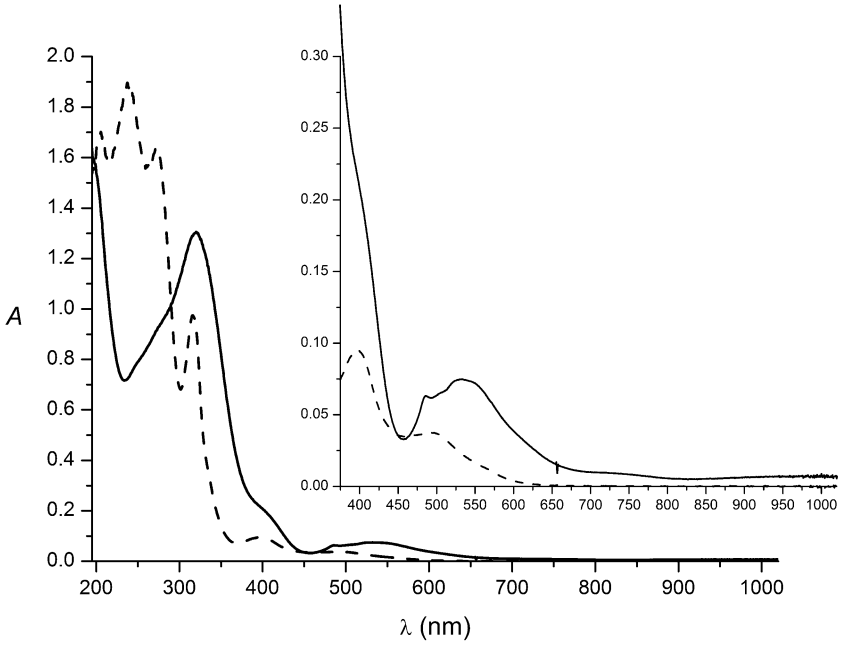

Figure 1 UV/vis absorption spectra of 1 (1 mM, dashed line) and 2a (1 mM, solid line), with CCl_3CO_2H (10 mM) in acetonitrile (1 mm pathlength). The inset shows an expansion of the visible region.

Assignment of the FTIR and Raman spectra of complexes **1**, **2a** and **2b** is facilitated by comparison with DFT calculated spectra (see supporting information) and, as expected, are similar with respect to bands associated with the tmtacn ligand but differ substantially in the low wavenumber region (Figures S1-3). Indeed, the modes associated with the $Mn(IV)(\mu\text{-}O)_3Mn(IV)$ and $Mn(III)(\mu\text{-}O)(\mu\text{-}RCO_2)_2Mn(III)$ cores of **1** and **2a**, respectively, dominate the resonance Raman spectra recorded at λ_{exc} 355 nm (Figure S4 and S5) and 457 nm at the same concentrations (1 mM) as employed[12,13] in the catalytic oxidation of alkenes (vide infra). The resonance Raman spectrum of **1** was reported earlier (in the solid state, λ_{exc} 457 nm) by Hage *et al*.[21] and showed enhancement of a band at 700 cm^{-1} assigned to the ν_{sym}(Mn-O-Mn) mode based on ^{18}O labelling. Raman spectra of **1** recorded in CH_3CN at λ_{exc} 355 nm and 457 nm show resonance enhancement primarily of low wavenumber modes (< 900 cm^{-1}) consistent with a μ-oxido to Mn^{IV} LMCT band. DFT and TD-DFT calculations on **1** confirm that the enhanced band at 700 cm^{-1} is due to a symmetric $Mn\text{-}(\mu\text{-}O)_3\text{-}Mn$ stretching mode. Assignment of the band at 799 cm^{-1} is less straightforward, however, but is likely to be due to Mn-N stretching modes or tmtacn ring breathing. For **2a**, significant resonance enhancement was observed, at 355 nm only, with a carboxylato bending mode at 790 cm^{-1} and additional weaker bands at 743 cm^{-1} (which overlaps with a band of acetonitrile, Figure 2) 1002, 1138, 1162, 1261 and 1293 cm^{-1} assigned to tmtacn

ligand modes. The latter bands are similar to those observed for **1**. In addition to the carboxylato based modes, relatively intense bands are observed between 420 and 520 cm^{-1}, which are assigned, based on DFT calculations, to symmetric and asymmetric breathing modes, respectively, involving the entire $Mn(III,III)_2$(μ-oxido)(μ-carboxylato) structure. The enhancement of predominantly carboxylato modes indicates that the absorption band at 350 nm is a carboxylato to Mn(III) charge transfer band. The UV/Vis absorption and resonance Raman spectra of **1** and **2a** (Figures S4 and S5, respectively) are unaffected by the addition of CCl_3CO_2H.

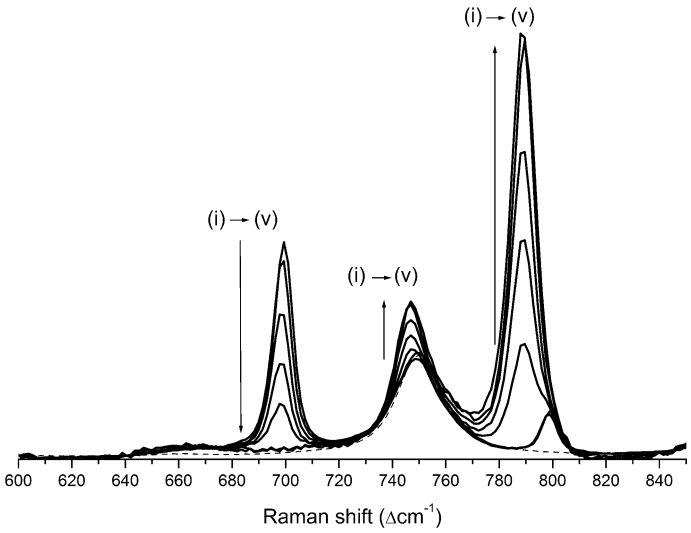

Figure 2 Resonance Raman spectra (λ_{exc} 355 nm) of varying mole fractions {(i) 1, (ii) 0.75, (iii) 0.5, (iv) 0.25 and (v) 0} of 1 w.r.t 2a in acetonitrile (dashed line) with CCl_3CO_2H (10 mM). Total concentration of 1 + 2a is 1 mM.

For **1** and **2a**, the redox potentials (in CH_3CN *vs* SCE) for reduction (0.2 V) and oxidation (1.4 V), respectively,[13] indicate that direct electron transfer between these complexes is not thermodynamically feasible. Indeed both in the absence and presence of CCl_3CO_2H, mixtures of these complexes are stable over several hours at room temperature and the UV/Vis absorption and rR spectra of a series of mole fraction mixtures match exactly to the spectra calculated by weighted summation of the individual spectra (Figure 2). Similarly, under reactions conditions, i.e. with 10 mM CCl_3CO_2H and 100 mM water in CH_3CN, **1**, **2a** and **2c** do not react with each other and are stable for several hours after mixing (Figure S6). These data exclude the possibility of direct electron transfer between the complexes.

Reaction monitoring with resonance Raman spectroscopy

The comparable degree of enhancement of the low wavenumber Raman bands of **1** and **2a** at 355 nm, at the concentrations employed in the catalytic oxidation of alkenes, allow the conversion from **1** to **2a** to be monitored quantitatively concomitant with the change in $[H_2O_2]$ (at 868 cm^{-1}, Figure 3).

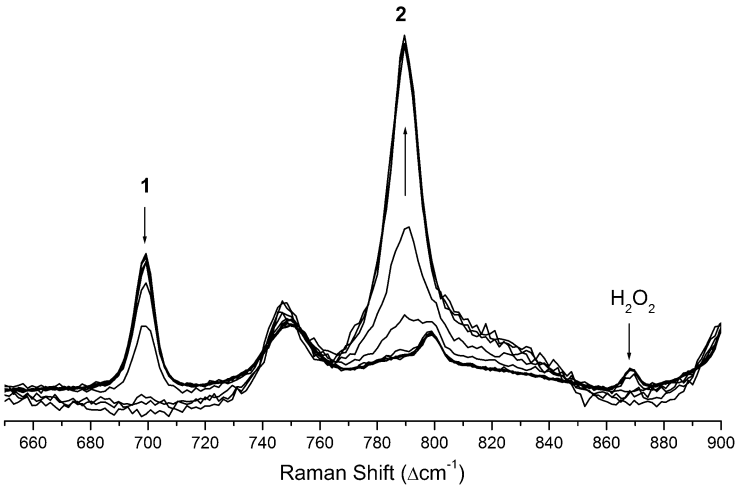

Figure 3 Raman spectra (λ_{exc} 355 nm) before, 10 s and then at 1000 s intervals after addition of 50 equiv. of H_2O_2 to a solution of 1 (1 mM) with CCl_3CO_2H (10 mM) in acetonitrile. Arrows indicate the direction of change in band intensity. Spectra have been normalised to the solvent band at 919 cm^{-1} to correct for changes in inner filter effects during the reaction.

Inspection of the time dependence of the changes in Raman intensity reveals an excellent correlation between the changes in intensity of the characteristic Raman bands of **1**, **2a** and H_2O_2, showing that the consumption of H_2O_2 and the conversion of **1** to **2a** proceed concomitantly. Notably, although 50 equiv. of H_2O_2 w.r.t. **1** were added, the consumption of H_2O_2 proceeds at a steady rate until **1** is consumed and continues thereafter until all H_2O_2 was consumed (Figure 4). The full consumption of the 50 equiv. of H_2O_2 during the period over which **1** converts to **2a** indicates that in that period a species capable of H_2O_2 disproportionation is present (vide infra).

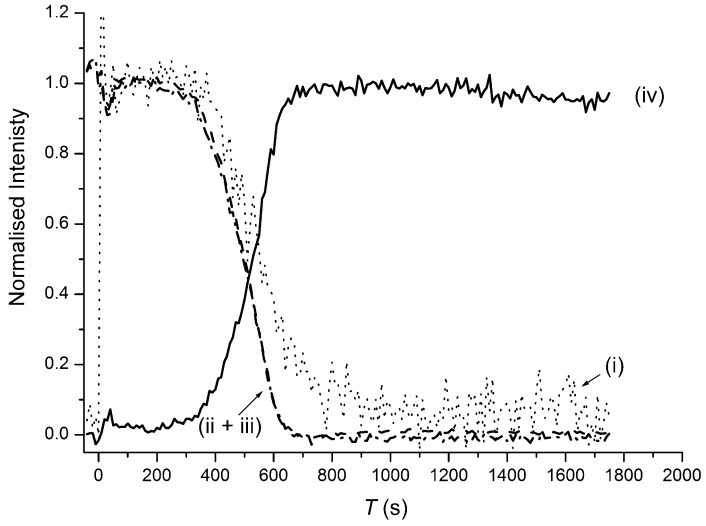

Figure 4 Change in normalised intensity of Raman scattering (λ_{exc} 355 nm) at (i) 868 cm^{-1} (H_2O_2) (ii) 700 cm^{-1} (1) (iii) 919 cm^{-1} (CH_3CN, a proxy for absorbance at 363 nm)[22] and (iv) 786 cm^{-1} (2a) after addition of 50 equiv of H_2O_2 to a solution of 1 (1 mM) with CCl_3CO_2H (10 mM) in acetonitrile.

Reaction monitoring with EPR spectroscopy

Although both complexes **1** and **2a** are silent to X-band EPR spectroscopy (at 77 K), the presence of complexes in other oxidation states, in particular Mn(II), Mn(IV), $Mn(II,II)_2$, $Mn(II,III)_2$ and $Mn(III,IV)_2$, should be manifested by the appearance of their characteristic EPR signals. The conversion of **1** to **2a** under standard conditions was monitored by UV/Vis spectroscopy with flash freezing of aliquots of the reaction mixture at specific times (Figure 5). The EPR spectra of the aliquots 1-4 are featureless. In the case of the spectra obtained at points 5 and 6 a very weak signal is observed that can be assigned tentatively to a 16 line species (the hyperfine coupling value a is ca. 76 G).[21] Between points 7 and 9 the characteristic 6 line signal of octahedral high spin Mn(II) appears and increases in intensity concomitant with the decrease and recovery in absorbance at 532 nm. Comparison of the EPR spectrum at point 9 with that of $Mn(II)(ClO_4)_2$ under similar conditions indicates that about 10% of the manganese is present as a mononuclear complex, presumably with loss of the tmtacn ligand, which is consistent with the absorbance at 532 nm, which is *ca*. 10% below that expected for full conversion of **1** to **2a**. Between points 9 and 10 the intensity of the six-line signal remains essentially constant, however, an additional weak 16 line signal appears also. Notably, the characteristic broad signal of **2c**[18] is not observed at any stage, indicating that it is not present in significant amounts.

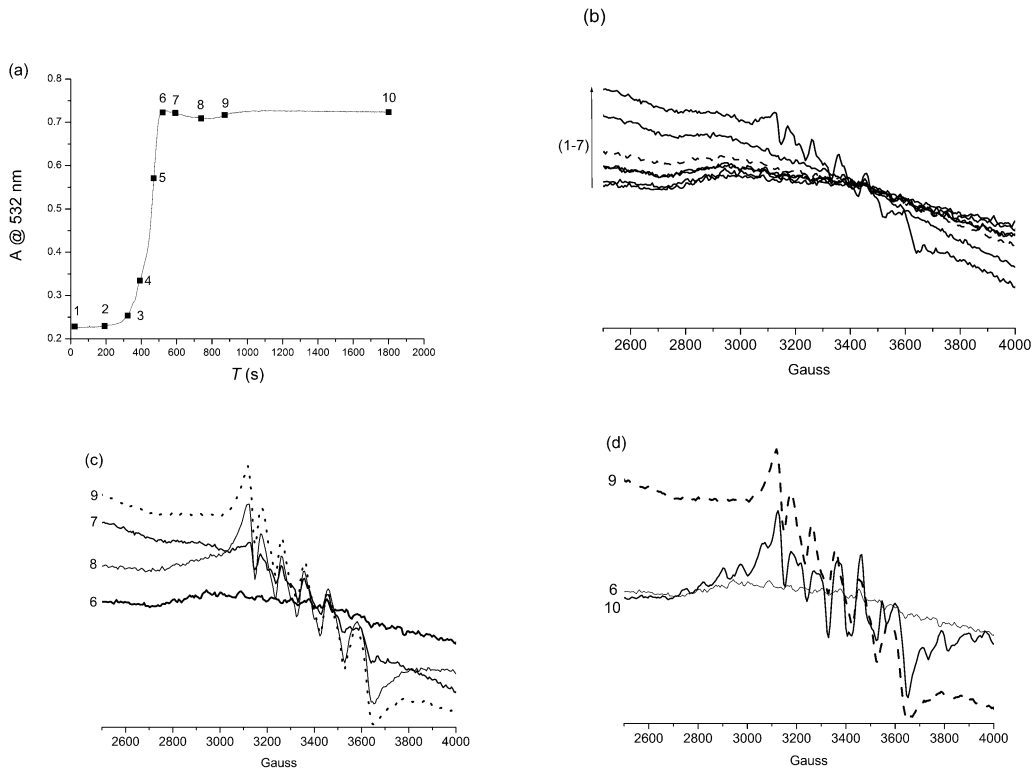

Figure 5 (a) Change in absorbance with time at 532 nm following the conversion of 1 to 2a and X-band EPR spectra (at 77 K) of aliquots of the reaction mixture flash frozen to 77 K at the time points (b) 1-7, (c) 6-9 and (d) 6, 9 and 10, as indicated in (a).

Origin of the lag time observed in the conversion of 1 to 2a

Although the duration of the lag-time observed in the conversion of **1** to **2a** is reproducible, i.e. the duration under standard conditions is 350 s +/- 15 s, it is highly sensitive to impurities and the presence of other metal ions and complexes.[23] Indeed, with a sample of **1** that had not

been recrystallized prior to use, a decrease in lag-time of 200 s was observed.[24] Addition of **2a**, the ultimate product, prior to addition of H_2O_2 results in only a marginal reduction in the lag-time even when present at a mole fraction of 0.5 and has relatively little effect on the reaction rate either (Figure 6).

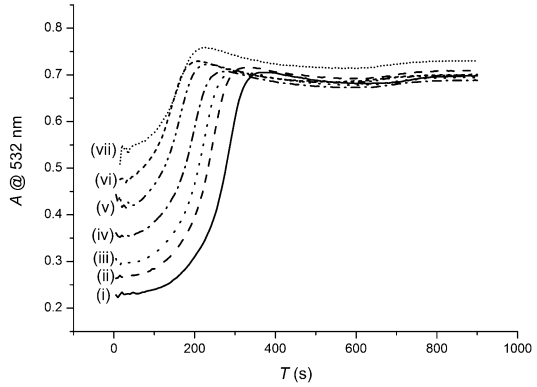

Figure 6 Absorbance at 532 nm over time after addition of 50 equiv. of H_2O_2 to 1 and 2a in acetonitrile with CCl_3CO_2H (10 mM). [1]+[2a] = 1 mM, mole fraction of 2a was (i) 0, (ii) 0.05, (iii) 0.1, (iv) 0.2, (v) 0.3, (vi) 0.4 and (vii) 0.5.

In contrast, even 0.01 equiv. of the Mn(II)Mn(II) complex **2b**, or a Mn(II) or Mn(III) salt results in a substantial decrease in the lag-time. It is clear, however, that regardless of the duration of the lag-time and the effect impurities or other complexes have on its duration, once initiated the reaction proceeds with almost identical kinetics (Figure 7). The disconnection between the lag-time and reaction kinetics once initiated[18] indicates that, regardless of the event that triggers the initial reduction of H**1**$^+$, the species formed upon reduction is much more effective at catalysing the further reduction of H**1**$^+$.

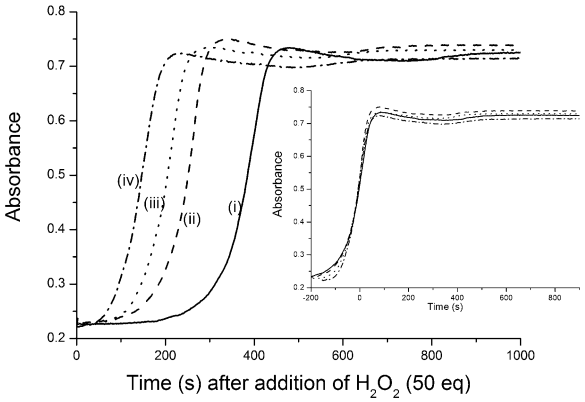

Figure 7 Absorbance at 532 nm over time after addition of 50 equiv. of H_2O_2 to a solution of (i) 1 (1 mM) with CCl_3CO_2H (10 mM) in acetonitrile and 1 with (ii) 2b (10 μM) (iii) $Mn(ClO_4)_2$ (20 μM) and (iv) $Mn(CH_3CO_2)_3$ (20 μM). Inset: overlay of curves with time offset to when the absorbance was 0.45.

Dependence of reaction rate on concentration of H_2O_2

Variation in the number of equiv. of H_2O_2 (5-100 equiv.) added w.r.t. **1** has a pronounced effect on the lag time, especially with less than 75 equiv. (Figure 8). The effect on lag time, however, is likely to be due to the concomitant variation in the amount of water added (vide infra). Notably,

however, once initiated, the reaction rate is relatively constant, indicating that the reaction is essentially zero order in H_2O_2, i.e. that the reaction of H_2O_2 with the species responsible for reducing H**1**$^+$ is a prior rapid equilibrium to the reduction of **1**. Furthermore, although complete consumption of the H_2O_2 present was observed in all cases (as determined by Raman spectroscopy), the conversion of **1** was essentially complete even with 10 equiv. of H_2O_2 (Figure 9).

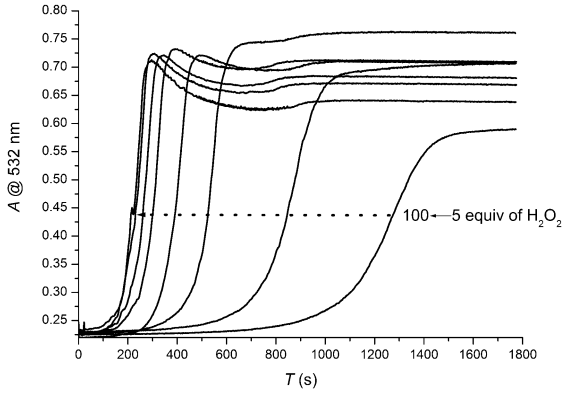

Figure 8 Absorbance at 532 nm over time after addition of (i) 5, (ii) 10, (iii) 25, (iv) 50, (v) 60, (vi) 75, (vii) 90 and (viii) 100 equiv. of H_2O_2 to a solution of 1 (1 mM) with CCl_3CO_2H (10 mM) in acetonitrile.

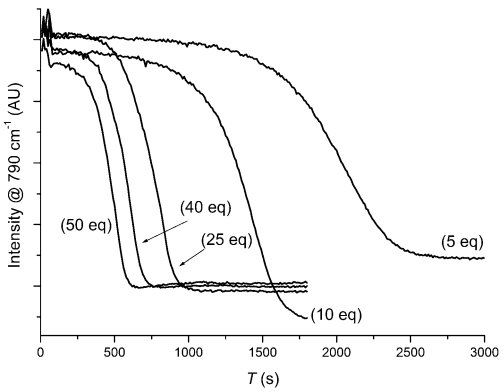

Figure 9 Intensity of the Raman band (λ_{exc} 355 nm) of 1 at 700 cm^{-1} over time after addition of (i) 5, (ii) 10, (iii) 25, (iv) 40 and (v) 50 equiv. of H_2O_2 to a solution of 1 (1 mM) with CCl_3CO_2H (10 mM) in acetonitrile.

It is notable that all of the H_2O_2 added initially is consumed during the conversion of **1** to **2a** but not before or after this process occurs. This correlation indicates that the species (**2x**) formed upon reduction of **1**, could be responsible for both the reduction of **1** and the disproportionation of H_2O_2. Previously,[18] it was demonstrated that whereas when **2a** is used directly in the catalytic oxidation of cyclooctene the efficiency in usage of H_2O_2 toward alkene oxidation was essentially complete, when **1** is used the reaction is systematically less efficient.[18] The systematic difference observed being the H_2O_2 that is disproportionated during the short period in which **1** undergoes conversion to **2a**.

Dependence of reaction on concentration of H_2O

The addition of excess water to the reaction (up to 150 mM) has relatively little influence on both the lag-time, the reaction rate and final yield of **2a** (Figure 10). Above 150 mM, an increase in the lag-time and a decrease in reaction rate was observed together with a decrease in the maximum absorbance at 532 nm, indicating that formation of **2a** is incomplete under these conditions. Notably, however, the absorbance reaches the same maximum at 650nm under all conditions except where a large of excess CCl_3CO_2H and water is present, which could indicate the formation of the non-μ-oxido bridged Mn(III)Mn(III) complexes, i.e. **2d**.[18]

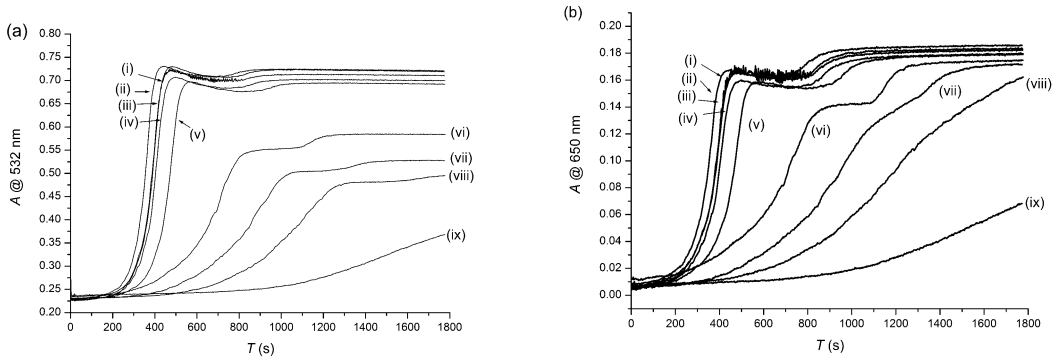

Figure 10 Absorbance at 532 nm and 650 nm over time after addition of 50 equiv. of H_2O_2 to a solution of 1 (1 mM) in acetonitrile with (i) 100 (i.e. that which is present in the 50 equiv. of H_2O_2 added), (ii) 120, (iii) 150, (iv) 180, (v) 200, (vi) 1000, (vii) 1500 and (viii) 1900 mM H_2O with CCl_3CO_2H (10 mM) and (ix) with 400 mM of H_2O and CCl_3CO_2H (100 mM).

Dependence of reaction on the concentration of CCl_3CO_2H

Typically 10 equiv. of carboxylic acid were employed for catalysis with **1**, however, it was noted earlier[18] that the concentration of carboxylic acid had only a modest effect on the catalytic oxidation of cyclooctene with **1**. Specifically, even two equiv. of CCl_3CO_2H were sufficient to achieve full activity initially, albeit with a loss of activity at later stages in the reaction. The lag time is affected only modestly with increasing acid concentration and notably the rate of reaction, once it has initiated, is essentially the same in all cases (Figure 11). The decrease in absorbance after the initial maximum is reached is noticeable in all cases and becomes especially pronounced at higher concentrations of CCl_3CO_2H. The dip and subsequent further recovery at higher concentration indicate that initial formation of a less coloured species, e.g., $[Mn(III,III)_2(OH)_2(\mu\text{-}Cl_3CO_2)_2(tmtacn)_2]^{2+}$ (**2d**) occurs initially, which subsequently converts to **2a** (vide infra). The rate of exchange of ^{18}O in **2a** has been determined by ESI-MS to be on the min time scale,[18] which is consistent with an equilibrium being established between **2a** and **2d**.

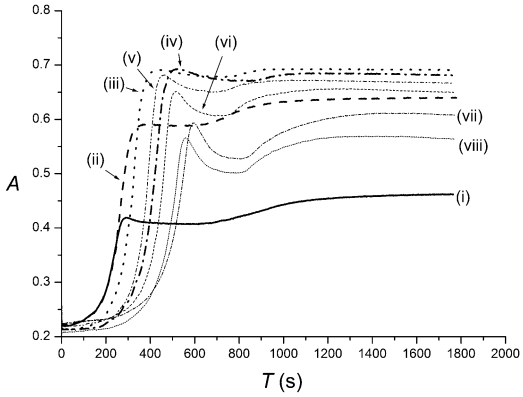

Figure 11 Absorbance at 532 nm over time after addition of 50 equiv. of H_2O_2 to a solution of 1 (1 mM) with (i) 1, (ii) 2, (iii) 5, (iv) 10, (v) 20, (vi) 50, (vii) 80 and (viii) 100 mM CCl_3CO_2H in acetonitrile.

When **1** was used with only 1 equiv. of CCl_3CO_2H, the conversion of cyclooctene (9%) was significantly less than when 2 equiv. of CCl_3CO_2H (59%) were present.[17] The large difference in the extent of alkene oxidation observed is surprising since even in the absence of CCl_3CO_2H, reasonable conversion (44%) of cyclooctene to its *cis*-diol and epoxide products were observed when **2a** was used as catalyst directly.[18]

When only 1 equiv. of CCl_3CO_2H w.r.t. **1** is available, only 50% conversion to **2a** is observed by both Raman (Figure 12b) and UV/Vis absorption spectroscopy (Figure 12a). Given that **2a** forms under these conditions, albeit with incomplete conversion of **1**, the limited conversion of the alkene is likely to be due, at least partly, to the decomposition of H_2O_2 (determined by Raman spectroscopy) catalyzed by reduction products of **1** in the absence of acid (note that all of the acid is consumed to form **2a**). Indeed, addition of a further 590 equiv. of H_2O_2 resulted in rapid disproportionation (monitored through the Raman band at 868 cm^{-1}) and ultimately the decomposition of **2a** (Figure 12). It is notable, however, that although excess H_2O_2 leads to destruction of **2a**, no further change in the concentration of **1** was observed.

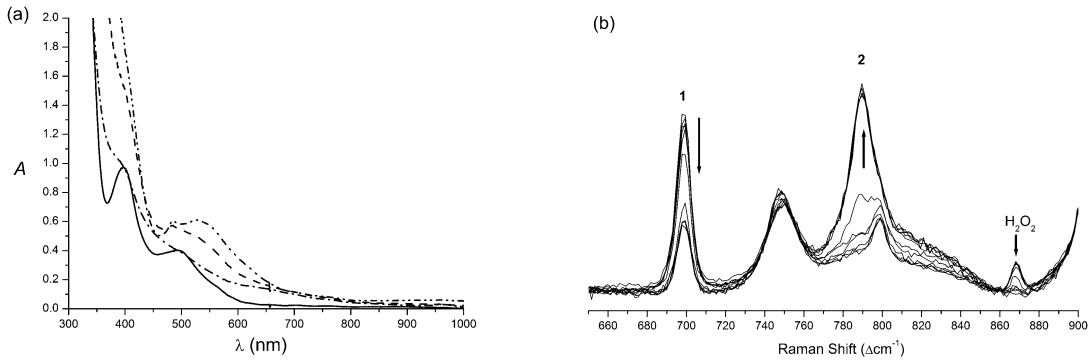

Figure 12 (a) UV/Vis absorption spectra of (solid line) 1 (1 mM) with CCl_3CO_2H (1 mM) in acetonitrile, (dashed line) 30 min after addition of 50 equiv. of H_2O_2 and (dash-dot line) 30 min after addition of 590 equiv. of H_2O_2. For comparison (dash-double dot), the spectrum 30 min after addition of 50 equiv. of H_2O_2 to 1 (1 mM) with CCl_3CO_2H (10 mM) in acetonitrile. (b) Raman spectrum (λ_{exc} 355 nm) of 1 (1 mM) with CCl_3CO_2H (10 mM) in acetonitrile at various times after addition of 50 equiv. of H_2O_2.

Inhibition of the conversion of 1 to 2a by cyclooctene

The lag time before conversion of **1** to **2a** begins is affected to a minor extent (< double) even with 0.5 M cyclooctene present. The observed rate of conversion of **1** to **2a**, however, is decreased dramatically and takes on the appearance of a 1st order rather than autocatalytic reaction (Figure 13). The retardation in reaction rate is not linearly dependent on cyclooctene concentration and indeed gives the appearance of saturation kinetics at higher concentrations. A further effect of addition of even only 10 equiv. of cyclooctene is that the overall yield of **2a** is higher (essentially full conversion to **2a**) and the additional process observed between 1000 and 2000 s (i.e. the decrease and then increase in absorbance is not observed with 50 or more equivalents of H_2O_2).

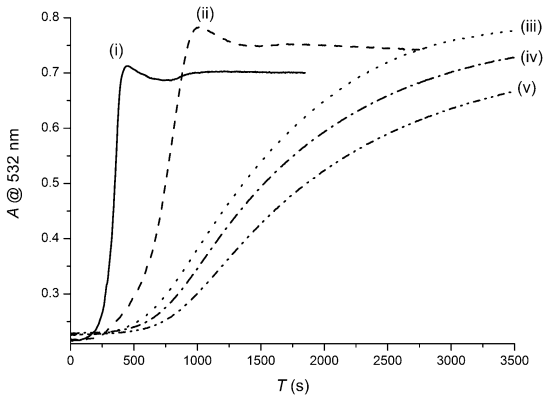

Figure 13 Absorbance at 532 nm over time after addition of 50 equiv. of H_2O_2 to a solution of 1 (1 mM) with CCl_3CO_2H (10 mM) in acetonitrile with (i) 0, (ii) 10, (iii) 50 (iv) 100 and (v) 500 mM cyclooctene.

Importantly, the full conversion of **1** to **2a** even with high concentrations of cyclooctene, which slows down the reaction significantly, suggests that H_2O_2 disproportionation is retarded also. The decrease in H_2O_2 disproportionation in the presence of cyclooctene is consistent with the involvement of species **2x** in both H_2O_2 disproportionation as well as alkene oxidation. It is notable also that addition of H_2O_2 to the Mn(II)Mn(II) complex **2b** results in rapid conversion to **2a**, the rate of which is retarded by addition of cyclooctene.[18]

Disproportionation of H_2O_2 by 2a

Although the efficiency with respect to the use of H_2O_2 to convert organic substrates is near unity,[18] in the absence of organic substrates, **2a** engages in relatively efficient H_2O_2 decomposition (Figure 14) at approximately the same rate as seen during the conversion of **1** to **2a** (Figure 4). Notably, the absorbance at 532 nm (and hence concentration of **2a**) decreases concomitantly with the decomposition of H_2O_2 and subsequently recovers to a limited extent. These data confirm that **2a** is capable, albeit with a low turnover frequency, of catalytic disproportionation of H_2O_2.

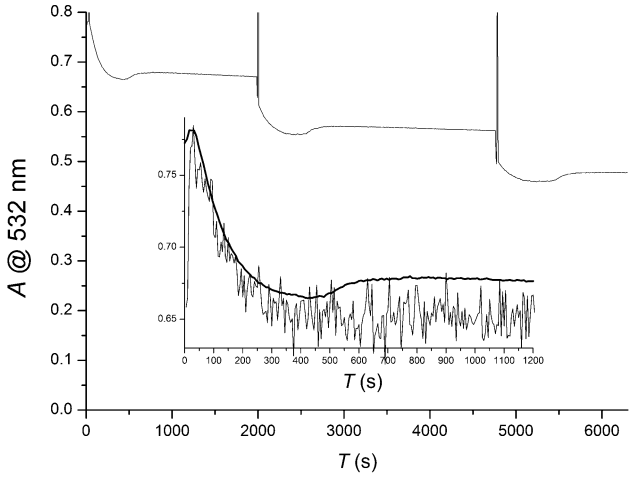

Figure 14 Absorbance at 532 nm over time after repeated addition of 50 equiv. of H_2O_2 to a solution of 2 (1 mM) with CCl_3CO_2H (10 mM) in acetonitrile (the spikes in absorbance denote the points of addition of H_2O_2). Inset: overlay of absorbance at 532 nm (thick line) and intensity of the Raman band (λ_{exc} 473 nm, thin line) at 869 cm^{-1}.

4.3 Discussion

The conversion of **1** to **2a** involves overall two electron reduction and exchange of two μ-oxido ligands for two μ-carboxylato ligands. It is evident that the conversion proceeds through a series of redox and ligand exchange events. The most obvious features of the conversion are that there is a lag-time before the reaction begins and that once initiated, it proceeds in an autocatalytic manner, i.e. a sigmoidal rather than exponential time dependence in the change in absorbance (e.g., Figure 4). In addition, further processes are observed after the conversion of **1** is complete.

The lag-period is highly sensitive to the presence of Mn(II) and Mn(III) ions. Indeed trace impurities can have a dramatic effect on its duration. Nevertheless, the duration of the lag period is highly reproducible provided precautions[24] are taken to ensure that reaction vessels are free of contaminants.

The duration of the lag-period has relatively little, if any, effect on the subsequent kinetics of the conversion of **1** to **2a**. Although an excess (at least 10 equiv. w.r.t. **1**) of H_2O_2 is required to achieve full conversion, with the remainder being disproportionated, consumption of H_2O_2 is only observed once the conversion of **1** to **2a** has initiated. Hence, it is apparent that, regardless of the event that initiates conversion, once the reduction of **1** has begun, the species then formed is much more efficient at catalyzing the reduction of **1** with H_2O_2.

Once initiated, the conversion of **1** to **2a** appears to be essentially direct in the sense that EPR active species are not observed until conversion nears completion and the increase in the intensity of the Raman bands of **2a** track exactly the decrease in the bands of **1** (Figure 4). Furthermore, the rate of the reaction is relatively insensitive to the concentration of H_2O_2, water and CCl_3CO_2H, except when present in gross excess, indicating that the reaction is zero order in all three components. The consequence of this is that the rate determining step must be the reduction of **1** by a relatively stable species (**2x**). A possible candidate for **2x** is the species

formed upon reaction of **2d** with H_2O_2 in a prior rapid equilibrium (i.e. $[Mn(III,III)_2(OH)(OOH)CCl_3CO_2)_2(tmtacn)_2]^{2+}$. The subsequent reactions that lead to **2a** are much faster than the rate of reduction. A complication that precludes a detailed kinetic analysis is that in addition to the reduction of **1**, **2x** is active in the disproportionation of H_2O_2 at a rate that is several times higher. Importantly, direct electron transfer between **2a** or **2c** to **1** has been excluded.

Mn(II) ions are formed during the reaction and are apparent especially at later stages (Figure 5). However, it is unlikely that Mn(II) ions are involved in the reactions observed as neither $Mn(II)(ClO_4)_2$ nor $Mn(III)(OAc)_3$ show H_2O_2 decomposition or cyclooctene oxidation in acetonitrile in the presence of excess CCl_3CO_2H. Furthermore **1** is unreactive in regard to H_2O_2 decomposition in the presence of an inorganic acid such as HPF_6. Notably, although 50% conversion of **1** to **2a** was observed with only 1 equiv. of CCl_3CO_2H (Figure 12), H_2O_2 underwent rapid disproportionation and eventually decomposition of **2a** was observed with no further change to **1**.

The involvement of Mn(II)Mn(II) complexes, such as complex **2b**, **2c** and **2e** can be excluded also for several reasons: **2b** undergoes immediate conversion to **2c** upon addition of acid and addition of H_2O_2 to **2c** in the presence of CCl_3CO_2H results in fast conversion to **2a** (Scheme 2). Notably, however, the conversion from **2c** to **2a** is retarded by the presence of cyclooctene (Figure 13 and Scheme 2).[18]

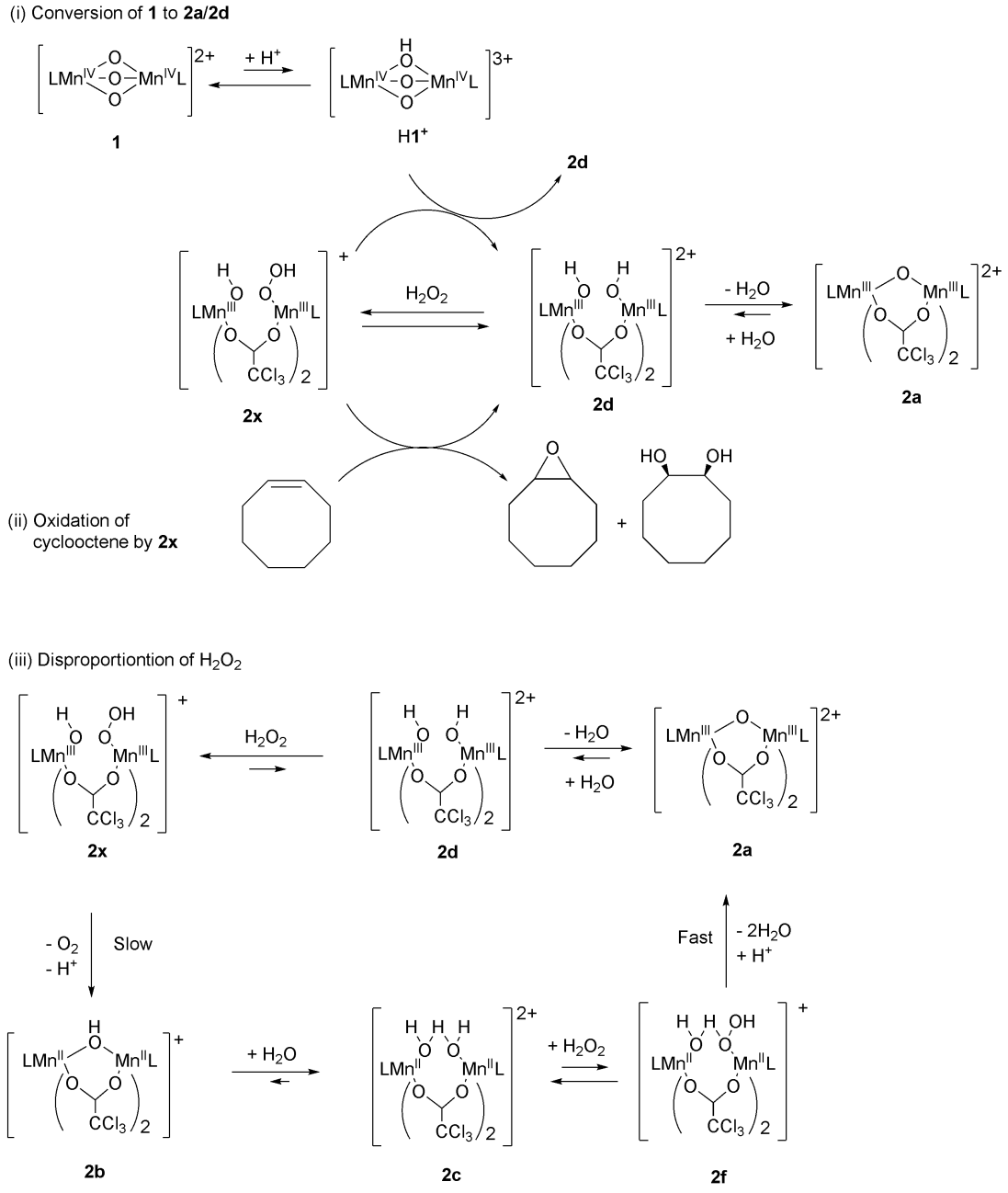

Scheme 2 Proposed mechanisms for the reaction of 2a/2d with H_2O_2 to form 2x and the subsequent reaction of 2x with (i) 1 and (ii) cyclooctene. (iii) Porposed mechanism for disproportionation of H_2O_2.

Although most experimental factors have relatively modest effects on the conversion of **1** to **2a**, cyclooctene is an exception. The addition of even 500 equiv. of cyclooctene has only a modest effect on the lag time, but even 10 equiv. impacts the rate of conversion of **1** and the efficiency in regard to the amount of **2a** formed. Indeed at above 50 equiv. w.r.t. **1** the change in absorbance is no longer sigmoidal but pseudo-exponential instead. Furthermore, essentially full conversion to **2a** is observed even with only 10 equiv. of cyclooctene, which indicates that the processes observed subsequent to full conversion of **1** are suppressed.

The third stage of the reaction, i.e. after **1** has undergone full conversion, relates to the coordination chemistry of **2a** primarily and to its limited ability to disproportionate H_2O_2. It is notable that addition of excess water and/or CCl_3CO_2H to **2a** results in the formation of **2d**, the

Mn(III)Mn(III) analogue of **2c**.[18] Indeed, preparative electrochemical reduction of **1** in the presence of CCl_3CO_2H has been shown earlier to lead to the formation of **2d** rather than **2a**.[18]

2a is relatively stable in the presence of excess H_2O_2, i.e. the concentration of **2a** decreases by at most 15% upon addition of 50 equiv. of H_2O_2. The disproportionation of H_2O_2 by **2a** is relatively slow, even in the absence of cyclooctene, and once complete a partial recovery in absorbance is observed which is consistent with the initial formation of **2d**. H_2O_2 disproportionation, as proposed for dinuclear manganese catalases,[1] involves sequential two electron reduction and subsequent two electron oxidation of the dinuclear manganese unit. It is evident that the Mn(II)Mn(II) complex **2c** can undergo oxidation to **2a**, tentatively via the non-μ-oxido bridged Mn(III)Mn(III) analogue **2d**. Such a mechanism is analogous to the operation of dinuclear manganese catalases[1] in which the redox state is cycled between Mn(II)Mn(II) and Mn(III)Mn(III) while oxidising and then reducing H_2O_2 (Scheme 2iii). The relatively slow rate of the reduction of **2a** to **2c** is likely, however, to be due to the equilibrium position between **2a** and **2d** rather than the lack of substantial structural change, since oxidation of **2c** to **2d** results in deprotonation and a decrease in redox potential by 300 mV.[18]

The effect of cyclooctene on both the rate of oxidation of **2c** to form **2a** and extent of H_2O_2 disproportionation suggests that a competitive inhibition mechanism is operating. The reduction from Mn(III)Mn(III) (**2x**) to Mn(II)Mn(II) (**2c**) with release of dioxygen must therefore be slower than the bimolecular reactions of **2x** with H**1**$^+$ and with cyclooctene. The reaction with H**1**$^+$, ultimately, yields more **2d**/**2a** and accelerates the reaction while the reaction with cyclooctene is likely to produce **2a**,[18] which then has to undergo opening of the μ-oxido bridge before coordination of H_2O_2 takes place.

4.4 Conclusions

In summary, it is apparent that the conversion of **1** to **2a** involves an initiation step, i.e. the reduction of H**1**$^+$, in order to proceed, however, the initial product of the reduction and ligand exchange reactions (**2a**/**2d**) can react readily with H_2O_2 to form **2x**, which is likely to be the species responsible for the further reduction of H**1**$^+$ (Scheme 2(i)). The rate at which the reaction proceeds is remarkable considering that under the conditions employed, the negative pK_a of **1** means that relatively little of the reducible complex is available. It is also likely that **2x** is also the species directly responsible for the oxidation of alkenes (Scheme 2(ii)). Indeed, the inhibitory effect of cyclooctene, even with only 10 equiv. present, on the rate of conversion of **1** to **2a** is expected considering that the reaction between **2x** and the alkene leads to **2a** and the epoxide/*cis*-diol product. The relative inertness of **2a** towards H_2O_2 means that this latter reaction is effectively a termination step in the conversion of **1** to **2a**.

The identification of an 'active catalytic species' and the development of a detailed model (i.e. a series of elementary steps) for a reaction requires an intimate understanding of not only the catalyst and its behavior under reaction conditions but also the factors that influence its reactivity and stability. In the present example the role played by redox state driven changes in coordination is clear in the conversion of **1** to the catalytically competent complex **2a**. In our search for the structure of the species directly responsible for the oxidation of organic substrates, close examination of the conversion of **1** to **2a** is warranted and as is demonstrated

in the present study, can reveal direct connections between the reduction of **1** and the oxidation of alkenes. Furthermore, it is clear that it is not the presence of carboxylic acids that suppresses H_2O_2 disproportionation, but instead the reaction between **2x** and substrate, e.g., cyclooctene, to form **2a** is faster than release of molecular oxygen to form **2c**.

4.5 Experimental Section

All reagents were obtained from commercial sources and used as received unless stated otherwise. H_2O_2 (50% v/v) in water was obtained from Acros. Complexes **1** ($[Mn(IV,IV)_2O_3(tmtacn)](PF_6)_2$), **2a** ($[Mn(III,III)_2(\mu\text{-}O)(\mu\text{-}CCl_3CO_2)_2(tmtacn)_2](PF_6)_2$), **2b** ($[Mn(II,II)_2(\mu\text{-}OH)(\mu\text{-}CCl_3CO_2)_2(tmtacn)_2](ClO_4)$) were available from earlier studies.[17] UV/vis absorption spectra were recorded using a Specord S600 UV/vis absorption spectrometer in 1 cm quartz cuvettes unless stated otherwise. X-band EPR spectra (9.47 GHz, Bruker ECS102) were recorded in 3 mm quartz tubes at 77 K with 2 G modulation and 81 ms conversion time. Raman spectra were recorded at 355 nm and 457 nm in backscattering mode as described earlier,[25] and at 785 nm using a Perkin Elmer Ramanstation. ATR-FTIR spectra were recorded using a Perkin Elmer Spectrum400 FTIR spectrometer equipped with a UATR attachment. All experiments were performed at 19 ^{o}C unless stated otherwise.

Computational methods

Simulation of Raman and IR spectra were performed using Density Functional Theory (DFT) as implemented in Gaussian 09c[26] using the B3LYP functional and a basis set composed by LANL2TZ+(f)[27] for manganese atoms and 6-311G(d,p)[28] for the remaining atoms after geometry optimization at the same level of theory. Resonance Raman spectra were calculated as implemented in ORCA 3.0.2. [29] Optimization was achieved using the BP86 functional[30] and Def2-TZVP[31] basis set, while the calculation of the Hessian matrices were performed using 6-311G(d,p) for H, C, N, O, Cl elements. The TD-DFT calculations were performed with a BH and HLYP functional and using the same basis set used to calculate the Hessian matrix. See the supporting information for coordinates of calculated structures. Optimized cartesian xyz coordinates for calculations using uB3LYP/6-311G(d,p)/LANL2TZ+(f) (Only For Mn) in Gaussian are available online – in published version of this chapter.

4.6 References

[1] (a) V. V. Barynin, M. M. Whittaker, S. V. Antonyuk, V. S. Lamzin, P. M. Harrison, P. J. Artymiuk, J. W. Whittaker, *Structure* **2001**, *9*, 725; (b) J. W. de Boer, W. R. Browne, B. L. Feringa, R. Hage, *C. R. Chimie* **2007**, *10*, 341.

[2] D. W. Christianson, *Prog. Biophys. Molec. Biol*., **1997**, *67*, 217.

[3] J. Barber, *Chem. Soc. Rev*. **2009**, *38*, 185.

[4] S. J. Lippard, J. M. Berg, Principles of Bioinorganic Chemistry, University Science Books, Mill Valley, California., **1994**.

[5] S. Mukhopadhyay, S.K. Mandal, S. Bhaduri, W. H. Armstrong, *Chem. Rev*., **2004**, *104*, 3981.

[6] Modern Oxidation Methods, 2nd ed., (Ed.: J.-E. Backvall) Wiley-VCH, Weinheim, **2010.**

[7] P. Saisaha, J. W. de Boer, W. R. Browne, *Chem. Soc. Rev*. **2013**, *42*, 2059.

[8] K. F. Sibbons, K. Shastri, M. Watkinson, *Dalton Trans.* **2006**, *5*, 645.

[9] G. C. Dismukes, *Chem. Rev.* **1996**, 96, 2909.

[10] M. Shank, V. Barynin, G. C. Dismukes, *Biochemistry* **1994**, *33*, 15433.

[11] (a) K. Wieghardt, U. Bossek, D. Ventur, J. Weiss, *J. Chem. Soc., Chem. Commun.* **1985**, 347. (b) K. Wieghardt, U. Bossek, B. Nuber, J. Weiss, J. Bonvoisin, M. Corbella, S. E. Vitols, J. J. Girerd, *J. Am. Chem. Soc*. **1988**, *110*, 7398.
[12] K. Wieghardt, U. Bossek, J. Bonvoision, P Beauvillian, J. J. Girerd, B. Nuber, J. Weiss, J. Heinze, *Angew. Chem., Int. Ed. Engl*. **1986**, *25*, 1030.
[13] R. Hage, J. E. Iburg, J. Kerschner, J. H. Koek, E. L. M. Lempers, R. J. Martens, U. S. Racherla, S. W. Russell, T. Swarthoff, M. R. P. Van Vliet, J. B. Warnaar, L. Van Der Wolf, B. Krijnen, *Nature*, **1994**, *369*, 637.
[14] D. E. De Vos, B. F. Sels, M. Reynaers, Y. V. S. Rao P. A. Jacobs, *Tetrahedron Lett*. **1998**, *39*, 3221.
[15] A. Berkessel, C. A. Sklorz, *Tetrahedron Lett*. **1999**, *40*, 7965.
[16] G. B. Shul'pin, G. Suss-Fink, J. R. L. Smith, *Tetrahedron* **1999**, *55*, 5345.
[17] J. W. de Boer, J. Brinksma, W. R. Browne, A. Meetsma, P. L. Alsters, R. Hage, B. L. Feringa, *J. Am. Chem. Soc.* **2005**, *127*, 7990.
[18] J. W. de Boer, W. R. Browne, J. Brinksma, P. L. Alsters, R. Hage, B. L. Feringa, *Inorg. Chem*. **2007**, 6353.
[19] J W. de Boer, P. L. Alsters, A. Meetsma, R. Hage, W. R. Browne, B. L. Feringa, *Dalton Trans.* **2008**, *44*, 6283.
[20] J. W. de Boer, W. R. Browne, S. R. Harutyunyan, L. Bini, T. D. Tiemersma-Wegman, P. L. Alsters, R. Hage, B. L. Feringa, *Chem. Commun*. **2008**, 3747.
[21] R. Hage, B. Krijnen, J. B. Warnaar, F. Hartl, D. J. Stufkens, T. L. Snoeck, *Inorg. Chem*. **1995**, *34*, 4973.
[22] The increase in absorption between 355 and 400 nm over the course of the reaction results in an increase in inner filter effect, and hence a decrease in overall spectral intensity. Therefore the decrease in the intensity of the solvent band at 919 cm^{-1} (367 nm) acts as a good proxy for the change in absorbance in that region.
[23] The possibility of photochemical processes induced by the spectrometers or laser irradiation can be excluded since all complexes (**1** and **2a**) are stable in solution with CCl_3CO_2H even under irradiation at 355 nm (10 mW) for several hours.
[24] It should be noted that rigorous cleaning of cuvettes and glassware (washing with acetone, thrice demi-water, soaking for 10 min in aqua regia (HCl/HNO_3 1:1 v/v) followed by doubly distilled water and then UVASOL grade acetonitrile) was required to obtain a repeatable lag-time.
[25] S. Abdolahzadeh, N. M. Boyle, M. L. Hoogendijk, R. Hage, J. W. de Boer, W. R. Browne, *Dalton Trans.* **2014**, *43*, 6322.
[26] Gaussian-09, Revision C.01, Gaussian Inc., Wallingford CT, **2010**.
[27] D. Feller, *J. Comp. Chem.* **1996**, *17*, 1571.
[28] R. Krishnan, J.S. Binkley, R. Seeger, J.A. Pople, *J. Chem. Phys*. **1980**, *72*, 650.
[29] (a) F. Neese, *WIREs Comput. Mol. Sci.*, **2012**, *2*, 73; (b) T. Petrenko, F. Neese, *J. Chem. Phys.* **2007**, *127*, 164319.
[30] (a) A. D. Becke, *Phys. Rev. A* **1988**, *38*, 3098; (b) J. P. Perdew, *Phys. Rev. B*, **1986**, *33*, 8822.
[31] A. Schaefer, H. Horn, R. Ahlrichs, *J. Chem. Phys.* **1992**, *97*, 2571.

4.7 Supporting information

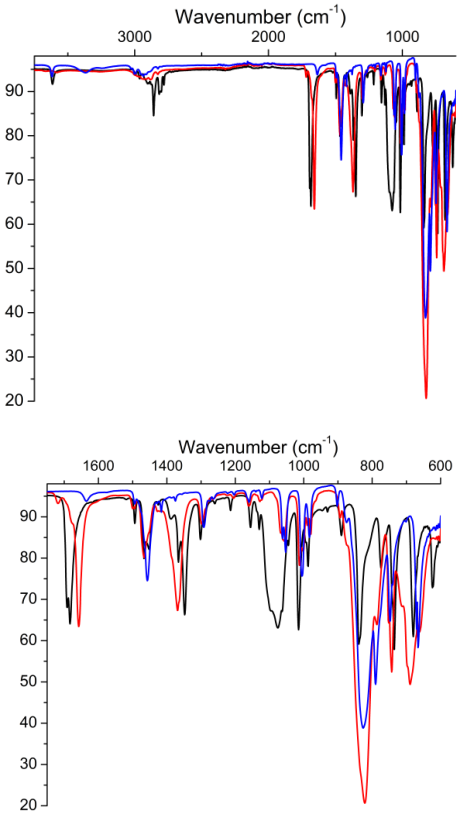

Figure S1 Solid state ATR-FTIR spectra (λ_{exc} 785 nm) of 1 (blue), 2a (red) and 2b (black).

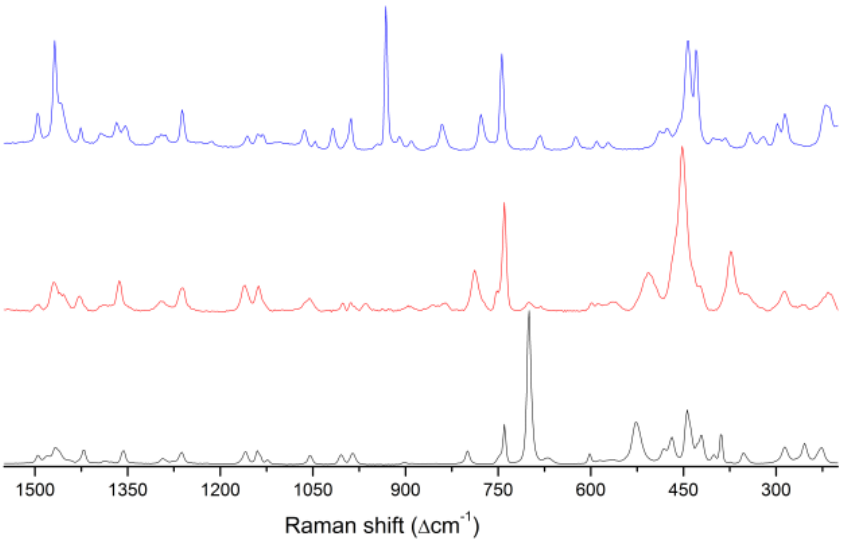

Figure S2 Solid state Raman spectra (λ_{exc} 785 nm) of 1 (black), 2a (red) and 2b (blue).

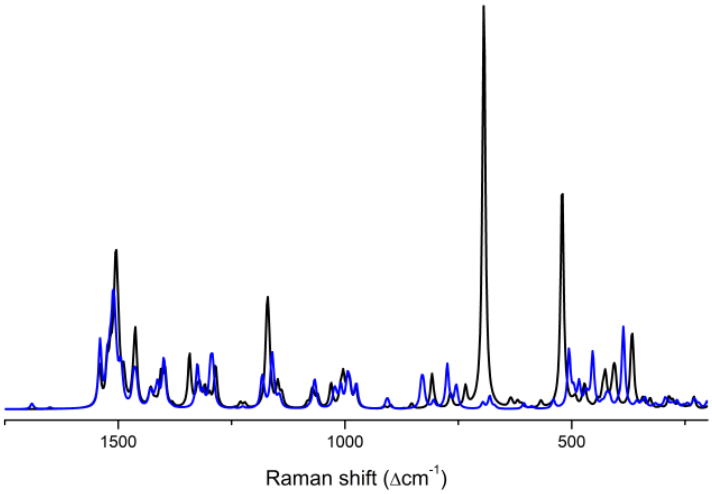

Figure S3 DFT calculated Raman spectra of 1 (1 mM, black) and 2a (1 mM, blue).

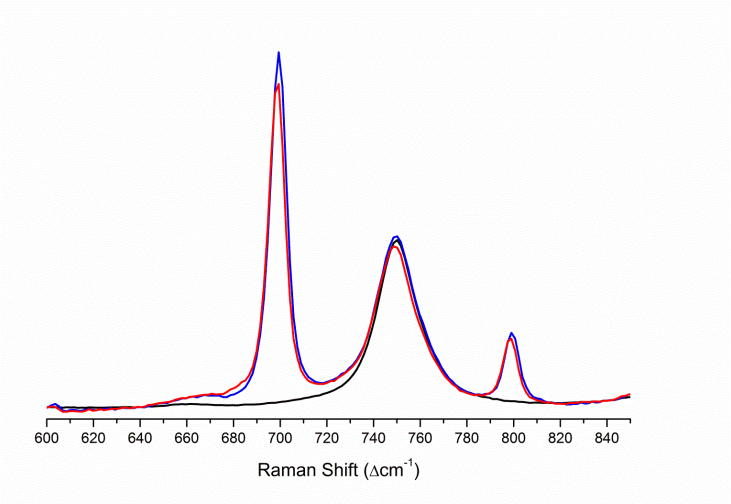

Figure S4 Resonance Raman spectra (λ_{exc} 355 nm) in acetonitrile (black line) of 1 (1 mM) without (blue line) and with (red line) CCl_3CO_2H (10 mM).

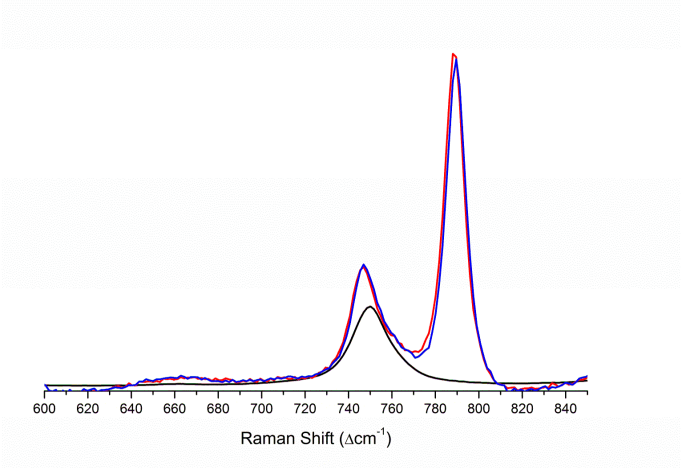

Figure S5 Resonance Raman spectra (λ_{exc} 355 nm), in acetonitrile (black line), of 2a (1 mM) without (red line) and with (blue line) CCl_3CO_2H (10 mM).

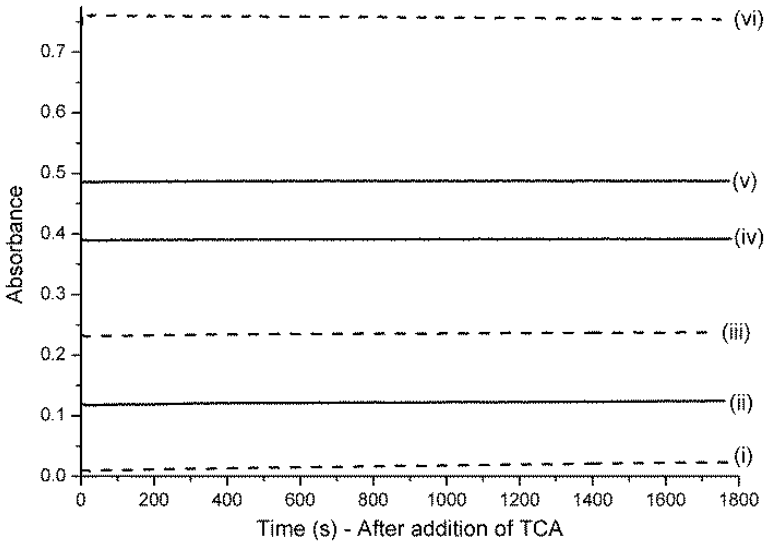

Figure S6 Absorbance at 532 nm of (i) 2b (1 mM), (ii) 2b (0.5 mM) and 1 (0.5 mM), (iii) 1 (1 mM), (iv) 2a (0.5 mM) and 2b (0.5 mM), (v) 1 (0.5 mM) and 2a (0.5 mM) and (vi) 2a (1 mM), in acetonitrile with CCl_3CO_2H (10 mM) and water (100 mM).

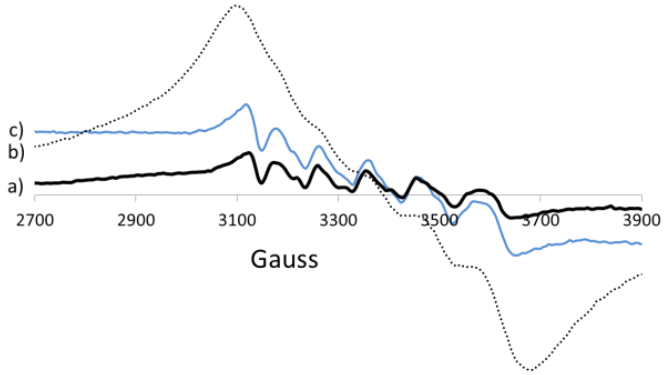

Figure S7 X-band EPR spectra (at 77 K) of $Mn(II)(ClO_4)_2$ (a) 0.2 mM and (b) 2 mM in CH_3CN with 10 mM CCl_3CO_2H and (c) of the aliquot drawn at point 9 in Figure 5

Chapter 5

Elucidation of the mechanism of manganese catalysed oxidation of alkenes in aqueous media at high pH

The oxidation of substrates, such as water soluble alkenes, with H_2O_2 with the catalyst $[Mn(IV,IV)_2(\mu\text{-}O)_3(tmtacn)_2]^{2+}$ (**1**) is studies in this chapter with the goal of elucidating the role of both 'free' Mn(II) ions and carbonate as a buffer. The chapter focuses on the effect of buffers, concentration and sequestrant on catalytic activity. The main finding is that mechanistic studies must recognize the possibility of concurrent catalytic processes being involved and consideration of the effect this has on results gained with variation in conditions and with probes is shown to be essential.

5.1 Introduction

The selective oxidation of organic compounds is as central to synthetic chemistry as to industrial chemical processes.[1,2] Terminal oxidants of choice are O_2 and H_2O_2, primarily due to the minimal chemical impact they and their by-products have on the environment and above all there atom and economic efficiency. The direct use of O_2 and H_2O_2, although thermodynamically favourable is kinetically impeded and hence catalysts are central to their application. Over recent decades, intensive efforts have been directed toward the discovery and development of transition metal based catalysts for the activation of H_2O_2, not least for dihydroxylation and/or epoxidation of olefins and oxidation of other functional groups.[3] Among the many first row transition metal catalysts reported to date, manganese complexes bearing ligands based on the ligand 1,4,7-trimethyl-1,4,7-triazacyclononane (tmtacn) such as **1** (Figure 1) have attracted considerable attention both for their solid state and magnetic properties and as models for bioinorganic systems.[4] In the mid-1990s, the catalytic activity of the complex $[Mn_2^{IV,IV}(\mu\text{-}O)_3(tmtacn)_2](PF_6)_2$ (**1**) was discovered in oxidation and bleaching process by Hage et al.[4b] The application of manganese complexes of tacn in a wide range of oxidative functional group transformations in organic solvents was reviewed recently by Saisaha et al.[5] and by Watkinson et al.[6]

Although the solid state and magnetic properties of these complexes have been examined in detail,[4a] the speciation of these complexes in solution and especially in water has received much less attention.[7] Recent mechanistic studies into manganese catalyzed oxidation catalysis in particular speciation analysis in non-aqueous media, have shown the key role of the formation of μ-carboxylato bridged ($[Mn(III,III)_2(\mu\text{-}O)(\mu\text{-}RCO_2)_2(tmtacn)_2]^{2+}$) complexes (e.g., **2**) formation in the case of **1**, which determines activity and selectivity in the oxidation of alkenes.[8] It was proposed based on ESI-MS experiments and ^{18}O-labeling studies that the dinuclear bis(carboxylato) bridged $Mn(III,III)_2(OH)(OOH)$ species is a key intermediate in the formation of epoxide or *cis*-diol products.[8] In chapter 4, the conversion of **1** to $[Mn(III,III)_2(\mu\text{-}O)(\mu\text{-}RCO_2)_2(tmtacn)_2]^{2+}$ was studied in detail using a combination of UV/Vis absorption, electron paramagnetic resonance (EPR), Raman and resonance Raman (rR) spectroscopy. We proposed that the conversion proceeds by an autocatalytic mechanism and that the species that is responsible for the oxidation of the organic substrates also catalyzes H_2O_2 decomposition, and the former process is competitive.[9] The ability of manganese catalysts to activate H_2O_2 to oxidize various azo and phenolic dyes in aqueous carbonate buffers was studied by Eldik and co-workers.[10] The formation of a Mn(II) -HCO_3 complex was proposed on the basis of UV/Vis absorption spectroscopy and electrochemistry. Precipitation of $Mn(II)CO_3$ was observed in the absence of substrates, while addition of the azo and polyphenolic dyes inhibited the precipitation through complexation. The formation of the catalytically inactive species ($Mn(IV)O_2$) upon reaction of Mn(II) with H_2O_2 in $NaHCO_3$(aq) was confirmed by UV/Vis absorption spectroscopy and ESR.[11] Kinetic analysis was interpreted as indicating that peroxycarbonate, a more reactive oxidant than H_2O_2, formed in situ and presented the rate-limiting step in the reaction.[12] Comparison of the catalytic activity of Mn(II) salts with $[Mn(II)(bpy)_2Cl_2]$ and $[Mn(III)Mn(IV)(\mu\text{-}O)_2(bpy)_4](ClO_4)_3 \cdot 2H_2O$ in the bleaching of dyes indicated common reactive intermediates.

In this chapter the focus is on understanding the behavior of complexes such as **1** during catalytic oxidations under conditions relevant to modern industrial bleaching. The activity of the catalytic system (i.e. **1**) in the oxidation of styrene sulfonate, a conjugated olefin with high solubility in aqueous media, is studied, due primarily to its lack of pH chemistry (Figure 1). The pH dependence of the structure of the complex present in water between pH 6 and 9; the rate of oxidation of styrene with **1** and with Mn(II) salts; and the role of sequestrants, such as DTPA, that are used industrially, on the reaction rate and efficiency were studied with UV/Vis absorption and Raman spectroscopy. The study of the reactivity of Mn(II) under the same conditions was carried out to exclude or implicate the species it forms, in the chemistry observed with **1**; i.e. is **1** a catalyst or simply a source of Mn(II). Here, the major part is focused on control experiments with Mn(II) salts and the effect of variation in the amount of carbonate.

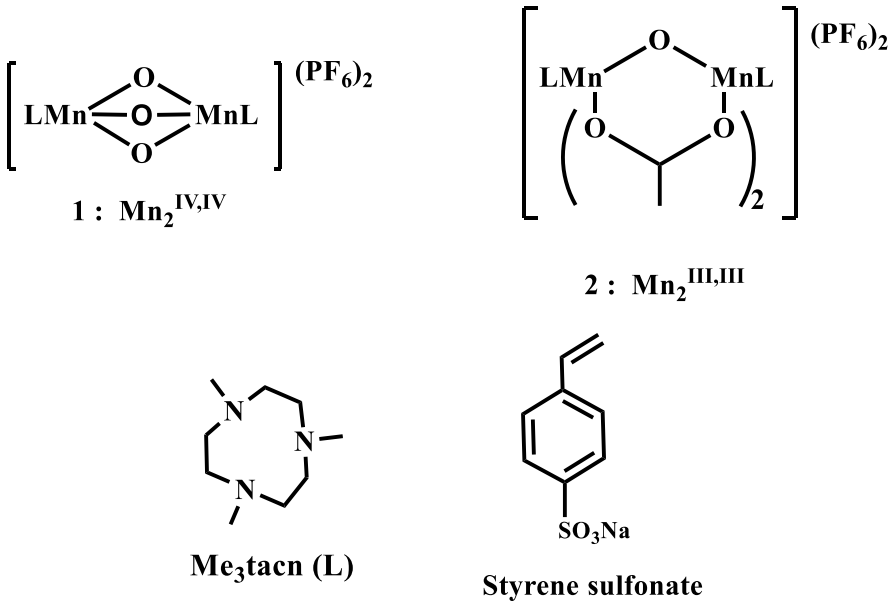

Figure 1 Structure of complexes 1 and 2, the ligand tmtacn and substrates styrene sulfonate (SS)

5.2 Results

Reaction monitoring by UV/Vis absorption, Raman and resonance Raman spectroscopy

Scheme 1 shows typical reaction conditions applied in the present study. The activity of **1** and Mn(II) ions was investigated and compared in the absence and presence of bicarbonate, acetate and borate (common reagents employed in industrial bleaching processes). Raman spectroscopy was used to monitor changes in the concentration of styrene sulfonate and its epoxide product. The bands in the range 1600–1650 cm^{-1} are characteristic of C=C stretching vibrations of vinyl and aryl groups and in particular the band at 1630 cm^{-1} is useful in monitoring reaction progress.[13]

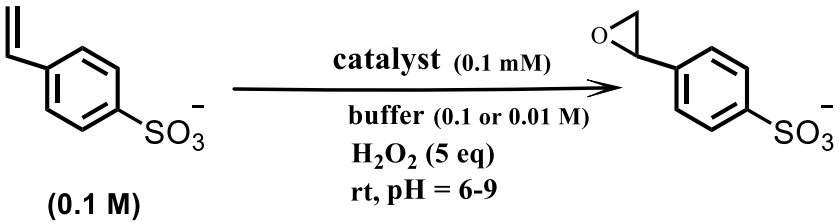

Scheme 1 Catalysed oxidation of styrene sulfonate (SS) with H_2O_2.

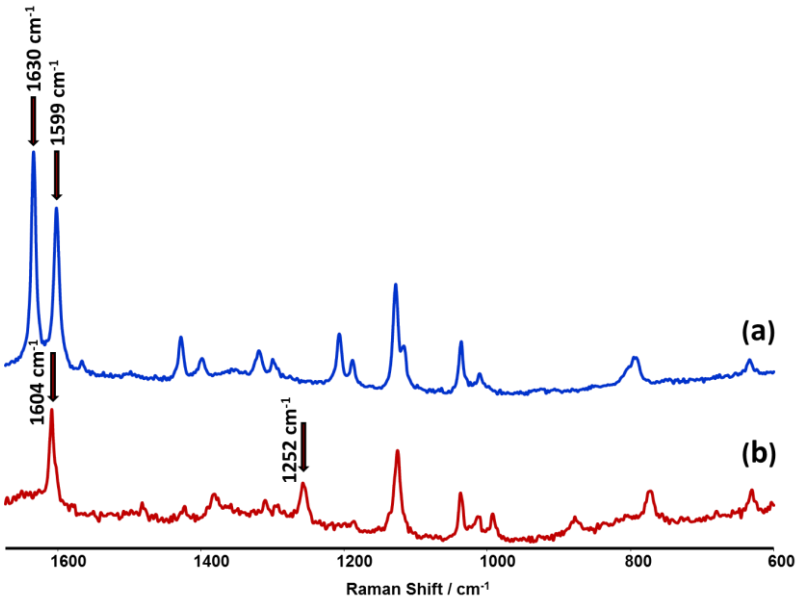

Figure 2 Raman spectra (λ_{exc} 785 nm) of (a) SS and (b) the epoxide product OSS

The UV/Vis absorption spectra of **1**, H_2O_2 and 0.1 M carbonate buffer (w.r.t. water) are shown in Figure 3. Despite the complete absorption of light by H_2O_2 in the UV region, the visible absorption bands of **1** enable monitoring of its concentration and changes to the complex over time, e.g., by monitoring absorbance at 315 nm.

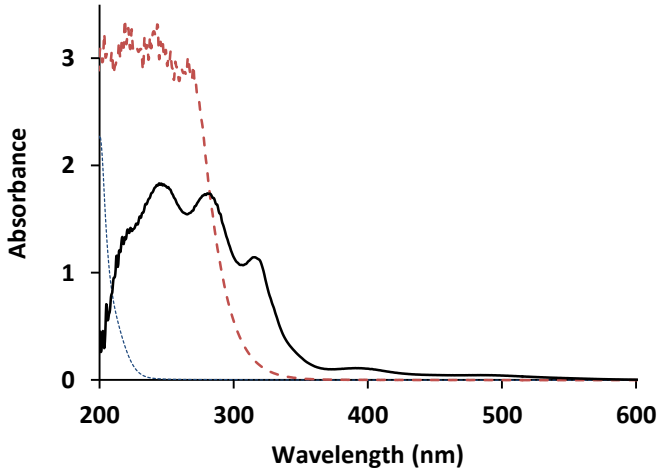

Figure 3 UV/Vis absorption spectra of 1 (0.1 mM, thick line), H_2O_2 (0.5 M, dashed line) and bicarbonate (0.1 M, dotted line) with respect to water as reference.

Stability of 1 in carbonate buffer in the presence of H_2O_2

The effect of the bicarbonate/carbonate on the structure of **1** was monitored by Raman spectroscopy (λ_{exc} 355 nm, Figure 4) over 23 h after the addition of H_2O_2. The spectrum after 23 h shows the complete consumption of the H_2O_2 (876 cm^{-1}) without significant disturbance of the Mn(μ-O_3)Mn core of **1** (699 cm^{-1}).

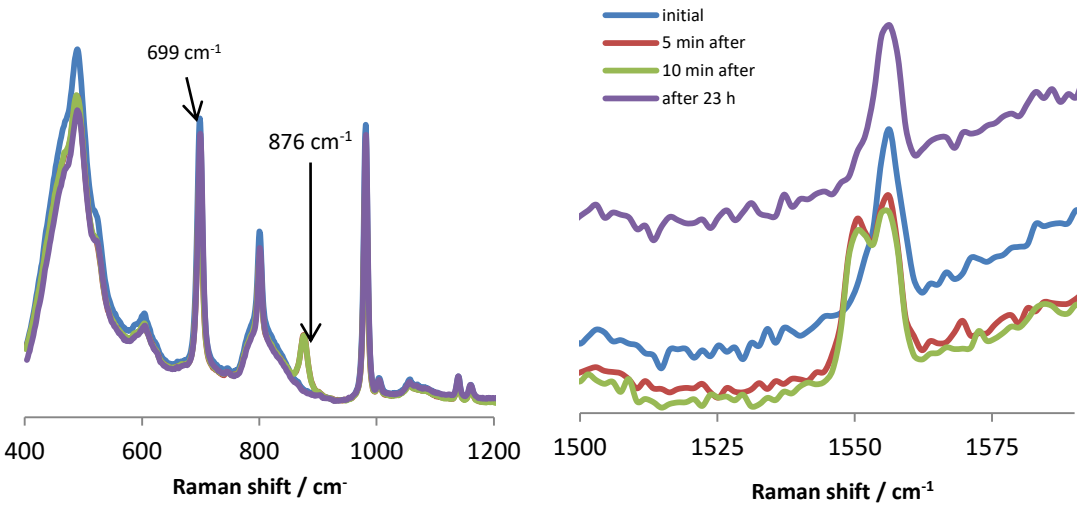

Figure 4 Raman spectra (λ_{exc} 355 nm) of a solution of H_2O_2 (0.5 M), and 1 (3 mM) in $NaHCO_3$ (aq. 0.1 M, pH 8.6) (left) and increase in dissolved O_2 (1550 cm^{-1}) (right). Spectra acquired before (blue), and 5 min (red), 10 min (green) and 23 h (purple) after the addition of H_2O_2.

It is apparent that in $NaHCO_3$(aq), H_2O_2 has no noticeable effect on **1** manifested in the constancy of the Raman band of **1** at 699 cm^{-1} and absorption spectrum[9,14] but that H_2O_2 decomposition proceeds quickly through disproportionation to water and O_2 (1550 cm^{-1}).

Dependence of the rate of oxidation of styrene sulfonate on the concentration of 1 and of Mn(II)SO_4

The rate of epoxidation of styrene sulfonate and the disproportionation of H_2O_2 in $NaHCO_3$(aq) (0.4 M, pH 8.6) was determined with **1** over the concentration range 50 – 200 μM and with Mn(II)SO_4 between 0 – 200 μM (Figure 5). The rate of epoxidation of styrene sulfonate shows a linear dependence on the concentration of **1**, however, the rate of disproportion of H_2O_2, shows no dependence. Notably, however, the duration of the lag period before which H_2O_2 disproportionation commenced was inversely dependent on the concentration of **1**. In contrast to **1**, with Mn(II)(SO_4) both the rate of epoxidation of styrene sulfonate as well as the disproportion of H_2O_2 depend logarithmically on concentration.

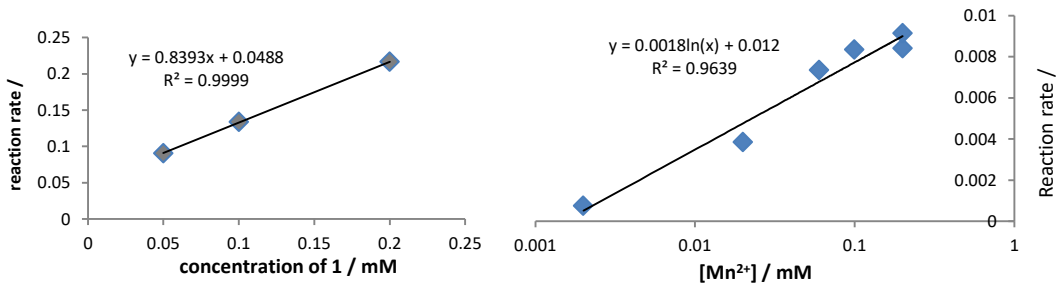

Figure 5 Dependence of the rate of the oxidation of the styrene sulfonate (right) on 1 and (left) on Mn(II)(SO_4).

The logarithmic trend in both the rate of disproportionation and styrene sulfonate oxidation indicates that the actual concentration of 'available' manganese ions in the presence of carbonate is limited both by solubility and by the rate of formation of insoluble manganese oxides – indeed examination of the Pourbaix plot for manganese indicates that Mn(II) is not stable at pH 8.6. Indeed in the absence of styrene sulfonate a dark precipitate formed rapidly upon addition of H_2O_2 to a bicarbonate buffered solution of Mn(II)SO_4. The Raman spectrum of the precipitate (Figure 6) obtained after the reaction of Mn(II) ions with H_2O_2 in the absence or presence of substrate show differences when compared to the spectrum of $MnCO_3$, in particular the bands at ~580 cm^{-1} and ~630 cm^{-1}, which are characteristic of Mn oxides. [15,16]

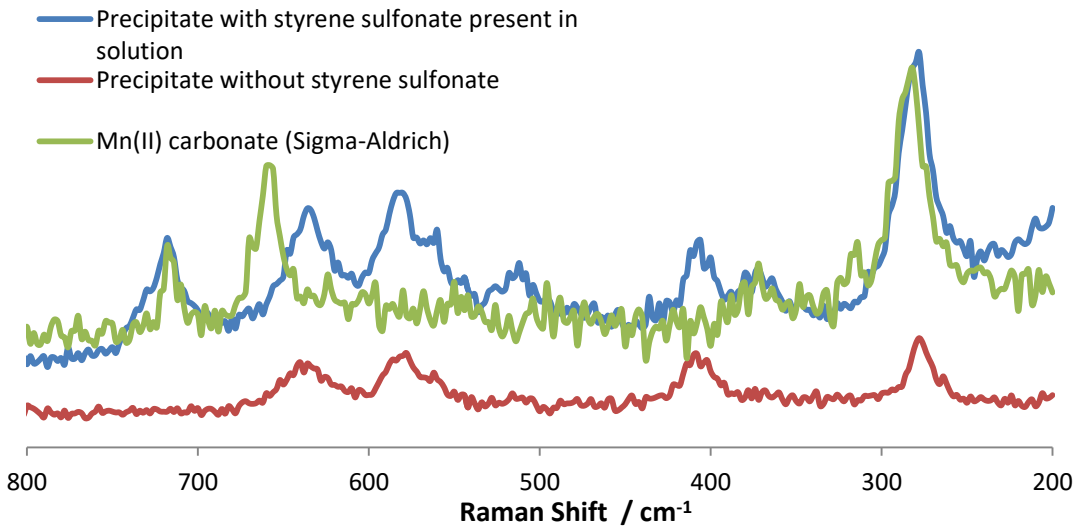

Figure 6 Raman spectrum of $MnCO_3$ (green line) and the spectrum of the precipitate obtained after addition of H_2O_2 to the solution containing $MnSO_4$ (0.2 mM) and $NaHCO_3$ (0.1 M) (red line) and with SS (blue line).

Cooperative effects between 1 and Mn(II)

The oxidation of styrene sulfonate and the disproportionation of H_2O_2 in presence of both **1** and Mn(II) was considered, since **1** could be acting simply as a 'slow leak' source of Mn(II). The reaction was carried out with continuous variation of **1** and Mn(II)SO_4, with a constant concentration of 0.2 mM in manganese. Remarkably the effect of variation on both the rate of H_2O_2 disproportionation and styrene sulfonate oxidation is negligible, which indicates that under these conditions, the same catalytically active species (i.e. not **1** or its derivatives) is responsible primarily.

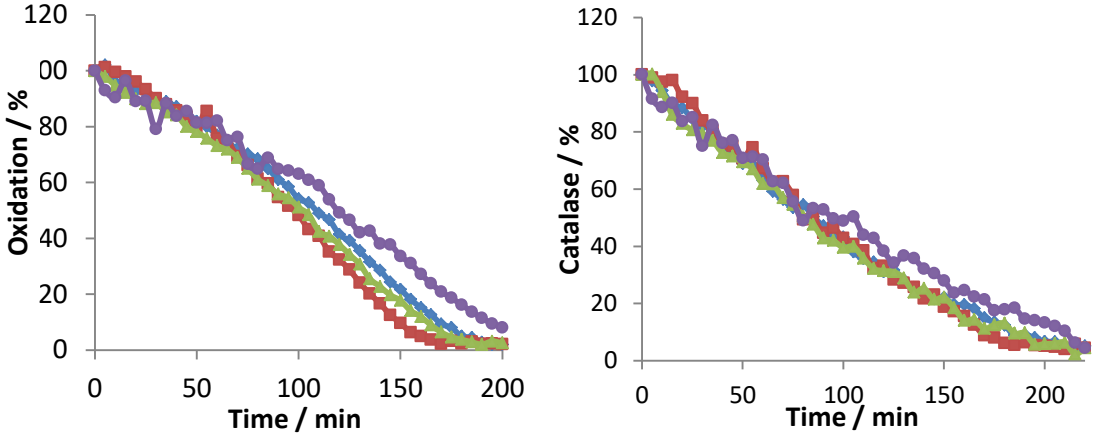

Figure 7 Oxidation of styrene sulfonate with H_2O_2 in the presence of various mole ratios of 1 and Mn(II)(SO_4). Monitor by Raman spectroscopy at λ_{exc} 785 nm. Left: % styrene sulfonate remaining and Right: %H_2O_2 remaining. Reaction conditions: sodium sulfate (0.5 M) as internal reference, H_2O_2 (0.5 M), $NaHCO_3$ (0.1 M), styrene sulfonate (0.1 M), and $MnSO_4$ and 1 in ratios (Mn(II) / (Mn(IV) + Mn(II))): 0 (blue diamonds); 0.5 (red squares); 0.3 (green triangles); 1 (purple circles).

Effect of DTPA on the catalytic oxidation of styrene sulfonate with 1 or Mn(II)SO_4

A frequently used approach to eliminate the effect of adventitious metal ions in aqueous reactions is to add a sequestrant, which by virtue of its multidenticity prevents the metal ion from engaging in catalysis. Hence, the activity of Mn(II)SO_4 is expected to be eliminated upon addition of the sequestrant DTPA (Penta(carboxymethyl)diethylenetriamine). The effect of DTPA on the oxidation of styrene sulfonate with H_2O_2 in the presence of **1** was determined with in situ reaction monitoring by Raman spectroscopy. With Mn(II)SO_4, conversion was not observed in the presence of DTPA, while with **1**, activity was observed albeit with the addition of a lag phase that affected the oxidation of styrene sulfonate more so than H_2O_2. These data indicate that although DTPA inhibits the reaction catalysed by Mn(II)SO_4, it has a lesser effect on the activity of **1**. An experiment that raises a question mark over this conclusion is illustrated Figure 9.

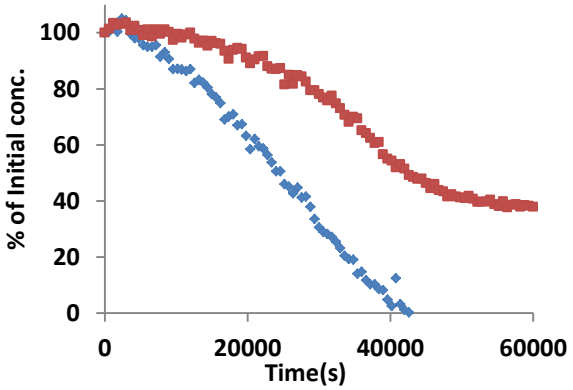

Figure 8 Change in concentration of H_2O_2 (0.5 M) and styrene sulfonate (0.1 M), in $NaHCO_3$ (aq., 0.4 M, pH 8.6), with 1 (0.1 mM), and DTPA (0.1 mM). Conversion was determined from the normalised intensity of Raman bands due to H_2O_2 (876 cm^{-1}, blue diamond's) and styrene sulfonate (1633 cm^{-1}, red squares).

Comparison of the reaction progress without DTPA present with an equivalent reaction in which DTPA is added after 50% conversion (Figure 9), shows that, even with **1**, DTPA does in fact stop conversion. Notably, however, after a considerable period of time, conversion continues again

with a rate similar to that observed without DTPA. These data indicated that a sudden change occurred in the reaction conditions.

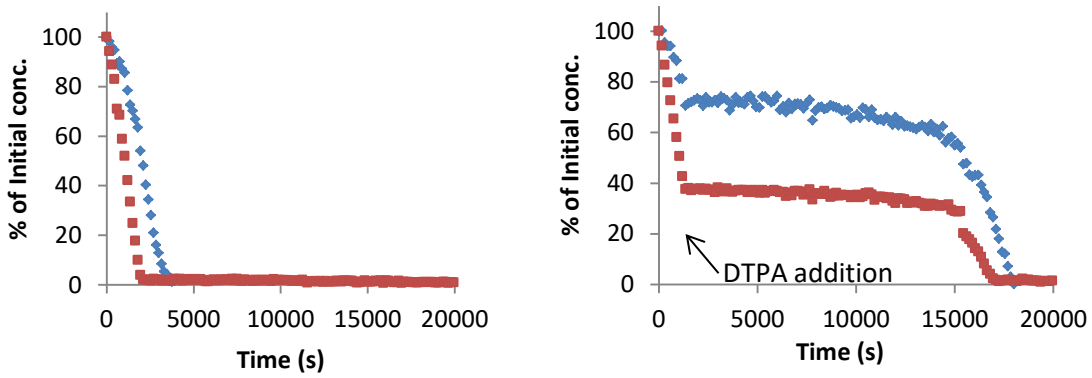

Figure 9 Oxidation of styrene sulfonate (0.1 M) with H_2O_2 (0.5 M) catalysed by 1, and Na_2SO_4 (0.5 M) at pH 8.6 (0.2 M $NaHCO_3$). Styrene sulfonate (1633 cm^{-1}, red squares) and H_2O_2 (876 cm^{-1}, blue diamonds) were monitored by Raman spectroscopy. (left) Without DTPA, and (right) with DTPA (0.1 mM) added after 1350 s.

Addition of H_2O_2 to a solution of **1** in 0.1 M $NaHCO_3$(aq) has no effect on the latter's absorption spectrum between pH 6 and 9 even over several hours in the absence of substrate. Furthermore, there is no evidence for significant decomposition of H_2O_2 over this period. The UV/Vis absorption spectrum of the reaction mixture (i.e. the absorbance of **1**) does not change significantly over the entire course of the reaction under standard conditions also (Figure 10). Reaction of **1** with H_2O_2 in the presence of 1 eq. of DTPA, however, shows a pH dependent lag phase after which a large change in the UV/Vis absorption spectrum is observed indicative of conversion of **1** to another species (Figure 10). A reasonable interpretation of the data is that an autocatalytic reaction leading to decomposition of the DTPA occurs rapidly at the end of the lag period, which 'unlocks' the reaction to Mn(II) salts formed by reduction of **1**.

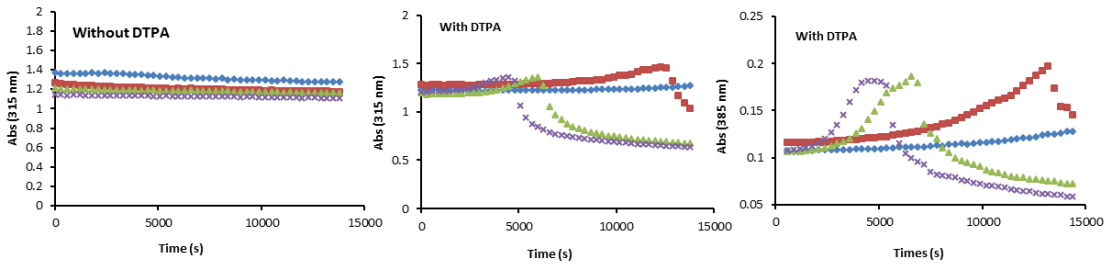

Figure 10 pH dependence of the change in absorbance of the reaction mixture (without styrene sulfonate) at 315 nm with 0.5 M H_2O_2, 0.1 M bicarbonate, 0.1 mM 1 (left) and with 0.1 mM DTPA also (centre and right). pH 8.9 (purple crosses), 8.0 (green triangles), 7.2 (red squares), 6.1 (blue diamonds).

Effect of buffering agents on the reaction rate

The rate of epoxidation of styrene sulfonate in the presence of borate, acetate, water and bicarbonate was determined by reaction monitoring with Raman spectroscopy (λ_{ex} 785 nm). As described above conversion under standard conditions is rapid in 0.1 M $NaHCO_3$(aq), whereas conversion is substantially slower without buffer or with acetate buffer and in borate buffer

conversion is not observed (Figure 11). These data raise the question whether carbonate is essential to the reactivity observed or if the other buffers inhibit the reactivity.

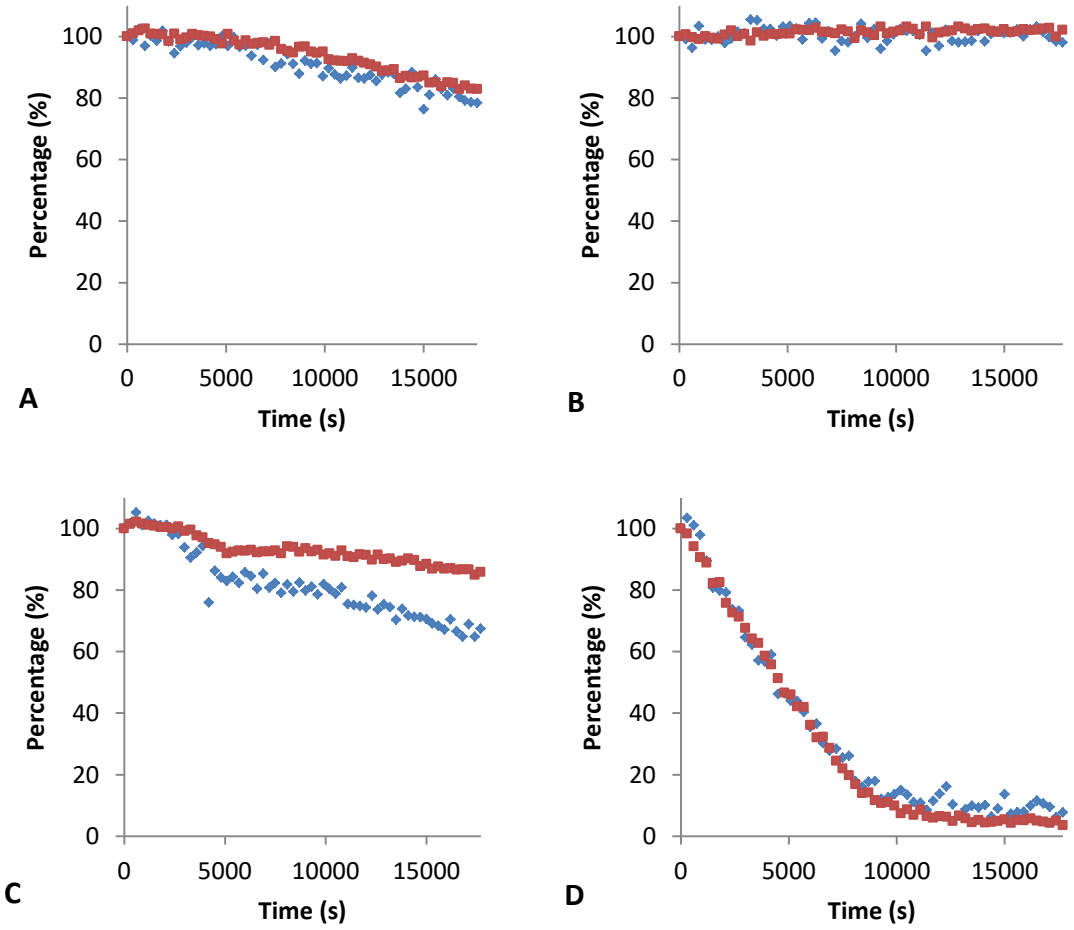

Figure 11 Time dependence of conversion of H_2O_2 (0.5 M blue diamonds) and styrene sulfonate (0.1 M, red squares) with 1 (0.1 mM) and Na_2SO_4 (0.5 M, internal reference) at pH = 8.6 and (a) no buffer, (b) sodium borate (0.1 M), (b) NaOAc (0.1 M), and (b) $NaHCO_3$ (0.1 M).

The effect of acetate and borate in the presence of bicarbonate, on conversion of both styrene sulfonate and H_2O_2 reveals that the presence of acetate has negligible effect in comparison to the reaction with carbonate alone (Figure 12), while the presence of borate increases the lag phase's duration and reduces the reaction rate substantially (Figure 13). Notably, however, a reduction in both the concentration of carbonate and borate results in a substantial decrease in reaction rate. These data indicate that carbonate is not acting simply as a buffer in the reaction but is actively involved, e.g., as a ligand etc.

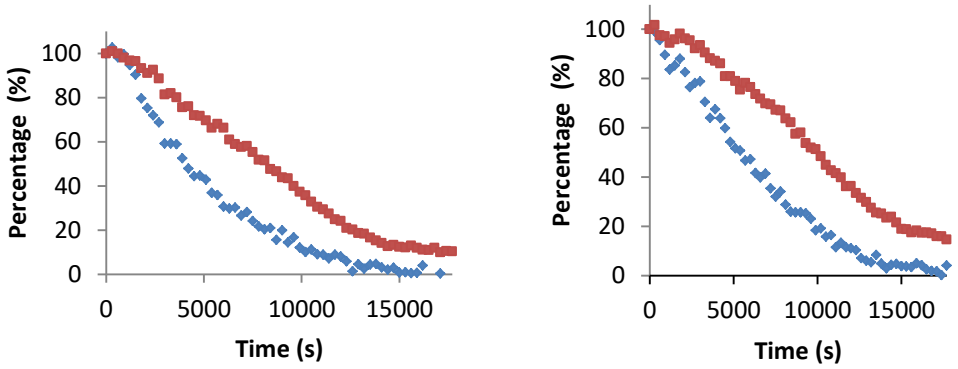

Figure 12 Time dependence of conversion of H_2O_2 (0.5 M blue diamonds) and styrene sulfonate (0.1 M, red squares) with 1 (0.1 mM) and Na_2SO_4 (0.5 M, internal reference) and $NaHCO_3$ (0.1 M, pH = 8.6), without (left) and with (right) NaOAc (0.1 M).

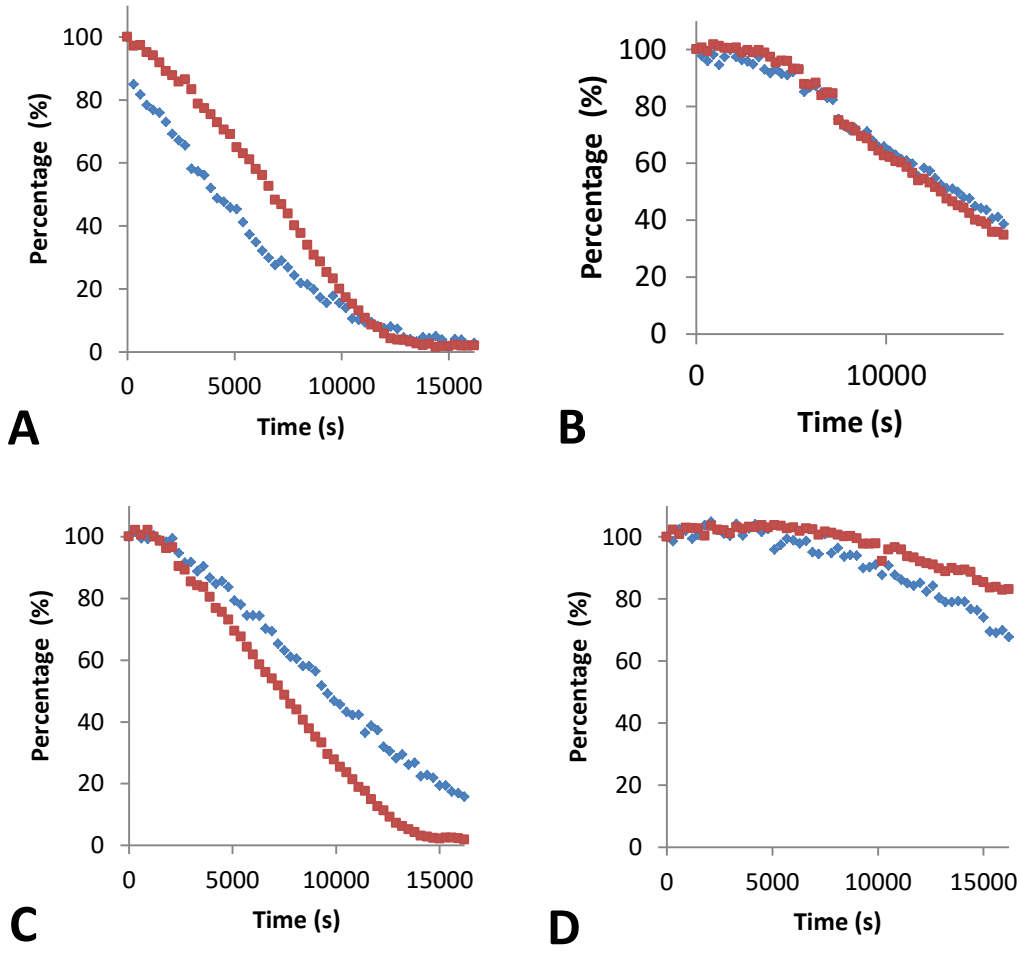

Figure 13 Time dependence of conversion of H_2O_2 (0.5 M blue diamonds) and styrene sulfonate (0.1 M, red squares) with 1 (0.1 mM) and Na_2SO_4 (0.5 M, internal reference) and $NaHCO_3$ (A-C 0.1 M, D 0.05 M, pH = 8.6), without (A) and with sodium borate (B 0.1 M, C &D 0.05 M).

As the borate buffer reveals a lag phase, a jump experiment was performed by adding borate (to 0.1 M) to a 0.1 M $NaHCO_3$(aq) solution after approx. 20% conversion of the substrate (Figure 14a). A control experiment in which 0.1 M $NaHCO_3$(aq) bicarbonate was added had no such effect (Figure 14b). In figure below, a drop in intensity is seen, which is observed as a drop in

concentration; however, this drop is assigned to absorption of the borate at different wavelengths.

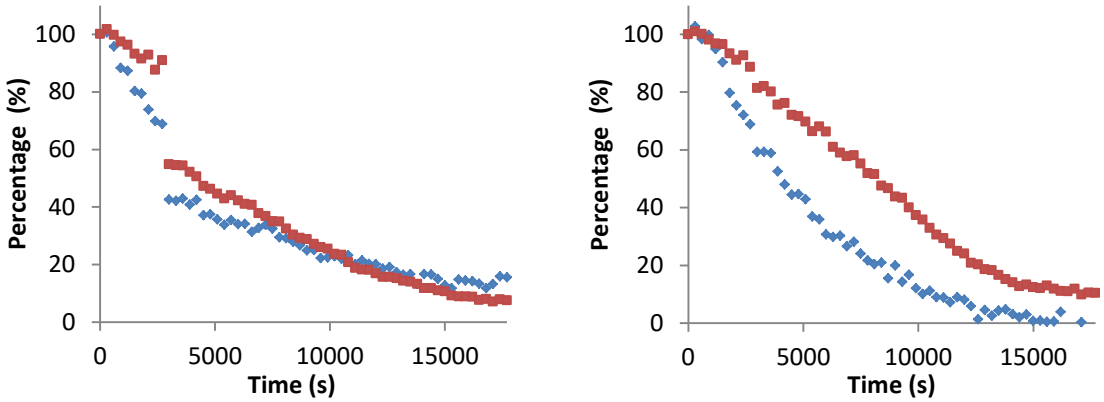

Figure 14 Time dependence of conversion of H_2O_2 (0.5 M blue diamonds) and styrene sulfonate (0.1 M, red squares) with 1 (0.1 mM) and Na_2SO_4 (0.5 M, internal reference) and $NaHCO_3$ (0.1 M), (left) borate (0.1 M) was added after 2700 s and (right) the same volume of buffer containing 0.1 M $NaHCO_3$ was added after 2700 s.

In situ formation of percarbonate.

The formation of percarbonate has been proposed by several groups to rationalise the activity of Mn(II) salts in the epoxidation of alkenes and in the bleaching of model dyes.[17,18,10] A similar reaction could be expected in the case of borate buffer (i.e. the formation of perborate). The presence of such species under catalytic conditions was explored in an effort to understand the role of the buffering agents in catalytic oxidation of styrene sulfonate. The formation of perborate in solution is plausible, however, it is relatively insoluble in basic water and hence the effect of such a reaction would be to inhibit oxidation by removal of oxidant from the solution (vide supra).

It is conceivable that peroxido-compounds form from the reaction of H_2O_2 with CO_2, HCO_3^-, CO_3^{2-}. Raman spectroscopy 532 nm and 785 nm, however, does not provide evidence for the formation of percarbonate in solution. Comparison of the Raman spectra of a solution of commercial sodium percarbonate and of sodium bicarbonate with H_2O_2 (pH 8.5, Figure 15) reveals that the only difference between the solutions is in regard to the bands at 984 and 1070 cm^{-1}, which are due to differences in pH and hence the concentration of CO_3^{2-} and HCO_3^-. However, the band at 984 cm^{-1} does not correspond to any of the bands in the spectra of bicarbonate solution collected at pH between 12 and 7 (Figure 16).

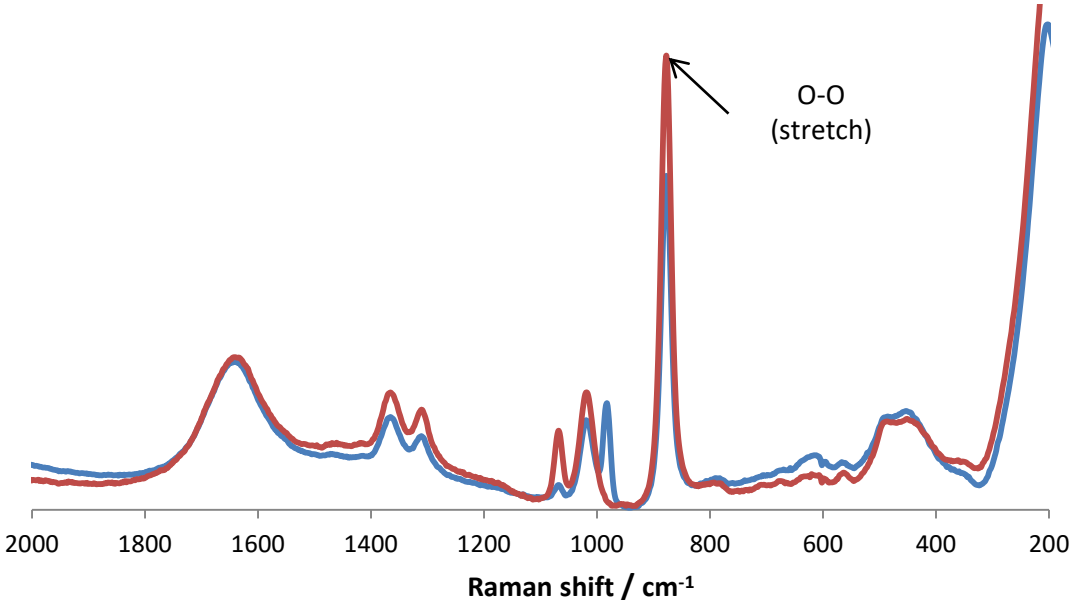

Figure 15 Comparison of Raman (λ_{exc} 532 nm) spectra of a 500 mM solution (pH 8.3) of sodium percarbonate (blue line) and of a solution of sodium bicarbonate (500 mM) and H_2O_2 (600 mM) (pH 8.7, red line).

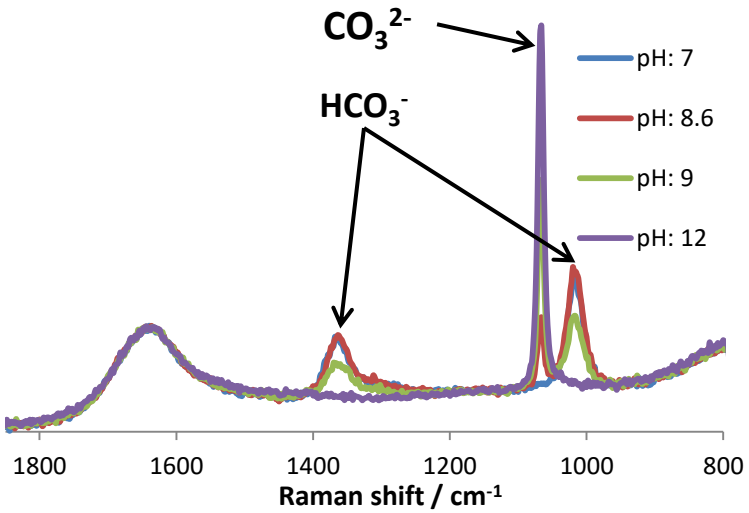

Figure 16 pH dependence of Raman (λ_{exc} 785 nm) spectrum of a $NaHCO_3$ (0.5 M) aqueous solution.

Catalytic activity of 1 under industrially relevant conditions:

Reaction progress monitoring of oxidation of the styrene sulfonate (SS) with H_2O_2 and **1** or Mn(II) was studied between pH 6 – 9 with a concentration of bicarbonate that is much less (10 mM) compared to studies described above and of more relevance to industrial conditions. In presence of Mn(II), conversion of styrene sulfonate was not observed over the pH range examined.

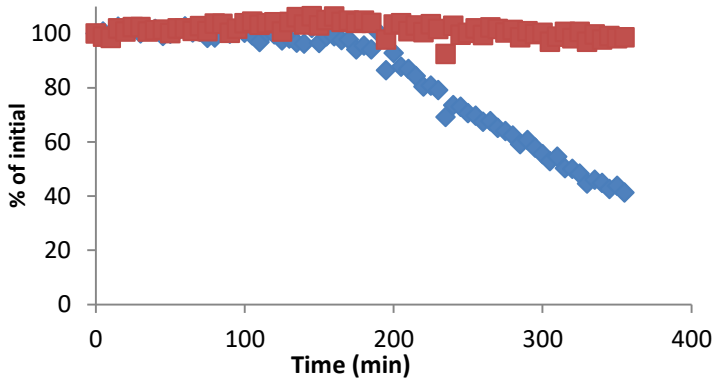

Figure 17 Time dependence of conversion of H_2O_2 (0.5 M blue diamonds) and styrene sulfonate (0.1 M, red squares) with Mn(II)SO_4 (0.2 mM) and Na_2SO_4 (0.5 M, internal reference) and $NaHCO_3$ (0.01 M, pH 8).

In contrast to **1**, although the reaction proceeds more slowly, conversion is observed. At pH 9 the lag phase decreases. Notably, although the rate of oxidation of styrene sulfonate shows little, if any, pH dependence, the rate of disproportionation of H_2O_2 increases with pH. (Figure 18)

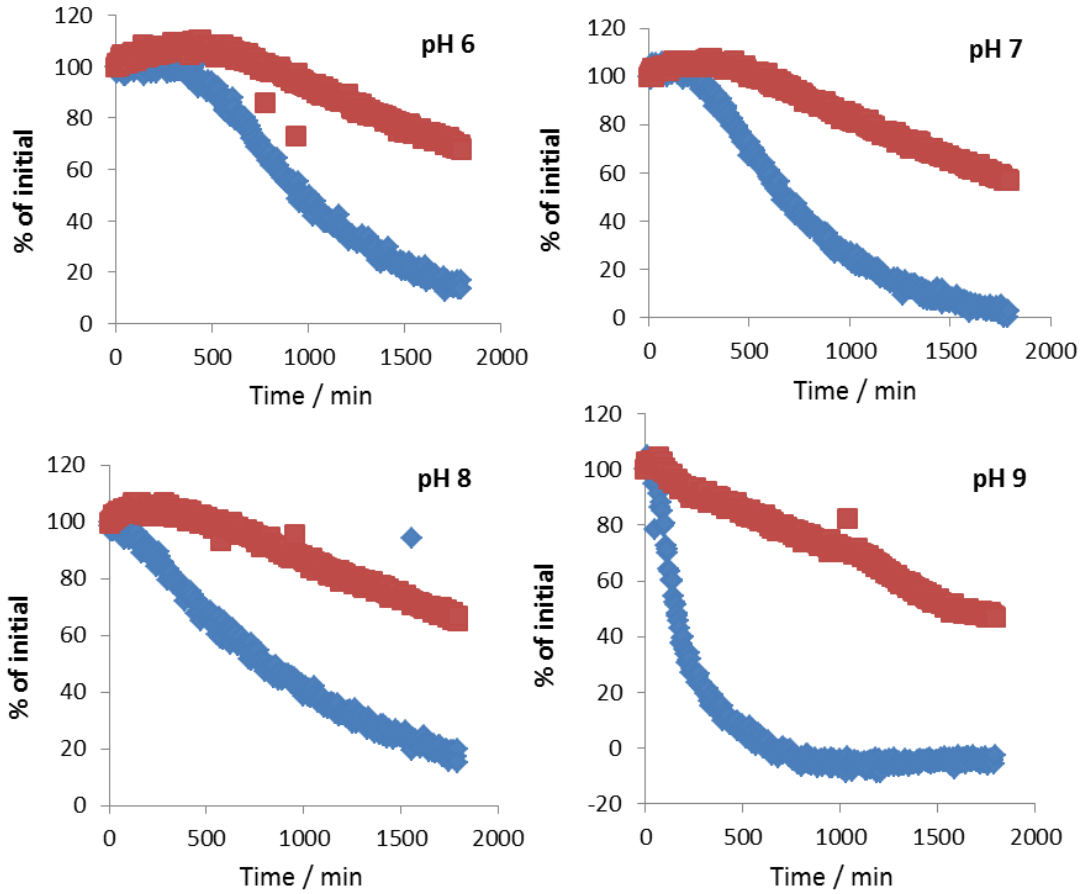

Figure 18 Time dependence of conversion of H_2O_2 (0.5 M blue diamonds) and styrene sulfonate (0.1 M, red squares) with 1 (0.1 mM) and Na_2SO_4 (0.5 M, internal reference) and $NaHCO_3$ (0.01 M). Upper left – pH 6, Upper right - pH 7; Lower left - pH 8; Lower right - pH 9.

5.3 Discussion

A key observation as to the physical changes that occur during the reactions is that the appearance of a brown precipitate is noticeably faster with Mn(II)SO_4 in the absence of substrate. This indicates that the formation of manganese oxides, which is thermodynamically favored at the pH of the solutions, is a slow process requiring nucleation. The dependence of the reaction rate on $\log_{10}$[Mn(II)] is consistent with the metastable situation that is encountered in the reaction; i.e. the manganese present should be in the form of manganese oxides but the formation of these is retarded by the presence of the substrate and accelerated due to the autocatalytic nature of their formation. Given that higher oxidation states are required to form the manganese oxides, the substrate can suppress nucleation by keeping the concentration of these species low. It is not inconceivable that the concentration of carbonate has a substantial influence on these processes given the low solubility of Mn(II)CO_3 (K_{sp} 2.24 x 10^{-11}). Hence, the actual steady state concentration of Mn(II) under reaction conditions is likely to be much lower than the analytical concentration. The effect of carbonate, although it is attractive to ascribe it to the formation of percarbonates, is therefore most likely due to its control on the steady state concentration of Mn(II). At lower concentrations of carbonate, its ability to inhibit the formation of manganese oxides is reduced non-linearly. Hence, the availability of catalytically active Mn(II) ions is drastically reduced and the disproportionation of H_2O_2 by the oxides at high pH is observed.

If it is presumed that Mn(II) ions are responsible for the catalysis observed and accepted that they are only present at low concentrations, then it is possible that the primary involvement of **1** in the reaction is to provide for a slow 'leach' of Mn(II) ions into solution.

A further argument in favor of the active catalytic species at high carbonate concentrations as being Mn(II) ions is provided by the effect of DTPA. DTPA sequesters metal ions effectively and suppresses the activity of Mn(II)SO_4 completely. In the case of **1**, DTPA does not halt conversion indefinitely, however reaction monitoring by UV/Vis absorption spectroscopy indicates that after a lag time the DTPA (which contains oxidizable amines) undergoes oxidative degradation, thereby releasing and Mn(II) ions captured.

At lower concentrations, where the activity of Mn(II) ions is negligible, then the conversion of substrate can be attributed to species derived from **1**. The lower reaction rates observed indicate that it may well show the same activity at higher carbonate concentrations but this would be masked by the activity of the Mn(II) ion based catalyst.

5.4 Conclusions

The reactivity of Mn(II) and **1** towards the oxidation of alkenes in aqueous solution is similar but not identical. Mn(II) presents a greater dependence on its own concentration and that of bicarbonate as well, whereas **1** shows a linear dependence of concentration on activity and depends less strongly on the presence of bicarbonate. It is remarkable that, in contrast oxidation in acetonitrile, in water **1** is unaffected by the presence of H_2O_2 (in absence of substrate at least). The difference in the requirement for carbonate/bicarbonate in solution points towards the possible formation of percarbonate species in the case of Mn(II) catalysed reactions, however, definitive evidence for its formation is elusive. The presence of borate, inhibits catalysis and

implies the in situ formation of the oxidant sodium perborate, however, while this species has not been observed it is clear that borate removes H_2O_2 by precipitation.

The most striking, and in many ways problematic, experiment is that with DTPA, which highlights how the presence of the sequestrant can prevent oxidation with Mn(II) but does not appear to affect the activity of **1** substantially. However, it is clear from the time dependent spectroscopy that in fact DTPA undergoes oxidation and therefore releases the bound ions into solution. These data raise the question whether or not **1** is acting as a Mn(II) reservoir and provides for a jumping off point for further studies of this complex system.

5.5 Experimental

Materials

Styrene sulfonate (Sigma Aldrich) and H_2O_2 50 % aqueous solution (Acros) and all the other commercially available chemicals were used without further purification unless stated otherwise. $[Mn(IV,IV)_2(\mu\text{-}O)_3(tmtacn)_2](PF_6)_2$ (**1**) was available from earlier studies.[9]

Instrumentation

Raman spectra were recorded using a Perkin-Elmer Raman Flex equipped with a fibre-optic probe (λ_{exc} 785 nm) at room temperature, typically with 10 exposures of 8 s duration. Raman spectra (λ_{exc} 355 nm) were recorded as described in chapter 4. UV/vis absorption spectra were recorded with a HP8453 spectrophotometer or a Specord600 (AnalytikJena) in 1 cm path length quartz cuvettes.

Catalysed oxidations

Oxidation of styrene sulfonate was carried out in a cuvette (3 mL total volume) according to the following protocol: Double distilled water was used to prepare a stock solution of 0.5 M Na_2SO_4, from which a buffer solution (typically 0.1 M) was prepared. A stock solution containing the **1** or $MnSO_4$ (3 and 6 mM, respectively) was prepared in parallel. The reaction mixture was prepared directly in the cuvette by addition of the appropriate volumes of buffer, the catalyst and, at the start of the experiment, aq. H_2O_2 with vigorous mixing. Typical concentrations employed were 0.1 M substrate, 0.1 mM catalyst and 0.5 M H_2O_2. Time zero is taken to be the point at which the catalyst is added. The epoxide, product of SS, was isolated and characterized by ^1H NMR spectroscopy as described elsewhere.[13]

Analysis of Raman spectra

Raman spectra were analysed in the spectral range 1800 to 600 cm^{-1}. The data analysis used the area of the bands between 1600 and 1650 cm^{-1}, which includes contributions from the reactant and products only. The band at 870 cm^{-1} was used to determine H_2O_2 concentrations. **1** and **2** were monitored at λ_{exc} 355 nm in the range 400 to 1000 cm^{-1}.

5.6 References

[1] a) J. A. Malona, K. Cariou, W. T. Spencer III, A. J. Frontier, *J. Org. Chem.*, **2012**, *77*, 1891. **b)** M. Marigo, J. Franzén, T. B. Poulsen, W. Zhuang, K. A. Jørgensen, *J. Am. Chem. Soc*. **2005**, *127*, 6964.

[2] a) S. S. Stahl, P. L. Alsters, "Liquid Phase Aerobic Oxidation Catalysis Industrial Applications and Academic Perspectives", Whiley-VCH, Weinheim, Germany, **2016**. **b)** J. R. Lokemeyer, M. Matusz, R. C. Yeates, "Epoxidation Catalyst, a Process for Preparing the Catalyst, and a Process for the Production of an Olefin Oxide", **2015**. **c)** R. Postma, P. Muppa, "Process for the manufacture of a 1,2-epoxide", **2014**.

[3] a) J.-E. Bäckvall, **"**Modern oxidation methods**",** Whiley-VCH, Weinheim, Germany, **2010**. b) J. Ichihara, A. Kambara, K. Iteya, E. Sugimoto, T. Shinkawa, A. Takaoka, S. Yamaguchi, Y. Sasaki, *Green Chemistry*, **2003**, *5*, 491. c) T. Katsuki, *Chem. Soc. Rev*., **2004**, *33*, 437.

[4] a) K. Wieghardt, U. Bossek, B. Nuber, J. Weiss, J. Bonvoisin, M. Corbella, S. E. Vitols, J. J. Girerd, *J. Am. Chem. Soc*., **1988**, *110*, 7398. b) V. C. Quee-Smith, L. DelPizzo, S. H. Jureller, R. Hage, J. L. Kerschner, *Inorg. Chem*. **1996**, *35*, 6461.

[5] P. Saisaha, J. W. de Boer, W. R. Browne, *Chem. Soc. Rev*., **2013**, 42, 2059.

[6] K. F. Sibbons, K. Shastria, M. Watkinson, *Dalton Trans*., **2006**, 5, 645.

[7] a) J. W. de Boer, W. R. Browne, J. Brinksma, P. L. Alsters, R. Hage, B. L. Feringa, *Inorg. Chem*. **2007**, 6353. b) S. Abdolahzadeh, J. W. de Boer, W. R. Browne, *Eur. J. Inorg. Chem*. **2015**, 3432.

[8] J. W. de Boer, W. R. Browne, J. Brinksma, P. L. Alsters, R. Hage, B. L. Feringa, *Inorg. Chem*., **2007**, 46, 6353–6372

[9] D. Angelone, S. Abdolahzadeh, J. W. de Boer, W. R. Browne, *Eur. J. Inorg. Chem.*, **2015**, 21, 3532.

[10] E. Ember, S. Rothbart, R. Puchta, R. van Eldik, *New J. Chem*., **2009**, 33, 34.

[11] E. Ember, H. A. Gazzaz, S. Rothbart, R. Puchta, R. van Eldik, *Applied Catalysis B: Environmental*, **2010**, 95, 179.

[12] E. V. Bakhmutova-Albert, H. Yao, D. E. Denevan, D. E. Richardson, *Inorg. Chem*., **2010**, 49, 11287.

[13] S. Abdolahzadeh, N. M. Boyle, A. Draksharapu, A. C. Dennis, R. Hage, J. W. de Boer, W. R. Browne *Analyst*, **2013**,138, 3163.

[14] R. Hage, B. Krijnen, J. B. Warnaar, F. Hartl, D. J. Stufkens, T. L. Snoeck, *Inorg. Chem.*, **1995**, 34, 4973.

[15] S.-H. Shim, D. LaBounty, T. S. Duffy, *Phys. Chem. Minerals*, **2011**, 38, 685.

[16] C. Julien, M. Massot, S. Rangan, M. Lemal, D. Guyomard, *J. Raman Spectrosc*. **2002**, *33*, 223.

[17] B. S. Lane, M. Vogt, V. J. DeRose, K. Burgess, *J. Am. Chem. Soc.*, **2002**, 124, 40, 11946.

[18] D. E. Richardson, H. Yao, K. M. Frank, D. A. Bennett, *J. Am. Chem. Soc*. **2000**, 122, 1729.

Chapter 6

Reaction Monitoring of Two-Phase Reactions by Raman Spectroscopy through Rapid Spectral Acquisition and Automated Spectral Sorting

Biphasic reactions offer tremendous opportunities in industrial chemical syntheses due to the ease at which the phases and hence reagents can be separated, thereby avoiding energy intensive separation processes such as distillations. A contemporary challenge presented in the implementation of biphasic reaction conditions is to determine and control the chemistry occurring in each phase, in order to improve manufacturing processes. On-line HPLC techniques for monitoring biphasic reaction monitoring have already been developed and demonstrate the potential benefits of on-line monitoring in controlling and optimizing reactions. In this chapter, a fully automated system for monitoring changes in the composition of two immiscible phases by Raman spectroscopy using a flow sampling system is described. This Raman spectroscopy/Flow system can acquire and distinguish Raman spectra of the phases present in an emulsified reaction mixture and offers a key advantage in the real-time information it can deliver. The final goal is to obtain reliable real-time kinetic data on two phase reaction mixtures in which substrates in the organic phase undergo oxidation.

6.1 Introduction

The scale at which fine and bulk chemical syntheses are carried out industrially makes them a primary target for achieving sustainability through reduction in the energy and resource demands. In parallel with the development of new, catalytic, synthetic methodologies, it is essential also to consider the physical methods used to carry out reactions and subsequent separations and purifications.[1] Continuous flow and biphasic batch/flow reactions play a central role in achieving these goals.[2] Both approaches offer opportunities in increasing the selectivity and overall efficiency of reactions with physical phase separation after the reaction (i.e. separation of immiscible solvent streams) reducing energy and materials costs. Furthermore, the use of water in reactions offers an important advantage in terms of safety due to its relatively high heat capacity. These approaches are used extensively in industry[3] and increasingly at research and development stages also.[4]

The development of new processes that make use of two phase conditions require real time (ideally in- or on-line) analysis in the quantification and control of the chemistry occurring in each phase. Inline HPLC, UV/vis absorption and FTIR and FTNIR[5] absorption spectroscopies have been applied to monitoring biphasic reactions and the potential benefits of inline monitoring in controlling and optimizing reactions are apparent.[6, 7] Two phase reactions present unique analytical challenges (vide infra) due to the physical properties of the reaction media. Sampling for at- or off-line analysis is an alternative provided that it is safe to do so and that both rapid phase separation and analyses can be achieved. However, the lag time between physical sampling and analysis, e.g., by HPLC or GC, precludes real-time control and retards process optimization. A further limitation is that accurate quantification of all components in all phases is costly in time and resources despite being essential in developing the microkinetic models that enable prediction of reaction progress.

The challenges faced in spectroscopic analysis of biphasic reactions spectroscopically are manifold.[8] Scattering, both due to a mismatch in refractive indices of the two phases in the case of emulsions and due to particulates, is the most challenging and although ATR-FTIR,[9] and ball-probe Raman spectroscopy[10] can circumvent the effect of scattering by particles, decreased time resolution and probe fouling limit their effectiveness. Furthermore, only a weighted average spectrum of the phases is obtained which prevents, for example, determination of the partitioning of organics into an aqueous phase and order of magnitude differences in spectral intensities between organic and aqueous components mean that often essentially only one phase is ‘seen’ (Figure 1). Overcoming these limitations necessitates addressing each phase individually and rapid real-time phase separation and spectral acquisition. In this regard Raman spectroscopy offers advantages due to the relatively low Raman scattering cross-section of water and the sharpness of bands compared with those observed in FTIR and UV/Vis absorption spectroscopy. Furthermore, Raman spectroscopy does not require a reference measurement, which simplifies implementation tremendously.

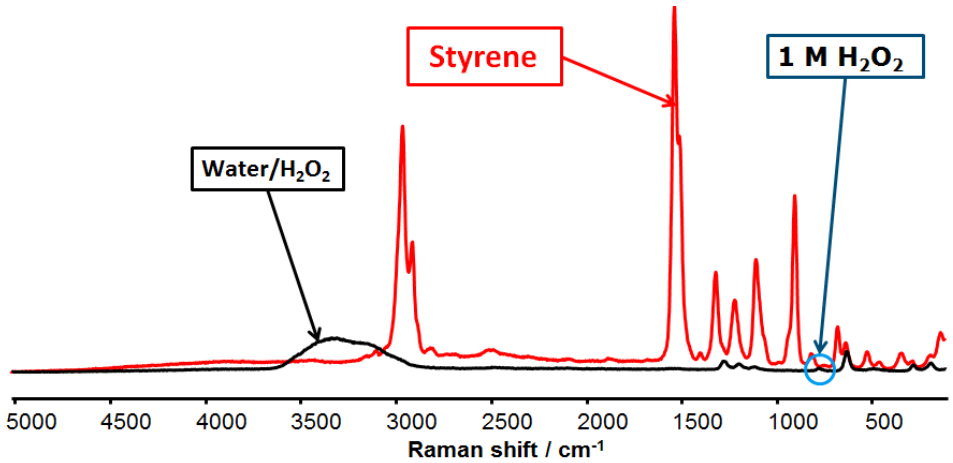

Figure 1 Comparison of the Raman spectrum of 1 M H_2O_2 in water and neat styrene obtained under identical sampling conditions at λ_{exc} 785 nm in a Teflon tube (vide infra). The relative signal intensity of the H_2O_2 contained in the aqueous phase is orders of magnitude less than that of the organic phase.

In this chapter an approach to in/on-line monitoring of two phase reactions is presented, which overcomes these challenges and demonstrate the use of the method in the manganese catalyzed epoxidation of styrene with H_2O_2.[11] The approach taken is described in Scheme 1 and can be broken down into two components. Spectral acquisition is achieved by placing a Teflon tube within the confocal volume of the Raman probe and using rapid (600 s^{-1}) spectral acquisition to obtain spectra containing contributions from only one of either of the phases. In the case of continuous flow systems this approach makes use of the propensity for immiscible solvents (i.e. two phase mixtures) to exhibit plug or slug flow.[12] In batch reactors direct monitoring of the individual phases in real-time is not possible but rapid sampling using a peristaltic pump, which, under appropriate conditions, breaks the emulsion to yield a slug flow behavior in PTFE/FEP tubing system. This approach allows for individual spectra to be obtained but presents a challenge with regard to data analysis. This challenge is meet through the use of a real-time spectral sorting algorithm to identify pure spectra of each phase and discard spectra containing contributions from both phases. Overall the approach allows for real time monitoring of both phases and overcomes the challenges presented by large differences in the Raman scattering cross-section of each phase (Figure 1).

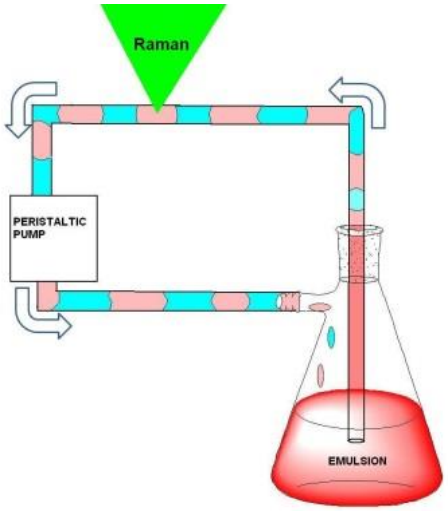

Scheme 1 Raman sampling system for two phase reactions. The different colors in the tube represent segmented slug flow. The green triangle represents how the laser light coming from the Raman probe focuses inside the tube volume.

6.2 Experimental section

Chemicals and reagents

$[Mn_2(\mu\text{-}O)_3(tmtacn)_2](PF_6)_2$ (**1**) (Catexel BV), and H_2O_2 (Acros 50 % w/w), Styrene (Sigma-Aldrich, with stabilizer), Styrene oxide (Sigma-Aldrich).

Model reaction

The experimental arrangement for the studies conducted required a biphasic reaction mixture. The organic phase of the reaction consisted exclusively of styrene (99% Sigma Aldrich, 50 ppm of t-butyl-catechol as stabilizer); the other phase consisted in a 0.2 M aqueous solution of sodium bicarbonate (puriss. Sigma Aldrich) containing **1** (typically 3 mM) and H_2O_2 (2 eq. w.r.t. styrene) added over 5 h. The model biphasic reaction used as a study case for developing the technique is the epoxidation of the styrene (Figure 2). The reaction was carried out by mixing the organic phase, styrene, with an aqueous solution containing 0.2 M $NaHCO_3$ and 3 mM of **1** (Figure 2). The mixture obtained is biphasic, however, vigorous mixing achieved what approximates an emulsion, which is essential for rapid establishment of interphasial equilibria. H_2O_2 (50% w/w) was added by syringe pump continuously over the reaction period to a final amount of 2 eq. w.r.t substrate.

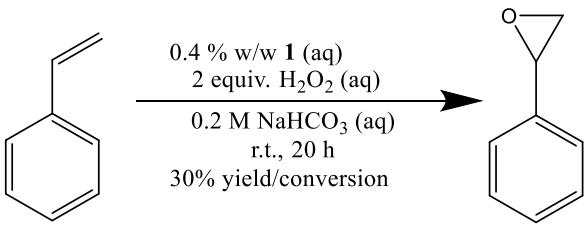

Figure 2 Epoxidation of styrene to yield styrene oxide, used as a case study, is achieved by vigorous stirring with 0.2 M $NaHCO_3$ (aq) containing 1 (3 mM) and H_2O_2 (2 equiv. w.r.t. styrene added over 5 h).

The reaction proceeded to 30% conversion and yield of epoxide, as determined from the ^{1}H NMR spectrum of the organic phase (Figure 3). Minor amounts of a product of further oxidation, in particular benzaldehyde, were observed also. The most important side products present in the aqueous and the organic phases are benzaldehyde and 1-phenyl-1,2-ethanediol, which were present, at most, at 2%.

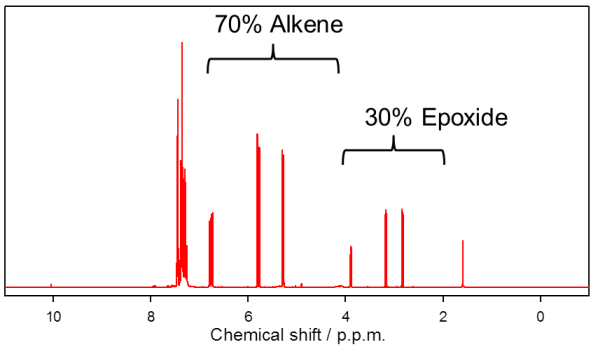

Figure 3 ^{1}H-NMR spectrum of the organic phase obtained after 20 h, showing signals of styrene and styrene epoxide as well as traces of aldehyde.

The method developed for obtaining spectra of the individual phases in the reactor consists of circulating, via a peristaltic pump, the emulsion formed by the two phases through a PTFE/FEP tubing system. The peristaltic pump (WPI, MiniStar™, Mounted with a Gore Style 100CR tube, ID: 2.8 mm) provided a gentle pulsed flow to the mixture through the FEP tubing system (Idex I.D.: 1/8”). The materials tested for the tubing system included silicon for the peristaltic part of the tubing, and PTFE and PVC for the rest of the circuit, however, FEP provided the best compromise between transparency and chemical inertness in comparison with PTFE and PVC. The diameter of the tube is a critical factor in acquiring good quality spectra with short acquisition times, with two commercially available diameters tested (1/16” and 1/8”). Upon entering the tube the emulsion is broken and a two phase (organic and aqueous) flow (slug flow, ~10 mL/s) is obtained. The slug flow pass through the confocal volume of the Raman system, with spectral acquisition every 60 ms. The sample withdrawn by the pumping system must be returned to the reaction vessel with a minimum delay and hence the flow rate and time available to record a spectrum of individual slugs is limited. Raman spectra were obtained using a 300 mW or 25 mW 532 nm fiber coupled laser (Cobolt Samba) connected to a low cost Raman probe (Inphotonics) and via a circle to line bundle to a Shamrock163 spectrograph with a Newton EMCCD CCD camera (Andor Technology). The choice of 532 nm as excitation wavelength is to access the maximum sensitivity of the CCD array for collection of Raman scattering. A script written in the Andor Basic language for controlling the acquisition system of the camera (1000 spectra per minute) and a program written in the C language was used to recognize, sort and average the spectra representing the individual phases and exclude mixed spectra.

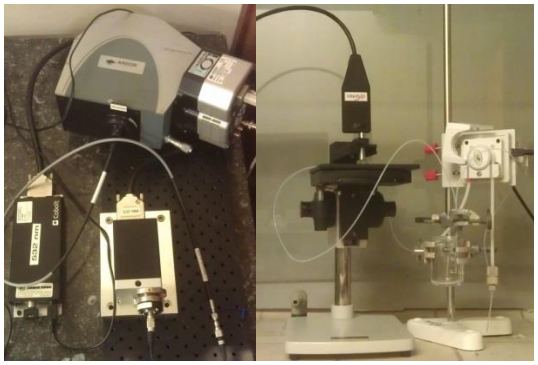

Figure 4 Raman spectrometer and arrangement for inline measuring.

6.3 Results and discussion

The reaction chosen in the current study is the epoxidation of styrene in aqueous H_2O_2. This reaction was selected as it requires the activation of H_2O_2 by a catalyst (**1**) for conversion of substrate and H_2O_2 to occur. Hence, in the absence of **1**, mixtures of styrene, styrene oxide and styrene-1,2-diol are stable in the presence of 1 M H_2O_2 in water over long periods.

Two phase mixtures of immiscible solvents typically show slug rather than side-by-side flow in micro and mesofluidic channels,[13] which facilitates acquisition of spectra of each phase (vide infra). In the case of batch reactions, ideally an emulsion is formed to maximize interfacial area and hence maximizes mass transfer rates between the two phases. Typically, however, the refractive indices of the two phases are different and hence light scattering is extensive, which presents two limitations with regard to in-line analysis by spectroscopic techniques, and especially when using Raman spectroscopy. The excitation light reaching the confocal volume is attenuated heavily which, together with scattering of the Raman photons produced, drastically diminishes overall signal intensity and therefore sensitivity. Secondly, the scattering also leads to an increase in stray light, which increases the relative contribution of shot noise, and a randomly varying background, both of which reduce the s/n ratios achievable and hamper automated spectral analyses.

Figure 5 A mixture of styrene and water shows the extent of scattering of light (532 nm) from a Raman probe, held externally to the vial, during rapid stirring and after standing to allow phase separation (left: vigorously stirred, right: after 10 min standing).

Several approaches to overcome the problem of scatter include the use of a sleeve or a ball lens to minimize the pathlength between the confocal volume and the probe window. Although often successful, these approaches fail when one of the phases separates and forms a thin film on the surface of the probe or precipitation occurs, both of which distort the optical path.

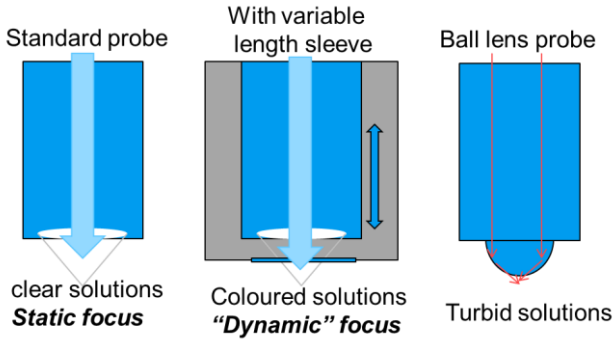

Figure 6 Raman probe arrangements used commonly for in-line reaction monitoring (a) standard arrangement where the confocal volume is several mm from the lens, (b) with a sleeve to reduce distance from confocal volume and surface of probe and (c) ball lens configuration where the distance between the lens and confocal volume is minimized to > 500 microns.

A relatively simple approach to recording spectra in situations where an emulsion is formed by mechanical agitation is to stop agitation and allow the two phases to separate. In cases where the density of the two phases are similar, for example the density of styrene oxide is 1.052 g/mL, such a separation will take at least several minutes, if not longer. Hence, this approach results in a complete loss of time resolution and is impractical in practice. An alternative approach to allowing the contents of an entire reactor to phase separate is to remove relatively small samples and break the emulsion mechanically. The breaking of the emulsion was achieved by withdrawing samples via a thin tube with active pumping (e.g., by using a peristaltic pump) which provided sufficient modulation in pressure in the tube, i.e. pulsed pumping. This approach provides for breaking of the emulsion to achieve slug flow within several seconds even where there is minimum difference in density.

Data acquisition

A prerequisite to the acquisition of Raman spectra in a flow system is that transparency to both the excitation light and the Raman scattering maximized. A quartz flow cell is in principle ideal in this regard, however, in practice the flow characteristics of such a cell and the effects of the connections with tubing were found to be detrimental to the time resolution achieved. A simpler alternative was to use perfluorinated tubing with as low a crystallinity as is available and to place a section of the tube (at least as far away from the inlet so that slug flow has been established) within the confocal volume of the reaction probe. Spectra were acquired during continuous pumping and the spectrum acquired are a weighted sum of all Raman scattering from the phases that are within the confocal volume during the period of acquisition (Figure 7). Hence, the time taken to acquire each spectrum should be less than the average residence time of each phase within the confocal volume. An additional advantage with taking this approach is that although perfluorinated tubing has a relatively weak Raman cross-section, it is sufficient to act as an external intensity reference (vide infra).

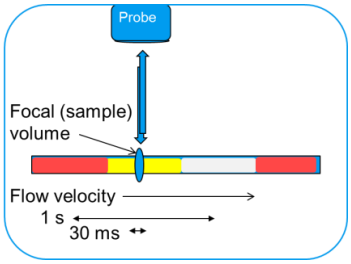

Figure 7 Relation between confocal volume, flow rate and acquisition rate.

These conditions presents a dichotomy in that slower flow rates will allow for increased acquisition times and hence lower limits of detection and higher s/n levels, however, slow flow rates will also reduce the overall number of spectra acquired (vide infra) and decrease the time resolution. Furthermore, breaking of emulsions to yield slug flow presents a lower limit to the flow rates that can be applied. In the present study spectral acquisition rates of between 30 and 60 ms (i.e. 60 and 90 ms including CCD readout time) proved sufficient.

Notwithstanding the loss of signal intensity due to scattering of both excitation light and Raman scattering, a further challenge to in-line monitoring of batch reactions, as mentioned in the introduction, is the often large disparity between the cross-section for various reaction components (e.g., H_2O_2 and styrene, Figure 1). The difference in response presents an upper limit on spectral acquisition, i.e. saturation of the CCD in the case of the organic phase.

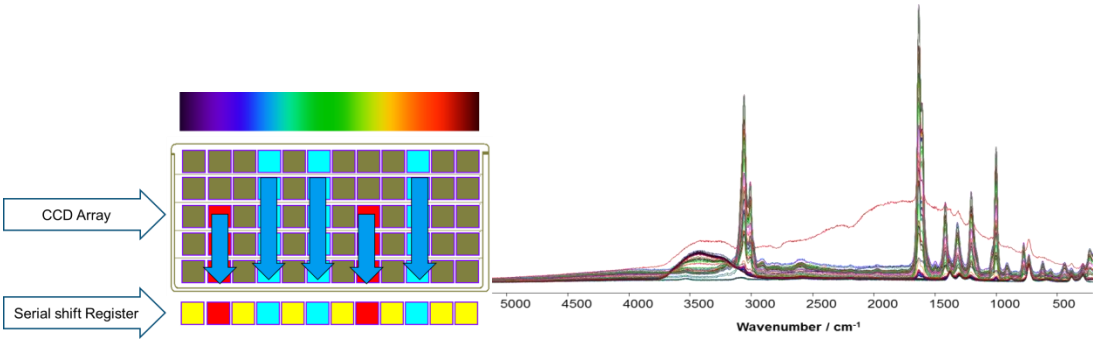

Figure 8 Acquisition of 100 spectra in one minute from a styrene/H_2O_2 (1 M aq.) 50/50 % mixture flowing through a FEP tube.

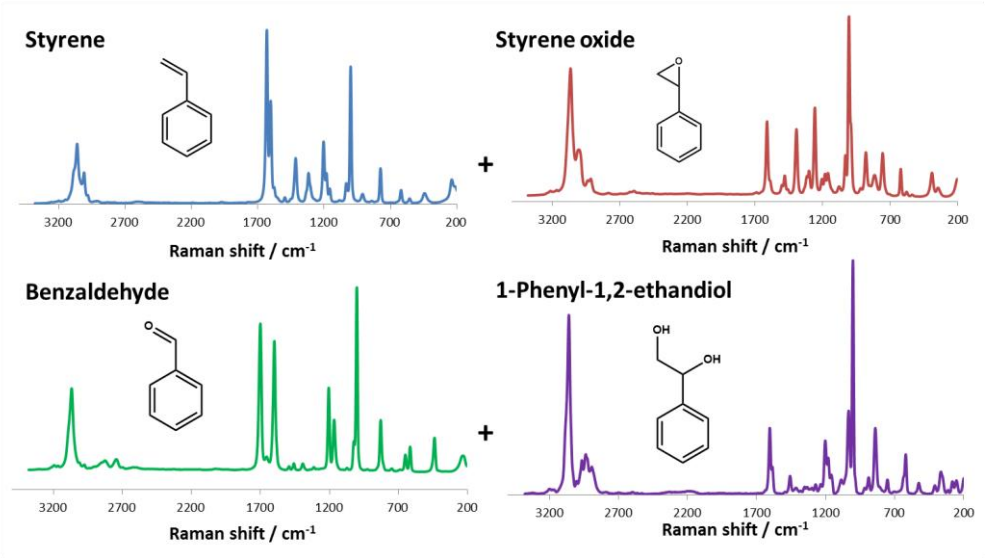

Figure 9 Spectra of individual components and relative Raman cross-sections. The spectra of mixtures are deconvoluted using the weighted sum of each of the pure spectra, i.e. a . (Styrene) + b . (Styr. Oxide) + c . (water)+ … + n . (n-component)

Spectral sorting

After the acquisition of 1000 spectra (ca. 1 min) the spectra obtained were sorted and averaged (this process can be automated) to increase the S/N ratio and increase repeatability (Figure 10). The use of an automated routine for sorting the spectra of each of the phases and discarding spectra obtained from air pockets or combinations of contributions from both phases) makes the rapid analysis (up to 1000 spectra/min) possible. The sorting routine is based on the recognition of the Raman scattering intensity of the organic or aqueous phases in the region of the X-H stretching modes (where X is O or C, respectively, for aqueous and organic phases). The strength of this method lies in that these stretching modes are at distinct wavelength ranges for each phase and intensities are relatively invariant over the reaction in the present case. In the case that an organic phase does not have distinct C-H stretching modes available that persist over the entire reaction another part of the spectrum, e.g., at which an isosbestic point is maintained, can be selected. Using the automated sorting routine, out of 1000 spectra acquired over one minute, 66 spectra of the aqueous phase and 256 spectra of the organic phase were collected.

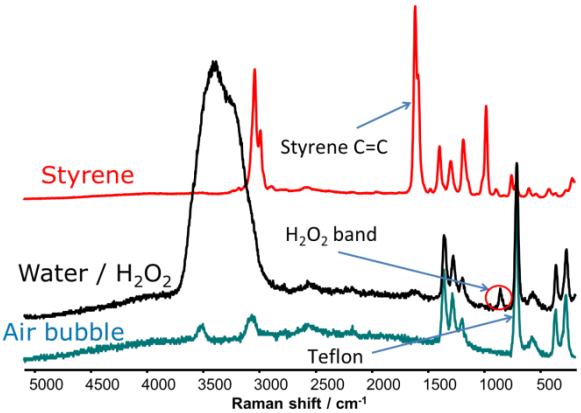

Figure 10 Spectra acquired during sampling of a 1:1 v/v mixture of styrene/H_2O_2 (1 M aqueous) by flowing through a FEP tube.

The areas of bands of interests from the aqueous spectra and the organic spectra were integrated, Figure 10, giving a relatively large standard deviation from the expected integrated value of a single slug measurement.

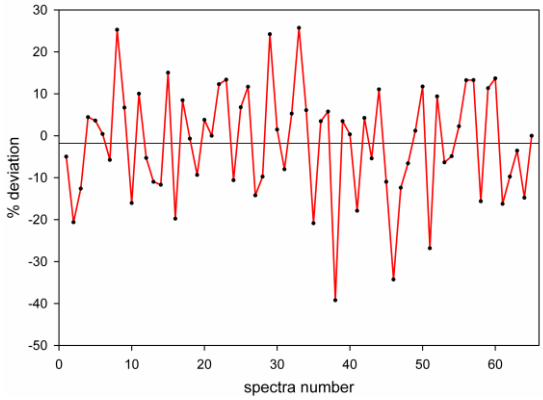

Figure 11 Deviation % from the expected value for the integration of the peroxide (O-O stretching) signal in the aqueous phase. The black horizontal line represents the median value obtained from the 66 spectra of the aqueous phase.

Although a single 60 ms acquisition spectrum is imprecise, the average of the spectra of each phase can provide a deviation of ca. 2%. It should be noted that the precise positioning and focusing as well as the stability of the light source are important in the precision and reproducibility of the measurements achieved.

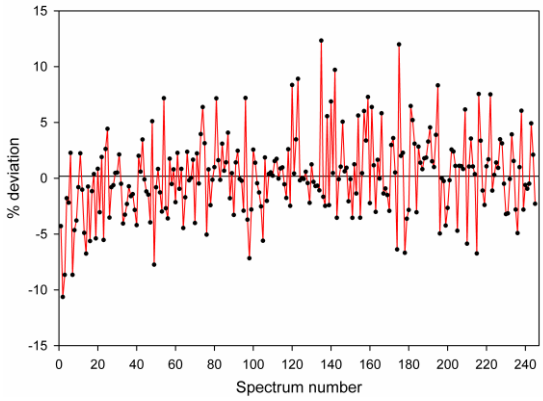

Figure 12. Deviation % from the expected value for the integration of the (C=C stretching) signal in the styrene phase. The black horizontal line represents the median value obtained from the whole 256 values of the organic phase.

Spectral analysis

Rapid analysis of the data to obtain information on conversion in the present system is facilitated by the relatively low extent of partition of the organic compounds into the aqueous phase (*vide infra*). Furthermore, partition of H_2O_2 into the organic phase is minimal (< 5%). Hence, a good first approximation can be obtained from the Raman spectra of the organic phase as to the extent of substrate conversion. The simplest approach is to fit the spectra obtained with a linear weighted combination of the spectra of neat styrene and styrene oxide to provide a convolution spectrum which overlaps optimally with spectra of various mixtures of the two components. In the present case, manual fitting by variation of the weight of each component was achieved with visual inspection of the residual plot as well as by linear least square

regression. Although, the real spectra could be fitted accurately, caution should be exercised in method development to restrict automated fitting algorithms to take into account that the components are not independent variables. Changes in the polarity of the medium, as the ratio of styrene and the more polar styrene oxide changes, can cause, albeit in this case very minor, shifts in peak position. Notably the partitioning of 1-phenyl-1,2-ethanediol and benzaldehyde between the aqueous and organic phase is dependent on the conversion of styrene to styrene oxide also, however the sensitivity is much less than for styrene oxide itself (Figure 14).

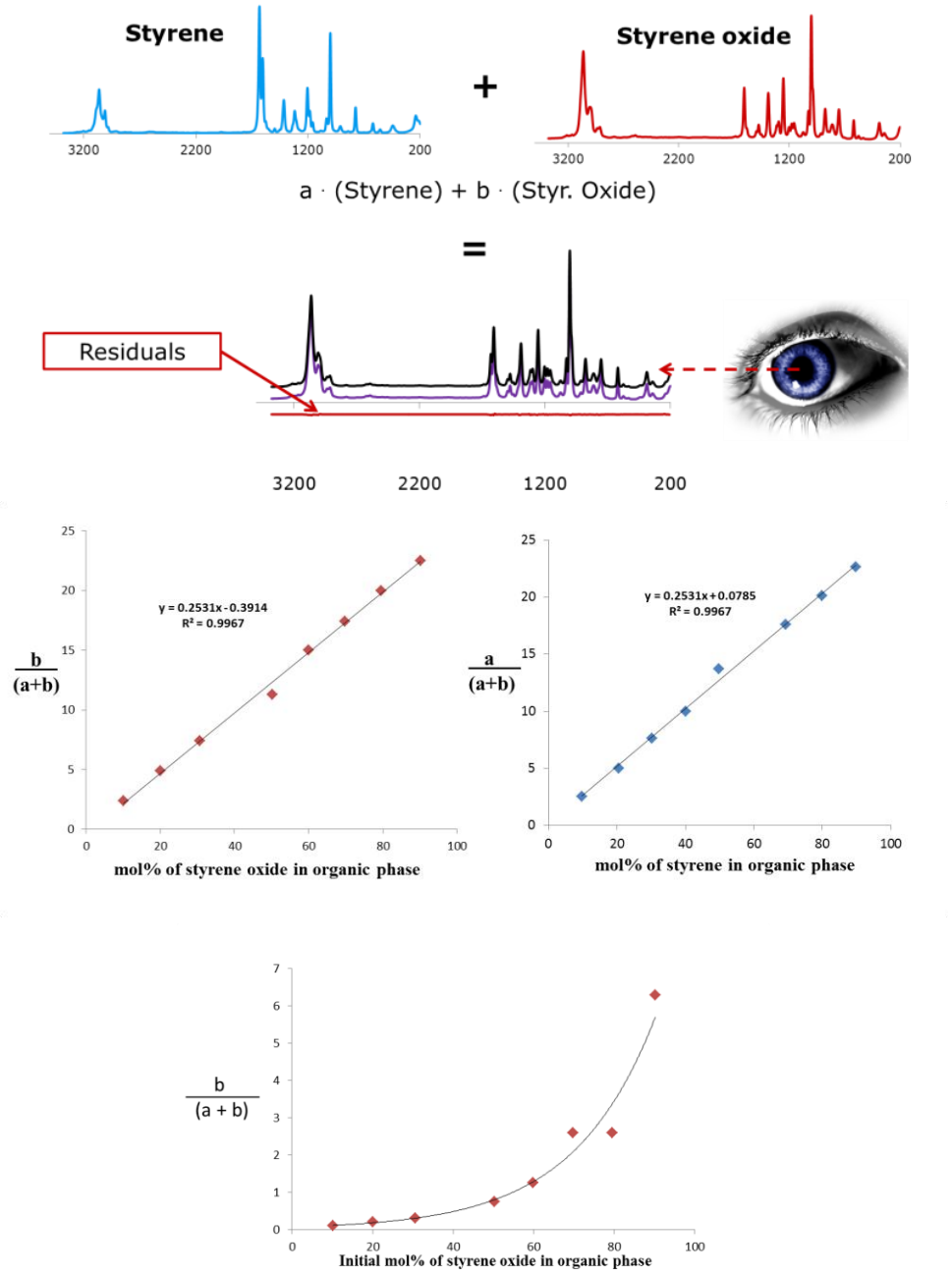

Figure 13 A linear combination of the spectra of styrene and styrene oxide were used to fit individual spectra of mixtures (shown as spectra with residual plots above). The ratio obtained was used together with standard curves for known mole fractions of mixtures (centre). The ratio of styrene oxide and 1-phenyl-1,2-ethanediol products in the aqueous and organic phases could be estimated also, however, the low concentrations reduced the accuracy due to low s/n ratios (lower plot). The y axis in each graph represents a dimensionless number obtained from fitting of component spectra.

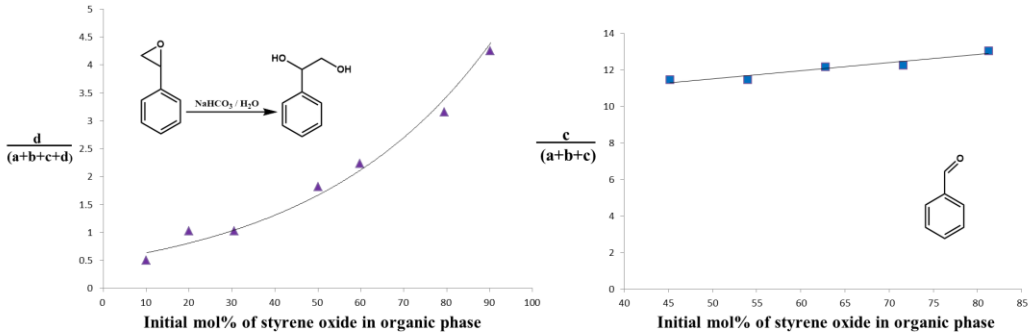

Figure 14 Partitioning of 1-phenyl-1,2-ethanediol (left) and benzaldehyde (right) between organic and aqueous phases at low concentrations (simulated reaction conditions). The y axis represents a dimensionless number obtained from fitting of component spectra.

6.4 Conclusions

As discussed in the introduction, the use of two phase reaction conditions provides an opportunity to aid separations and thereby reduce the energy demands of synthetic processes. In this chapter a major challenge to implementing such reactions is addressed; in-line reaction progress analysis. It is shown that, using flow techniques, rapid phase separation can be achieved and by rapid spectral acquisition allows for high quality spectra to be obtained rapidly. The key challenge tackled in this chapter is spectral sorting and recombination followed by quantitative determination through fitting against a training set. Future studies will apply this approach to monitor on going reactions.

6.5 References

[1] M. P. Dudukovic, F. Larachi, P. L. Mills, *Catal. Rev. Sci. Eng*. **2002**, *44*, 123.
[2] See for example; a) J. Antes, D. Boskovic, H. Krause, S. Loebbecke, N. Lutz, T. Tuercke and W. Schweikert, *Chem. Eng. Res. Des*. **2003**, *81*, 760. b) A. P. Harvey, M. R. Mackley, T. Seliger, *J. Chem. Technol. Biotechnol*. **2003**, *78*, 338.
[3] C. W. Kohlpaintner, R. W. Fischer, B. Cornils, *Appl. Catal A-Gen*., **2001**, *221*, 219.
[4] M. Zawadzki, F. A. e Silva, U. Domańska, J. A. P. Coutinho, S. P. M. Ventura, *Green Chem*., **2016**, *18*, 3527.
[5] S. Hocde, C. Pledel-Boussard, D. Le Coq, G. Fonteneau, J. Lucas, *Proc. SPIE-Int. Soc. Opt. Eng*., **1999**, 50, 3849.
[6] S. Hardy, I. M. de Wispelaere, W. Leitner, M. A. Liauw, *Analyst*, **2013**, *138*, 819.
[7] W. A. Shafer, S. Hobbs, J. Rehm, D. A. Rakestraw, C. Orella, M. Mclaughlin, Z. Ge, C. J. Welch, *Org. Process. Res. Dev.*, **2007**, *11*, 870.
[8] W. N. Delgass, "Spectroscopy in Heterogeneous Catalysis", Academic Press, New York, **1979.**
[9] a) X. Gao, J. Chorover, *Environ. Chem.* **2012**, *9*, 148. b) S. J. Tinnemans, J. G. Mesu, K. Kervinen, T. Visser, T. A. Nijhuis, A. M. D. E. Beale, Keller, A. M. J. Van Der Eerden, B. M. Weckhuysen, *Catalysis Today*, **2006**, *113*, 3. c) H. Hua, M. A. Dubé, *Polym. React. Eng*., **2002**, *10*, 21.
[10] M. F. Roberto, T. I. Dearing, C. W. Branham, O. Bleie, B. J. Marquardt, *Processes* **2014**, *2*, 24.
[11] J. W. de Boer, W. R. Browne, J. Brinksma, P. L. Alsters, R. Hage, B. L. Feringa, *Inorg. Chem*., **2007**, *46*, 6353.
[12] P. Griffith, G. B. Wallis, J. *Heat Transfer* **1961**, *83*, 307.
[13] J. R. Burns, C. Ramshaw, *Lab Chip*, **2001**, *1*, 10.

Chapter 7

Towards (S,S,S)Trispyrrolidine-1,4,7-triazacyclononane

The drive to establish an ever more detailed mechanistic understanding of the catalytic activity of $Mn(III,III)_2$(tmtacn) dicarboxylato based complexes (Chapter 2) in the oxidation of alkenes requires ever more sophisticated approaches for revealing the nature of the species that engages directly in substrate oxidation. In this chapter efforts towards the synthesis of a chiral analogue of tmtacn, i.e. (S,S,S)Trispyrrolidine-1,4,7-triazacyclononane (tptacn), are described in detail together with an overview of the ultimate objective of their synthesis.

7.1 Introduction

Previously the use of chiral carboxylic acids has been shown to provide for enantioselectivity in the *cis*-dihydroxylation of chromene and the use of a chiral analogue of the tmtacn ligand was shown by Bolm and coworkers to provide for enantioselectivity in the epoxidation of alkenes.[1]

As already discussed in Chapter 4 the dimanganese bis-carboxylato species is most likely structurally similar to species that engages with alkenes in their oxidation with hydrogen peroxide. The drive to establish an ever more detailed mechanistic understanding of the catalytic activity of $[Mn(III,III)_2(\mu\text{-}O)(\mu\text{-}RCO_2)_2(tmtacn)_2]^{2+}$ bis-carboxylato based complexes (Chapter 4) in the oxidation of alkenes requires even more sophisticated approaches for revealing the nature of the species that engages directly in substrate oxidation. Previous studies have identified a number of chiral carboxylates that, when used as ligands with $[Mn(IV,IV)_2(\mu\text{-}O)_3(tmtacn)_2]^{2+}$ provide for the asymmetric cis-dihydroxylation of alkenes, in particular chromene in an enantiomeric excess of up to 54 %.[2] Earlier reports by Bolm et al. focused on the use of chiral analogues of the 1,4,7-triazacyclononane (tmtacn) ligand, in the synthesis of a series of chiral complexes. Manganese complexes of these ligands enabled the asymmetric epoxidation of alkenes such as styrene (43 % e.e.), cis-β-methylstyrene (55 % e.e.) and chromene (40 % e.e.).[1] An alternative class of chiral tmtacn ligands in which the chirality is present in the macrocyclic structure has been derived from the cyclization of a proline trimer (Figure 1 – top left), however, although a high conversion of substrates was achieved (88 %), the enantiomeric excess achieved was limited (20 % e.e.).[3] A point of note in these studies, however, is that longer reaction times and an increase in oxidant leads to formation of other species that may not retain the chiral ligand, inferred by the decrease in enantiomeric excess over the reaction. Furthermore in these studies the role of carboxylic acids had not yet been recognized, which may explain their limited scope. Nevertheless the observation of enantioselectivity, albeit low, confirms that the ligands are part of the species that engages with the substrates.

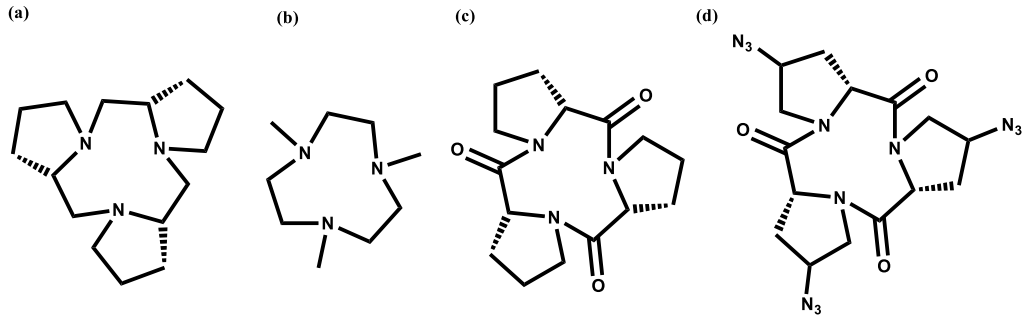

Figure 1 (a) (S,S,S)Trispyrrolidine-1,4,7-triazacyclononane (tptacn).[3] (b) The ligand tmtacn. (c) Cyclo(tri-L-proline), the precursor of tptacn. (d) Azide derivative of the Cyclo(tri-L-proline) recently (2006) reported by Wennemers et. al.[6]

The synthesis of dinuclear manganese complexes, analogous to the $[Mn(III,III)_2(\mu\text{-}O)(\mu\text{-}RCO_2)_2(tmtacn)_2]^{2+}$ complexes discussed in chapter 4, with chiral ligands such as trispyrrolidine-1,4,7-triazacyclononane (tptacn) would allow for match/mismatch experiments to be performed with chiral carboxylate bridges, enabling the the nuclearity of the active complex to be established further. Indeed such complexes would be of further use in allowing techniques such as CD spectroscopy to be applied in studying their reactions with H_2O_2. For these reasons, the synthesis of the cyclo(tri-L-proline) (Figure 1a) was seen as a worthwhile goal. Although the

synthesis of the tptacn by reduction of the cyclo(tri-L-proline) was described in the literature recently,[3] the synthetic procedure for obtaining the cyclo(tri-L-proline) was reported almost 40 years ago and therefore considered obsolete in light of the advances in peptide chemistry in the intervening years.[4,5] Indeed a recent synthesis of an azide derivative of the cyclotriproline was considered more prospectful in the design of a new synthetic path.[6] In this chapter, a robust synthesis and characterization of the cyclic trisproline based on earlier studies by de Boer[7] is described in detail, with emphasis on the methods used for purification and determination of retention of diastereomeric and enantiomeric excess.

7.2 Experimental section.

The methyl ester of proline chloride salt, the N-Boc protected Proline, the ECD and HATU were used as provided from Bachem. The HOBt and DIPEA were used as provided from Sigma-Aldrich. All solvents used were spectroscopic grade. The glassware used was dried before every coupling reaction and Boc deprotection.

Dimerization of Proline

10.02 g (47.15 mmol) of Boc protected L-proline (Boc-ProOH, Bachem), 9.86 g (63.53 mmol) of 1-ethyl-3-(3-dimethylaminopropyl)carbodiimide (EDC, Bachem) and 7.30 (54.07 mmol) of 1-hydroxybenzotriazole hydrate (HOBt, Sigma-Aldrich) were dissolved in 300 mL of anhydrous dichloromethane (DCM, Labscan) in a round bottomed flask. The mixture is stirred at room temperature for 1 h to favour the formation of the benzotriazol Boc-prolinate ester (Boc-Pro-OBt). The solution containing Boc-Pro-OBt was transferred dropwise over 1 h to a round bottom flask containing 24 mL (137.7 mmol) of ethyldiisopropylamine (DIPEA, Sigma-Aldrich) and 7.86 g (47.46 mmol) of L-Proline methyl ester hydrochloride ([HCl · Pro-OMe], Bachem). After addition was complete the reaction mixture was stirred at room temperature for 48 h. The organic layer was washed with brine (100 mL), three times with bicarbonate saturated water (200 mL), three times with 1 M aqueous sodium bisulfate (200 mL) and finally with brine (100 mL). The organic layer was dried with anhydrous Na_2SO_4 and filtrated by gravity followed by removal of solvent in vacuo. The crude yield was 14.67 g. The product is purified by flash silica column chromatography (automatic columning machine: DCM with a gradient of methanol up to 2 % vol over 30 min) to remove side products, primarily HOBt. A transparent viscous oil (**2**) was obtained (11.75 g). (Exact mass: 326.20; ^{1}H-NMR (400 MHz, $CDCl_3$): t-Boc: [9H, d: 1.36, 1.42 ppm], pyr-CH_2: [8H, m, 1.78 – 2.25 ppm], Pyr-CH_2 [4H, m, 3.33 – 3.80 ppm], -OCH_3: [3H, s, 3.67 ppm], Pyr-CH-N: [2H, m, 4.30 – 4.62 ppm]; ^{13}C-NMR (200 MHz, $CDCl_3$): mix of rotamers [23.4, 23.9, 24.8, 24.9, 28.2, 28.3, 28.5, 28.7, 28.9, 29.8, 46.3, 46.3, 46.5, 46.7, 51.9, 52.0, 52.1, 57.5, 58.5, 79.2, 79.3, 153.6, 154.4, 171.0, 171.4, 172.5, 172.8 ppm]).

Saponification of Boc-Pro-Pro-OMe

11.75 g (36.0 mmol) of **2** were stirred vigorously together with circa 200 mL of NaOH (2 M aqueous solution) in a round bottom flask until the mixture became homogeneous (ca.30 min). The aqueous solution was neutralized with HCl (conc.) and extracted 5 times with DCM. The DCM is then dried over anhydrous Na_2SO_4 followed by removal of solvent in vacuo yielding 8.24 g (73 %; 26.14 mmol) of **3** as white crystals (T_{melt}: 176-177 °C; ^{1}H-NMR (400 MHz, $CDCl_3$): t-Boc: [2 x s, 9H, 1.39, 1.45 ppm], Pyr-CH_2:[8H, m, 1.85-2.41 ppm], Pyr-CH_2:[4H, m, 3.38-3.80 ppm], Pyr-CH-N:[2H, m, 4.37-4.68 ppm], mixture of rotamers; ^{13}C-NMR (200 MHz, $CDCl_3$): mixture of

rotamers: [23.7, 24.3, 25.0, 27.0, 27.2, 28.4, 28.4, 29.4, 30.2, 46.7, 46.9, 47.3, 57.6, 57.7, 59.9, 60.0, 79.8, 79.9, 153.5, 154.6, 172.2, 172.5, 174.4, 174.7 ppm]).

Proline trimerisation

In a round bottom flask containing 200 mL of DCM 8.13 g (26.18 mmol) of **3** (Boc-Pro_2-OH), 4.36 g (32.29 mmol) of HOBt monohydrate and 4.46 g (28.77 mmol) of EDC were dissolved, in that order. The mixture was stirred at room temperature for 1 h and then transferred dropwise into a second round bottom flask containing 100 mL of DCM, 4.35 g (26.18 mmol) of [HCl · Pro-OMe] and 12 mL (68.8 mmol) of DIPEA. After stirring for 48 h at room temperature, the DCM solution was washed, respectively with brine, three times with saturated aqueous $NaHCO_3$, three with aqueous $NaHSO_4$ (1 M) and finally with brine. The DCM layer was reduced in vacuo to yield a non-volatile yellowish oily residue. Column chromatography (with a gradient over 30 min to 98:2 DCM/MeOH) the oil yielded 8.67 g (78.3 %) of a transparent viscous oil corresponding to Boc-Pro_3-OMe. (Exact mass + Na^+: 446.23; ^{1}H-NMR (400 MHz, $CDCl_3$): t-Boc: [9H, d: 1.38, 1.42 ppm], pyr-CH_2: [12H, m, 1.70 – 2.29 ppm], Pyr-CH_2 [4H, m, 3.33 – 3.80 ppm], -OCH_3: [3H, s, 3.68 ppm], Pyr-CH-N: [4.30 – 4.80 ppm]; ^{13}C-NMR: mix of rotamers:[23.5, 24.1, 24.8, 24.8, 27.8, 28.0, 28.4, 28.5, 28.7, 28.9, 29.9, 46.5, 46.6, 46.7, 46.9, 52.1, 57.6, 57.7, 58.4, 58.5, 79.1, 79.3, 153.7, 154.5, 170.4, 170.7, 170.8, 171.3, 172.7 ppm]).

Saponification of Boc-Pro_3-OMe

2.5 g (5.9 mmol) of Boc-Pro_3-OMe was mixed with 55 mL of a 2 M NaOH aqueous solution in a round bottomed flask until the oil dissolved completely and the mixture became homogeneous (ca. 40 min). Insoluble residuals were removed by addition of 2 mL of DCM followed by separation and neutralization of the aqueous layer with HCl (conc.) until the pH was ca. 5 at which point the solution became turbid. The product was extracted, and washed with 150 mL of DCM three times and finally with 50 mL of ethyl acetate. The organic solvents used for extraction were combined and dried with anhydrous Na_2SO_4, filtered and the solvent removed in vacuo. 2.31 g (95 %) of white fluffy crystals of Boc-Pro_3-OH were obtained. (Exact Mass + Na^+: 432.21; Melting point: 199 - 200 °C; ^{1}H-NMR (400 MHz, CDCl3): t-Boc: [9H, d: 1.38, 1.43 ppm], pyr-CH_2: [12H, m, 1.72 – 2.30 ppm], Pyr-CH_2 [6H, m, 3.30 – 3.87 ppm], Pyr-CH-N: [4H, m, 4.30 – 4.79 ppm]; ^{13}C-NMR (400 MHz, $CDCl_3$): mix of rotamers [23.6, 24.1, 24.9, 25.1, 27.5, 27.6, 28.0, 28.1, 28.4, 28.5, 28.9, 29.8, 46.6, 46.8, 46.9, 47.3, 57.7, 57.8, 59.6, 59.6, 79.4, 79.5, 153.6, 154.6, 171. 6, 171.4, 171.8, 172.5, 173.0, 173.1, 173.2 ppm]).

Deprotection of the Boc group

2.31 g (5.64 mmol) of Boc-Pro_3-OH were dissolved in 14 mL of dry DCM in a dry two necked round bottom flask. 7 mL of HCl (4 M) in dioxane (Sigma-Aldrich) were added and the mixture stirred at room temperature for 2 h during which time bubbles of CO_2 were observed. The solvent was removed in vacuo under reduced pressure (oil pump to remove the dioxane), yielding 2.5 g of product (which contains dioxane, 50% by NMR). NMR spectroscopy confirmed that the reaction went to completion. (Exact Mass: 309.17; ^{1}H-NMR(400 MHz, $CNCD_3$): pyr-CH_2: [12H, m, 1.72 – 2.52 ppm], Pyr-CH_2 [6H, m, 3.20 – 3.80 ppm], Pyr-CH-N: [4H, m, 4.30 – 4.79 ppm]; ^{13}C-NMR (200 MHz, D_2O): [pyrolidine ring: 24.5, 25.2, 28.5, 28.9, 29.3 ppm], [CH_2-N: 47.3, 48.0, 48.3 ppm],[αCH: 59.6, 59.7, 60.1 ppm], [C=O: 168.2, 172.1, 176.4 ppm]).

Cyclization of the trisproline:

1.2 g (3.12 mmol) of 1-[bis(dimethylamino)methylene]1-H-1,2,3-triazolo[4,5-b]pyridinium 3 – oxide hexafluorophospate (HATU) and 1.6 mL (8.5 mmol) of DIPEA were dissolved in 100 mL of dimethyl formamide (DMF) with vigorous stirring at room temperature in a dried round bottom flask. 500 mg of triproline chloridrate (1.45 mmol) dissolved in 18 mL of DMF was injected over 1 h and the reaction stirred for a further 23 h. The solvent was removed in vacuo yielding 2.3 g of non-volatile residues. The crude is washed with ethyl acetate and the solids washed again with DCM and filtrate. The DCM layer was dried in vacuo yielding 235 mg of the trisproline (Yield: 50 %; Exact Mass: 291.1; ^{1}H-NMR in $CDCl_3$: pyrrolidine ring 12H [1.8 – 2.8 ppm], α-N-6H [3.5 – 3.9 ppm], chiral-α-N-3H [4.4 – 4.8 ppm] ; ^{13}C-NMR: Pyrrolidine ring C [24.6 ppm], pyrrolidine ring [28.0 ppm], [47.6 ppm], [58.5 ppm], Carboxylic carbon [171.5 ppm]).

(^{13}C-NMR assignments were made by comparison with spectra obtained using the Gaussian09 rev-C[8] Density Functional Theory (DFT) software package with the Gauge-Independent Atomic Orbital (GIAO)[9] method and the functional and basis set B3LYP/6-311+G (2d,2p)[10] after geometry optimization on the (S,S,S) and (R,S,S)-cyclotriproline using the smd model for simulating the solvent environment).

7.3 Results and Discussion

Synthetic approach

The peptide coupling reactions (steps 1, 3 and 6, Scheme 1) were adapted from the procedure reported earlier by Sontag et al.[6] and de Boer.[7] The first two reaction steps use EDC to form a reactive Benzotriazol-oxy proline ester followed by coupling via a mechanism common to carbodiimmides.[11,12] The difficulty in these steps lies in the purification of the product, especially in the removal of the spent coupling reagents, which is achieved by a series of washing steps to alternately remove residual compounds that are more hydrophilic than the product. Specifically the brine wash is used to remove unreacted proline (present as a water soluble zwitterion), as water alone does not partition sufficiently from dichloromethane. Aqueous sodium bicarbonate removes the sodium salt of HOBt and $NaHSO_4$ protonates the DIPEA, EDC [13] and amine side products rendering them water soluble also. The final washing with brine is used to remove water from the organic layer. This extraction protocol provides a product in already high purity and makes further purification by chromatography feasible. Conditions for column chromatography, using an automated columning system, were based on those reported by de Boer,[7] thin layer chromatography and chromatograms (UV and ECD). The latter were especially useful in distinguishing fractions containing UV absorbing contaminants (e.g., HOBt) from those with relatively little absorbance at 350 and 280 nm.

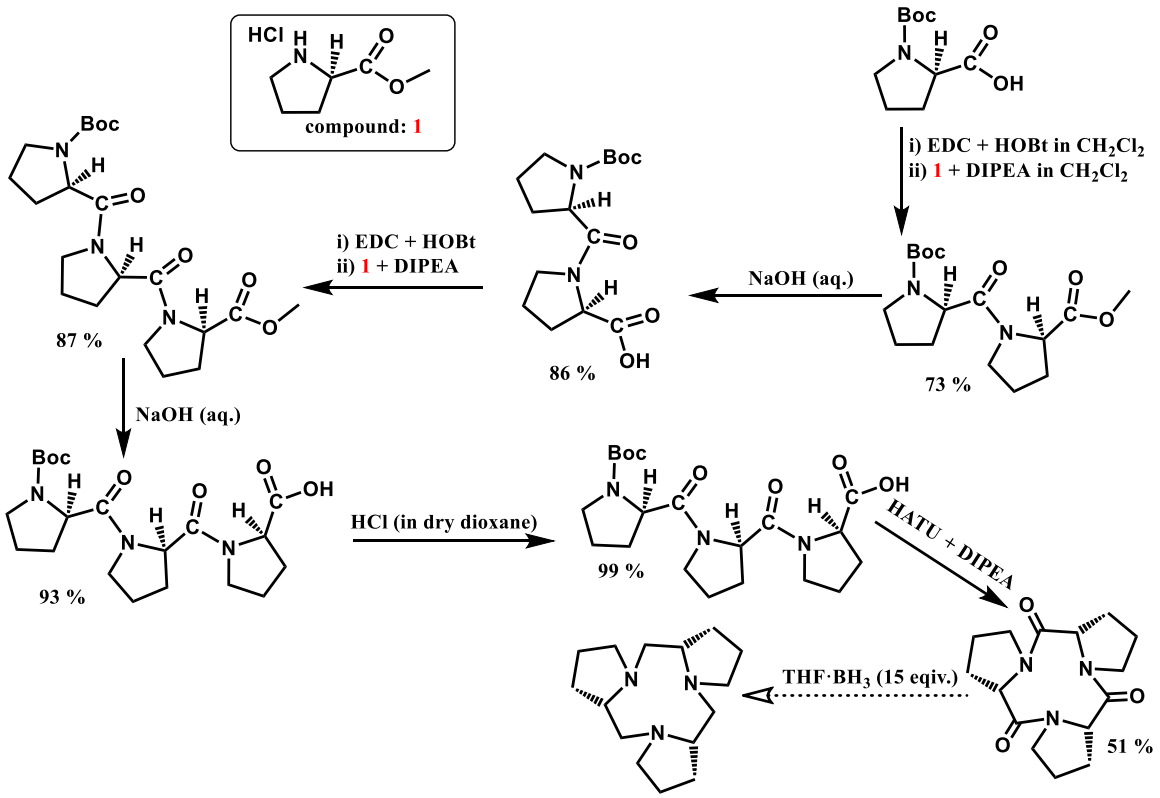

Scheme 1 Overview of the reactions.

In the cyclization of the proline trimer (**step 6**) an alternative to the coupling reagent EDC was used since improved cyclization (in terms of yield and epimerization) were reported with derivatives of 1-hydroxy-7-azabenzotriazole (HOAt) and uronium salts earlier [14,15]. Wennemers et. al.[6a] reported prompted the choice of HATU for the cyclization. The proline trimer in this case is added to the reaction flask slowly to ensure that the concentration of the reactant is always well below the effective molarity (EM).[16] The workup in this specific reaction is different because the desired product and many by side products are significantly soluble in water. Washing with ethyl acetate[5] was used to remove residual DMF, DIPEA and unreacted HATU. The insolubility of HOAt and the uronium salts in dicholoromethane allowed for their removal. The cyclized triproline was obtained with a good degree of purity and without apparent epimerization, as determined by ^{1}H-NMR and ^{13}C-NMR spectroscopy. This approach is a straightforward alternative to earlier procedures using purification by sublimation[5] or by reverse phase (Sephadex LH20) column chromatography with DMF as eluent[17].

The saponification reactions (**step 2** and **4**) were adapted from the procedure of de Boer and earlier reports.[6b] Dissolution of the methyl ester in aqueous sodium hydroxide proved to be straightforward with no evidence of epimerization and allowed for separation of the product upon acidification and extraction with dichloromethane.

The removal of the Boc group (**step 5**) is described widely, and proceeds by protonation of the Boc group using a strong acid such as HCl, trifluoroacetic acid. HCl in dioxane was chosen as it was reported to be effective for related compounds.[6a,18] Initial attempts using only dioxane as solvent were unsuccessful due to limited solubility, which prompted the use of dichloromethane/dioxane mixtures which dissolved the reactant fully but not the product which precipitated directly.

^{13}C NMR characterization of cyclic trisproline

Although the synthesis of the cyclic trisproline was successful; a key challenge is to avoid epimerization during the work-up and purification. The high symmetry and the relative structural rigidity of the cyclo-tris-(L)-proline presents advantages in regard to its study by DFT methods as it limits the number of conformers that must be considered in the analysis. DFT geometry optimization with the B3LYP/6-311+G (2d,2p) in water model (smd), confirmed the geometrical and magnetic equivalence of sets of fragments for the SSS or RRR diasteroisomers, while the symmetry is broken for the SRR or RSS diastereoisomers. The ^{13}C- NMR spectra were simulated (B3LYP/6-311+G (2d,2p)) in water (with the smd model) with the method Gauge-Independent Atomic Orbital (GIAO) and using as TMS (B3LYP/6-311+G(2d,p) GIAO) as reference. A near exact match of the calculated and experimental data were obtained for the SSS-cyclotriproline, while for RSS-cyclotriproline the pattern of signals predicted were distinct from the experimental data.

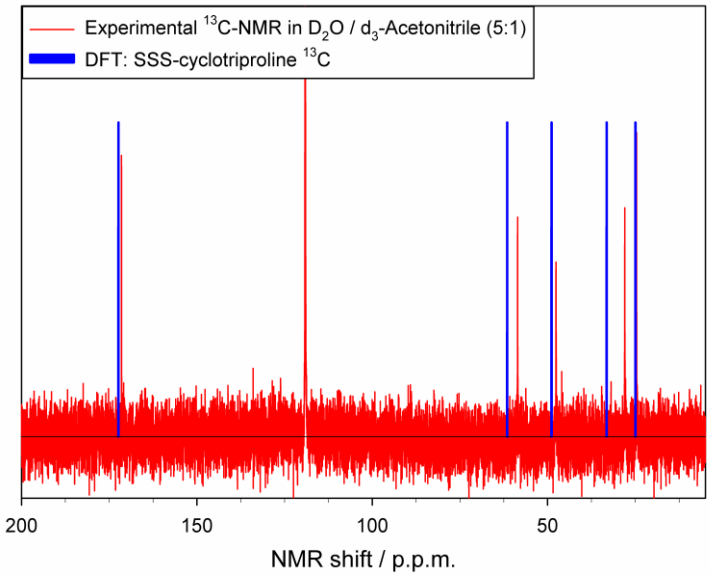

Figure 2 Comparison between the measured ^{13}C-NMR spectrum, from the purified step 5 (red line), and the calculated ^{13}C-NMR spectrum of the SSS-cyclotriproline (blue line).

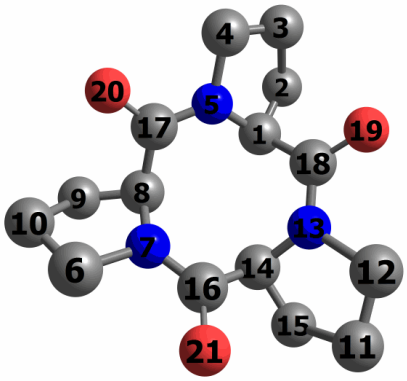

Figure 3 DFT calculated ^{13}C-NMR spectrum: {Atoms 16, 17, 18} 172.38 ppm, {Atoms 1, 8, 14} 61.54 ppm, {Atoms 4, 6, 12} 48.90 ppm, {Atoms 2, 9, 15} 33.18 ppm and {Atom 3, 10, 11} 24.96 ppm.

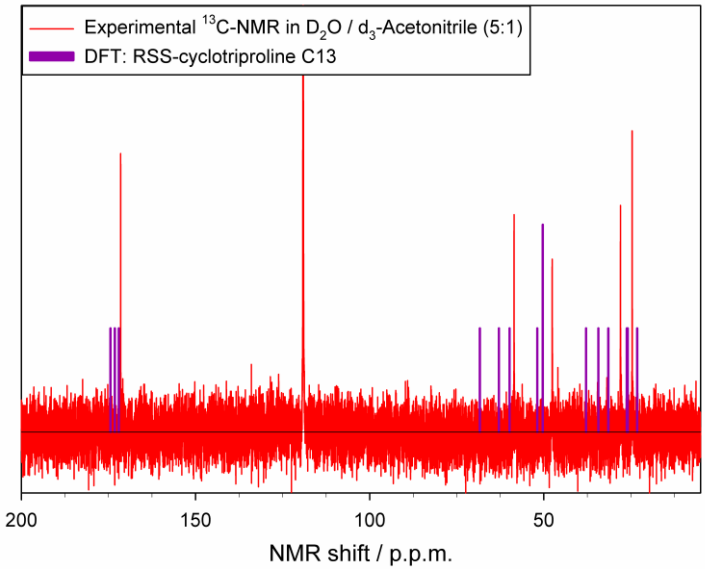

Figure 4 Comparison between the measured ^{13}C-NMR spectrum, from the purified step 5 (red line), and the calculated ^{13}C-NMR spectrum of the RSS-cyclotriproline (blue line).

Although the calculation of the ^{13}C-NMR was performed only on the minimum energy geometry without consideration of all the other possible local minima (through the use of Molecular Dynamics), the shifts obtained are in particularly good agreement with the experimental data due to the rigidity of the structure and the dominance of a single conformation. A notable point in regard to characterization of the Boc protected intermediates is the effect of slow rotation on the ^{1}H NMR spectrum (Figure 4). A double peak in the ^{1}H-NMR spectrum of the N-Boc protected monomer, dimer and trimer coalesces at higher temperatures confirm the slow interconversion to the rotamers.

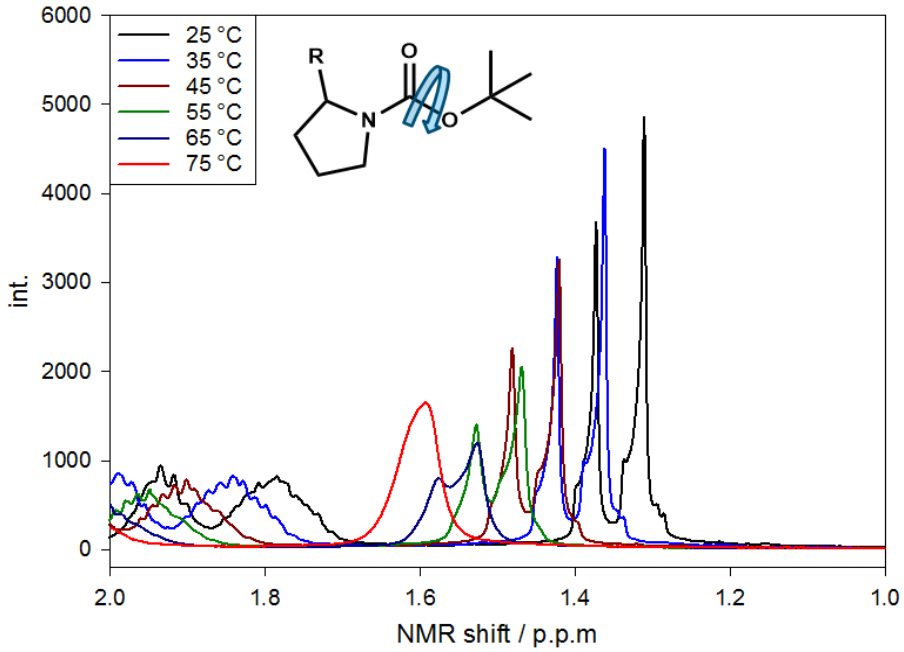

Figure 5 Coalescence of the ^{1}H-NMR signal of the Boc hydrogens with increasing temperature (peaks shift toward higher ppm with increasing temperature).

7.3 Conclusions

The method for the synthesis of cyclic triproline reported in this chapter provides the product in 23 % overall yield. Reducing the dependence on length chromatographic steps was essential in order to make the synthesis economic and in this regard the use of multiple washing steps proved as effective as it was convenient. The confirmation that the reaction proceeded without epimerization was also essential and this was achieved by a combination of ^{13}C NMR spectroscopy and DFT methods. The next and final step in the ligand synthesis is to reduce the peptide bonds to amines, again without loss of diastereomeric excess.

7.4 References

[1] C. Bolm, D. Kadereit, M. Valacchi, *Synlett*, **1997**, 6, 687

[2] J. W. de Boer, W. R. Browne, S. R. Harutyunan, L. Bini, T. D. Tiemersma-Wegman, P. L. Alsters, R. Hage, B. L. Feringa, *Chem. Comm*., **2008**, 3747.

[3] C. Bolm, N. Meyer, G. Raabe, T. Weyhermuller, E. Bothe, *Chem. Commun*., **2000**, 2435.

[4] M. Rothe, K. D. Steffen, I. Rothe, *Angew. Chem., Int. Ed. Engl*., **1965**, 4, 356

[5] J. Vičar, P. Maloň, A Trka, J. Smolíková, I. Fric and K Bláha, *Coll. Czeckslov. Chem. Commun*., **1977**, 42, 2701.

[6] a) LS. Sonntag, S. Schweizer, C. Ochsenfeld, H. Wennemers, *J. Am. Chem. Soc*., **2006**, 128,14697. b) L.-S. Sonntag, M. Langer, S. Ivan, M. Conza, H. Wennemers, *Synlett*, **2004**, *7*, 1270.

[7] Thesis from J. W. de Boer, University of Groningen, **2008**, ISBN: 9789036733366.

[8] *Gaussian*-09, Revision B.01, M. J. Frisch, G. W. Trucks, H. B. Schlegel, G. E. Scuseria, M. A. Robb, J. R. Cheeseman, G. Scalmani, V. Barone, B. Mennucci, G. A. Petersson, H. Nakatsuji, M. Caricato, X. Li, H. P. Hratchian, A. F. Izmaylov, J. Bloino, G. Zheng, J. L. Sonnenberg, M. Hada, M. Ehara, K. Toyota, R. Fukuda, J. Hasegawa, M. Ishida, T. Nakajima, Y. Honda, O. Kitao, H. Nakai, T. Vreven, J. A. Montgomery, Jr., J. E. Peralta, F. Ogliaro, M. Bearpark, J. J. Heyd, E. Brothers, K. N. Kudin, V. N. Staroverov, T. Keith, R. Kobayashi, J. Normand, K. Raghavachari, A. Rendell, J. C. Burant, S. S. Iyengar, J. Tomasi, M. Cossi, N. Rega, J. M. Millam, M. Klene, J. E. Knox, J. B. Cross, V. Bakken, C. Adamo, J. Jaramillo, R. Gomperts, R. E. Stratmann, O. Yazyev, A. J. Austin, R. Cammi, C. Pomelli, J. W. Ochterski, R. L. Martin, K. Morokuma, V. G. Zakrzewski, G. A. Voth, P. Salvador, J. J. Dannenberg, S. Dapprich, A. D. Daniels, O. Farkas, J. B. Foresman, J. V. Ortiz, J. Cioslowski, D. J. Fox, Gaussian, Inc., Wallingford CT, **2010**.

[9] K. Wolinski, J. F. Hilton, P. Pulay*, J. Am. Chem. Soc*., **1990**, *112*, 8251.

[10] a) A. D. Becke, *J. Chem. Phys*. **1993**, *98*, 5648. b) C. Lee, W. Yang, R. G. Parr, *Phys. Rev. B* **1988**, *37*, 785. c) P. J. Hay, W. R. Wadt, *J. Chem. Phys*. **1985**, *82*, 299.

[11] E. Valeur, M. Bradley, *Chem. Soc. Rev*., **2009**, 38, 606.

[12] L. A. Carpino, *J. Am. Chem. Soc*., **1993**, 115, 4397.

[13] J. Sheehan, P. Cruickshank, G. Boshart, *J. Org. Chem.* **1961**,*26*, 2525–2528

[14] F. Albericio, J. M. Bofill, A. El-faham, S. A. Kates, *J. Org. Chem.*, **1998**, 63, 9678.

[15] A. Ehrlich, S. Rothemund, M. Brudel, M. Beyermann, L.A Carpino and M. Bienert, *Tetrahedron Lett*., **1993**, 34, 4781.

[16] V. M. Krishnamurthy, V. Semetey, P. J. Bracher, N. Shen, G. M. Whitesides, *J. Am. Chem. Soc*., **2007**, 129, 1312.

[17] H. Kessler, W. Bermel, A. Friedrich, G. Krack, W. E. Hull, *J. Am. Chem. Soc*., **1982**, *104*, 6304.

[18] E. R. Blout, C. M. Deber, D. A. Torchia, *J. Am. Chem. Soc*, **1971**, *93*, 4893.

Summary

Look before you leap: this English idiom could be the motto for the ethos of the work described in this thesis, in which a deeper understanding of catalysts and the mechanisms by which those catalysts operate was sought. Indeed the aim of this book is to apply key spectroscopic and theoretical methods to understand the mechanism of action of two classes of first row transition metals complexes, which provide thermally accessible pathways towards activation of O_2, NaOCl and H_2O_2 for the oxidation of (in)organic substrates (oxidation catalysis).

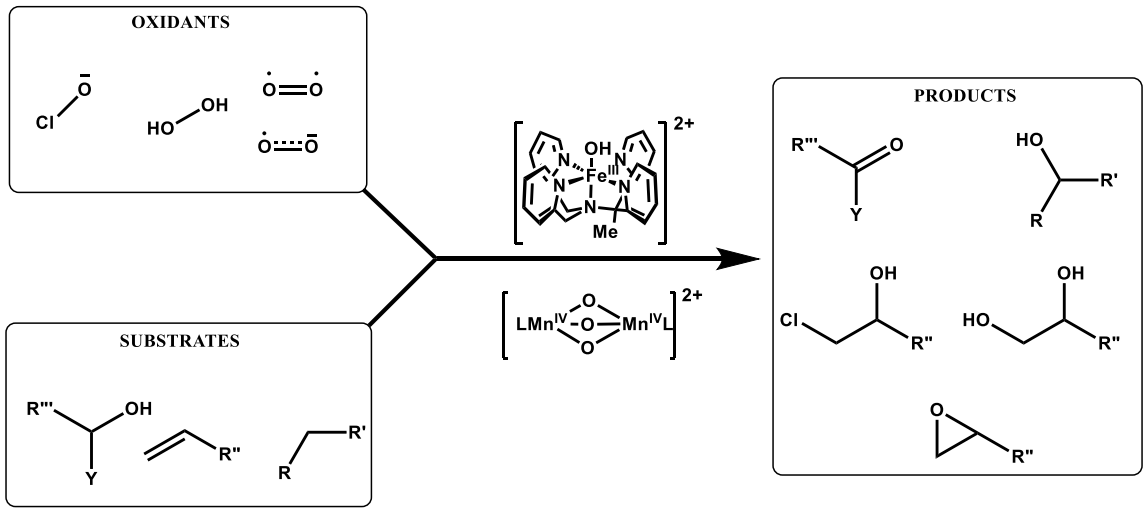

Figure 1 A general scheme of the oxidation catalysts' reactivity with oxidants and organic substrates.

The study of mid-d-transition metal complexes is particularly challenging due to their spin activity.

In Chapter 1 the spectroscopic and theoretical tools used in this thesis are introduced. The major spectroscopic tools used are Raman and resonance Raman spectroscopy combined with UV-vis absorption spectroscopy. Raman spectroscopy is a vibrational technique, which means it discloses information about the structure and bond strengths of a particular compound, and in contrast to its sister technique infrared (IR) spectroscopy, has the advantage that it can be applied readily in many solvents, and especially aqueous solutions. The resonance effect couples electronic excitations with vibrational modes therefore some of these modes will have an enhanced signal by a few tens to several thousand times increasing in this way the sensitivity of the technique. The theoretical methods applied in this thesis, amongst the many post Hartree-Fock methods, consists exclusively of the Density Functional Theory (DFT). DFT has the tremendous advantage that it has been implemented widely over in the last decades, in calculations in the fields discussed in this thesis due to its computational inexpensiveness with respect to its accuracy. DFT was used in this thesis to optimize molecular structures, compute their UV-vis absporption, IR, Raman, resonance Raman and NMR spectra and calculate the thermochemistry of reactions.

In Chapter 2 the reactivity of the iron(II) complexes of N4Py and MeN4Py (Figure 2) with hydrogen peroxide and sodium hypochlorite in aqueous solution were studied with DFT methods. These iron complexes are used as a tool, ultimately, to understand the reactivity of

iron based enzymes including haloperoxidases and halogenases, which are enzymes capable of halogenation of organic compounds. Ultimately, these studies are expected to help in the design of selective and efficient catalysts for a wide range of reactions.

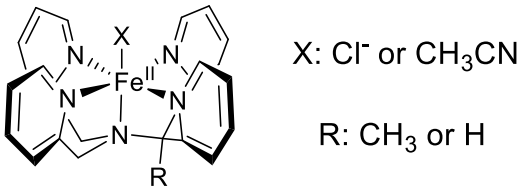

Figure 2 Structure of the [Fe(II)RN4Py-X]$^{2+}$ complexes whose reactivity are described in Chapter 2.

The DFT studies were, thus, used to simulate resonance Raman spectra in order to confirm the assignments of the enhanced vibrational modes observed in experimental studies (involving also isotopic labelling with $H_2{}^{18}O_2/H_2{}^{18}O$), but also for determining the spin states and the thermochemistry of the complexes and their reactants during all the intermediate steps of the reactions. The main results from these DFT studies highlighted the dependence of resonance enhancement of Raman spectra on the spin state of the complexes and revealed the formation of a Fe(IV)=O species by homolytic cleavage of both the $Fe^{(III)}$ hypochlorito and hydroperoxido intermediates.

In Chapter 3, a study of the reactivity of Fe(II) complexes (already discussed in the previous chapter) with dioxygen. The importance of this reactivity lies in their similarity to biologically relevant iron complexes which, activate dioxygen, engage in DNA cleavage thereby affecting DNA replication, therefore damaging, especially tumor, cells. For these reasons an increased understanding of the mechanism of action for activation of oxygen by the complexes shown in Figure 2 could lead to the development of new generation of antitumor drugs (Chemotherapics). The study, performed by DFT methods, starts with the spin states of the relevant complexes and the pH dependent reactivity of the complex FeMeN4Py in water through two pathways in the reaction with O_2 (i.e. outer sphere electron transfer vs. ligand substitution, Figure 3). The study revealed a non-negligible thermodynamic preference for the ligand exchange rather than electron transfer but highlight the closeness in energetic pathways available.

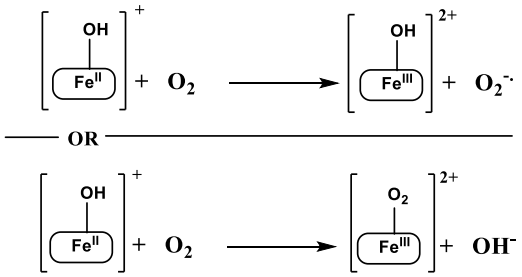

Figure 3 Scheme of the outer sphere electron transfer (top) and ligand exchange (bottom).

Furthermore it was determined that the adduct FeMeN4Py-O_2, formed through the ligand exchange mechanism, has both the kinetic and thermodynamic potential to perform the oxidation of methanol to formaldehyde and the so called purple species Fe(II)MeN4Py-OOH.

In Chapter 4 a distinct class of complexes based on Mn dimers, used in industrial bleaching processes, are introduced and studied spectroscopically in organic (acetonitrile) solvent. The particular reaction studied as described in this chapter is the reduction of a [Mn(IV,IV)$_2$(μ-

$O)_3(tmtacn)_2]^{2+}$ by H_2O_2 in presence of a carboxylic acid (trichloroacetic acid) to form [Mn(III, III)$_2$(μ-O)(trichloroacecato)$_2$(tmtacn)$_2$]$^{2+}$ (Figure 4).

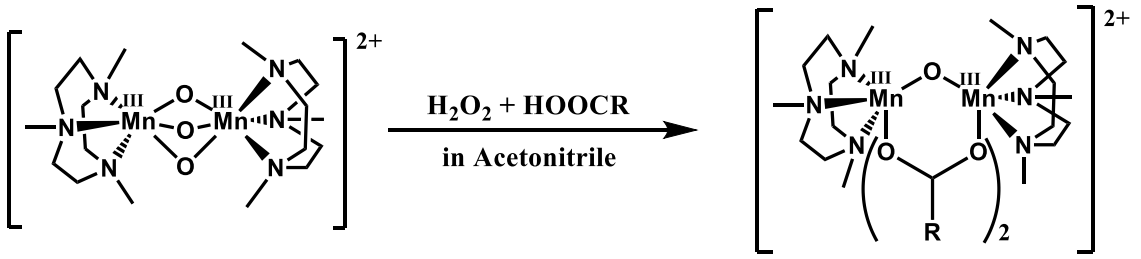

Figure 4 Reduction of the Mn(IV,IV)$_2$ complex to Mn(III, III)$_2$ in the presence of hydrogen peroxide and a carboxylic acid.

During the above mentioned transformation it was observed earlier that intermediates are particularly active in the epoxidation and cis-dihydroxylation of alkenes. This chapter pushes further our detailed knowledge on this reaction by unraveling the autocatalytic nature of the intermediate that is active in the oxidation of alkenes and in the disproportionation of the H_2O_2, furthermore it has been excluded that the active intermediate could be ligand dissociated Mn^{2+} or a Mn(II) dimer with tmtacn ligands. Again a combination of UV-vis absorption, Raman and resonance Raman spectroscopies were key to establishing the previously unexpected reaction of the intermediates with H_2O_2 (disproportionation), which competes directly with substrate oxidation.

In Chapter 5 the catalytic abilities of [Mn(IV,IV)$_2$(μ-O)$_3$(tmtacn)$_2$]$^{2+}$ and Mn^{2+} in water were investigated using Raman spectroscopy, in aqueous solution, under a range of conditions of pH, catalyst concentration , substrate concentration and additives (bicarbonate, borate, acetate, sequestrants). The speciation analysis performed is essential to gain understanding of the transformations the catalyst undergoes to form the species responsible for alkene oxidation. Although the studies did not reveal the molecular structure of the active form of the catalyst responsible of the oxidation the conclusion that can be drawn from these studies is that concurrent activity between two catalysts must be considered in order to understand the complexity of the dependence on conditions observed.

In Chapter 6 a tool for monitoring biphasic reactions using Raman spectroscopy has been developed and tested. In order to have the best contact between phases, a biphasic reaction should work under fine emulsion conditions. Such conditions, however, render impossible the acquisition of useful spectra by any visible/infrared spectroscopic technique due to light scattering. Furthermore, information as to the content of each of the phases is lost. The tool that we proposed to solve these challenges consists of a pumping system that withdraws the emulsified biphasic mixture and, while inside the tubes constituting the apparatus, the mixture crashes into slugs which can be analyzed by Raman spectroscopy. Since the acquired data will be a random distribution of pure organic, aqueous, gaseous phases and mixtures of phases, an algorithm was also developed to group the data in 3 groups: organic, aqueous, discarded spectra allowing the data analysis almost instantaneously.

In Chapter 7 the partial synthesis of (S, S, S)-cyclotrisproline is reported using more modern methods compared to those reported previously in the literature. The final aim of this synthesis is to obtain the chiral ligand TPTACN (analogue of TMTACN) to be used to synthesize dinuclear

manganese complexes bearing many chiral centers to be employed as a probes to reveal mechanistic insight on the species that engage the substrate oxidation.

In conclusion, the spectroscopic and theoretical methods applied in this thesis show that such a combined approach is adept in explaining the mode of action of transition metal catalysts. Apart from the calculation of the thermodynamic feasibility of various pathways, the simulation of spectroscopic data proved to be a powerful tool to link the theoretical and experimental data, and allow for mutual validation. The conclusions arising from the use of both theory and spectroscopy have raised interesting variations in possible mechanisms by which non-heme iron complexes operate, and lay the ground work for a yet deeper computational study of the Fe(III)-OOH and –OCl species in their reaction with alkenes and other organic substrates. Furthermore the unexpected stability of the iron-dioxygen complex presents a challenge to spectroscopic efforts in observing such as species. The spectroscopic studies on the manganese dimers studied in this thesis would benefit form a similar approach to support mechanisms with computational studies and relate the presence bicarbonate/carbonate to the catalytic activation of Mn^{2+} and more importantly $[Mn(IV,IV)_2(\mu\text{-}O)_3(tmtacn)_2]^{2+}$. However, over and above the resources needed for such studies, the real challenge facing a computational approach is the lack of a good working model and a clear few of the nature of the catalytically active species.

Despite their mechanistic complexity, the application of such oxidation catalysts in more complex reaction conditions, i.e. two phase reactions, adds as many challenges to their study as they add opportunities for application. The validation of the methods developed in this thesis to monitor two phase reaction mixtures was realized, however, despite delivering the result (spectra of each phase with good time resolution), a key challenge is to recover information present in the large volume of discarded data. Further development should focus on practical aspects, e.g., using tubes with a decreased wall thickness or/and changing completely the acquisition method (e.g.: using a measurement chamber where the emulsion breaks into two phases) and /or improving the sorting algorithm with deconvolution algorithms to harvest further information from the normally discarded spectra.

Finally, the synthesis of the chiral TP-TACN ligand, although not completed, has been taken a step further through the use of modern methods albeit with the final and most challenging step remaining. Reduction of the cyclotrisproline with THF-BH_3 is the recommended next step as tests indicate (^{13}C-NMR spectroscopy) that no epimerization does not take place. The improvement of the purification procedure of the cyclization step would, most probably, increase the yield and the quality of the final product. Of course obtaining the ligand is only the first step of the next long chapter in understanding the chemistry of a remarkable catalyst - $[Mn(IV,IV)_2(\mu\text{-}O)_3(tmtacn)_2]^{2+}$.

Samenvatting

Bezint eer ge begint: dit Nederlandse spreekwoord zou het motto kunnen zijn voor het ethos van het werk wat beschreven is in dit proefschrift, waarin is gezocht naar een beter begrip van katalysatoren en de mechanismen waarmee deze katalysatoren functioneren. Het doel van deze exercitie is door middel van het toepassen van spectroscopische en theoretische technieken de mechanismen van twee klassen eerste-rij-overgangsmetaalcomplexen beter te kunnen begrijpen. Deze complexen voorzien in thermisch toegankelijke paden richting de activering van O_2, NaOCl en H_2O_2 voor de oxidatie van (an)organische substraten (oxidatiekatalyse).

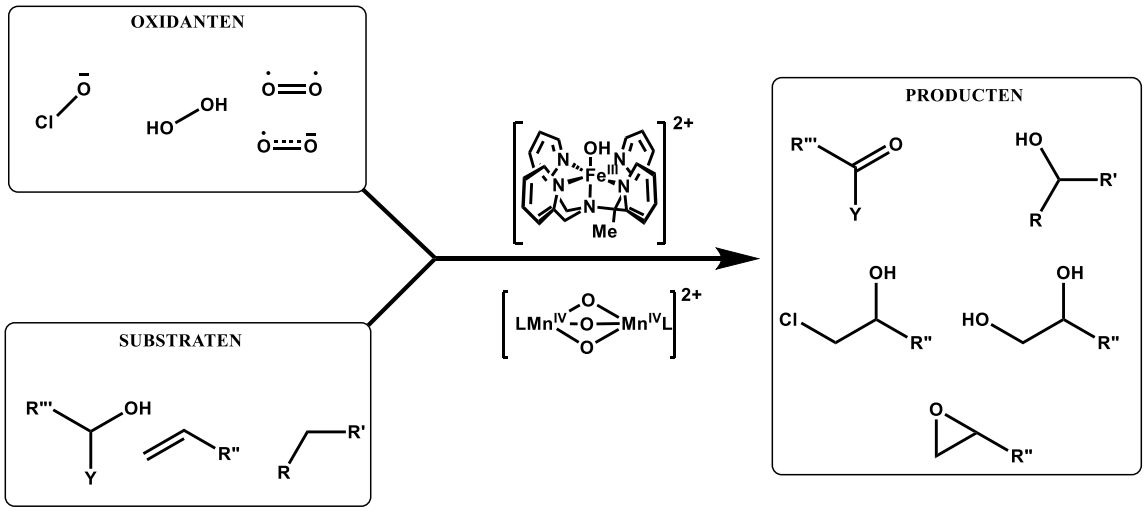

Figuur 5 Een algemeen overzicht van de reactiviteit van oxidatiekatalysatoren met oxidanten en organische substraten.

De studie naar overgangsmetalen met een gedeeltelijk gevulde d-schil is in het bijzonder uitdagend door hun spinactiviteit.

In hoofdstuk 1 worden de spectroscopische en theoretische technieken geïntroduceerd die gebruikt worden in dit proefschrift. De meest gebruikte spectroscopische technieken zijn Raman en resonantie Ramanspectroscopie gecombineerd met UV-vis absorptiespectroscopie. Ramanspectroscopie is een techniek die gebaseerd is op vibraties, wat betekent dat het informatie bevat over de structuur en bindingssterktes van een molecuul en in tegenstelling tot de gerelateerde infraroodspectroscopie (IR), het voordeel heeft toepasbaar te zijn in een breed scala van oplosmiddelen, in het bijzonder in waterige oplossingen. Het resonantie effect koppelt elektronische excitaties met deze vibratietoestanden. Daarom krijgen enkele van deze toestanden een signaal dat tientallen tot enkele duizenden keren versterkt wordt, wat de gevoeligheid van deze techniek verhoogd. De theoretische methode gebruikt in dit proefschrift bestaat, naast de vele post-Hartree-Fock methodes, exclusief uit dichtheidsfunctionaaltheorie (DFT). DFT heeft het grote voordeel dat het in de afgelopen decennia op grote schaal toegepast is bij berekeningen in het vakgebied van dit proefschrift vanwege de efficiëntie van de berekeningen ten opzichte van de nauwkeurigheid die ermee bereikt kan worden. In dit proefschrift is DFT gebruikt om moleculaire structuren te optimaliseren, om hun UV-vis

absorptie, IR, Raman, resonantie Raman en NMR spectra te voorspellen en voor het berekenen van de thermochemie van reacties.

In hoofdstuk 2 wordt de reactiviteit van de Fe(II) complexen van N4Py en MeN4Py (Figure 2) met waterstofperoxide en natriumhypochloriet in een waterige oplossing bestudeerd met DFT methodes. Deze ijzercomplexen worden gebruikt als voorbeeld om een beter begrip van de reactiviteit van ijzer gebaseerde enzymen te krijgen waaronder haloperoxidases en halogenases die in staat zijn organische stoffen te halogeneren. Uiteindelijk wordt verwacht dat dit onderzoek kan leiden tot het ontwerpen van selectieve en efficiënte katalysatoren voor een breed scala van reacties.

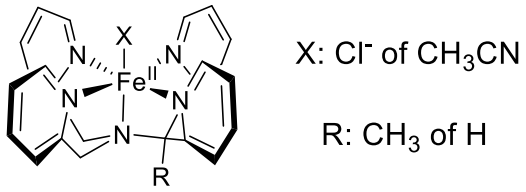

Figuur 6 Structuur van de [Fe(II)RN4Py-X]$^{2+}$ complexen waarvan de reactiviteit wordt beschreven in hoofdstuk 2.

De DFT studies werden dus gebruikt om resonantie Ramanspectra te simuleren om de toekenning te bevestigen van resonantie-versterkte vibratietoestanden zoals waargenomen in experimentele studies (waaronder ook de isotoop labeling met $H_2{}^{18}O_2/H_2{}^{18}O$), maar ook voor het bepalen van spintoestanden en thermochemie van de complexen en de bijbehorende reactanten gedurende alle tussenstappen van de reacties. De belangrijkste resultaten die uit deze DFT studies voortkomen is dat de resonantieversterking van Ramanspectra afhankelijk is van de spintoestand van de complexen, alsmede de vorming van een $Fe^{(IV)}$=O verbinding door homolytische splitsing van zowel het Fe(III) hypochloriet als het waterstofperoxide tussenproduct.

In hoofdstuk 3 wordt de studie naar de reactiviteit van Fe(II) complexen (besproken in het voorgaande hoofdstuk) met het zuurstof molecuul beschreven. Het belang van deze reactiviteit ligt in de overeenkomst met biologisch relevante ijzercomplexen die zuurstof activeren, en zich bezighouden met DNA-splitsing waardoor het invloed heeft op het replicatie van DNA en daardoor cellen beschadigt, in het bijzonder tumorcellen. Om deze redenen kan een beter begrip van het mechanisme van activatie van zuurstof door de complexen zoals afgebeeld in Figure 2, leiden tot de ontwikkeling van een nieuwe generatie antitumormedicijnen (chemotherapie). Het onderzoek, uitgevoerd met DFT berekeningen, start met de spintoestanden van de relevante complexen en de pH afhankelijkheid van de reactiviteit van het FeMeN4Py complex in water via twee mogelijke processen in de reactie met O_2 (d.w.z. buitenste-schil-elektronoverdracht vs. ligandvervanging, Figure 3). De studie onthulde een niet-verwaarloosbare thermodynamische voorkeur voor ligandvervanging ten opzichte van elektronoverdracht, maar liet ook zien dat er een klein energetisch verschil is tussen de twee reactiepaden.

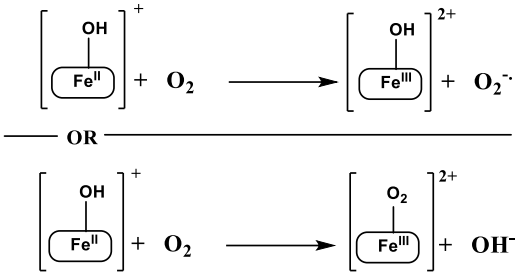

Figuur 7 Schema van de buitenste-schil-elektronoverdracht (boven) en de ligandvervanging (onder).

Bovendien is bepaald dat het FeMeN4Py-O_2 adduct, wat door het ligandvervangingsmechanisme wordt gevormd, zowel kinetisch als thermodynamisch de mogelijkheid heeft om de oxidatie van methanol tot formaldehyde uit te voeren en daarbij het paarse Fe(II)MeN4Py-OOH complex vormt.

In hoofdstuk 4 wordt een typisch soort complexen geïntroduceerd, gebaseerd op mangaandimeren en gebruikt in het industriële blekingsprocessen, en spectroscopisch bestudeerd in een organisch oplosmiddel (acetonitril). De reactie beschreven in dit hoofdstuk is de reductie van $[Mn(IV,IV)_2(\mu\text{-}O)_3(tmtacn)_2]^{2+}$ met H_2O_2 in de aanwezigheid van een carbonzuur (trichloorazijnzuur) om $[Mn\ (III, III)_2(\mu\text{-}O)(trichlooracetato)_2(tmtacn)_2]^{2+}$ te vormen (Figure 4).

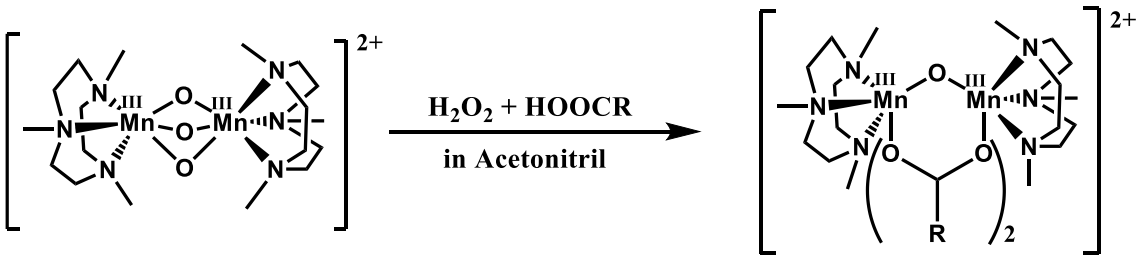

Figuur 8 Reductie van het $Mn(IV,IV)_2$ complex naar $Mn(III, III)_2$ in de aanwezigheid van waterstofperoxide en een carbonzuur.

Eerder was al geobserveerd dat tijdens de bovengenoemde transformatie de tussenproducten in het bijzonder actief zijn in de epoxidatie en cis-dihydroxylering van alkenen. Dit hoofdstuk bouwt hierop verder en levert gedetailleerde kennis over deze reactie door het ontrafelen van de autokatalytische aard van het tussenproduct dat actief is in de oxidatie van alkenen en in de disproportionering van H_2O_2. Daarnaast kon worden uitgesloten dat een van het ligand gescheiden Mn^{2+} of een Mn(II) dimeer met TMTACN liganden de actieve vorm kon zijn. Ook hierbij was een combinatie van UV-vis absorptie, Raman en resonantie Ramanspectroscopie de sleutel om de voorheen onverwachte reactie vast te stellen van de tussenproducten met H_2O_2 (disproportionering), wat concurreert met de directe oxidatie van het substraat.

In hoofdstuk 5 wordt het katalytische vermogen van $[Mn(IV,IV)_2(\mu\text{-}O)_3(tmtacn)_2]^{2+}$ en Mn^{2+} onderzocht waarbij gebruik werd gemaakt van Ramanspectroscopie in waterige oplossing, in uiteenlopende condities van onder andere verschillende pH's, katalysator concentraties, substraat concentraties en andere toevoegingen (bicarbonaat, boraat, acetaat, complexvormers). De uitgevoerde analyse van de concentratieveranderingen is essentieel om een beter begrip te krijgen van de veranderingen die de katalysator ondergaat tot de actieve vorm die verantwoordelijk is voor de alkeenoxidatie. Hoewel dit onderzoek niet de moleculaire

structuur oplevert van de actieve vorm van de katalysator die verantwoordelijk is voor de oxidatie, leidde het onderzoek wel tot de conclusie dat de competitieve activiteit van twee katalysatoren in acht genomen moet worden om de complexiteit van de geconstateerde afhankelijkheid van condities te kunnen begrijpen.

In hoofdstuk 6 is een methode ontwikkeld en getest voor het volgen van een twee-fase-reactie met behulp van Ramanspectroscopie. Om een zo goed mogelijk contact tussen de twee fasen te hebben, moet een twee-fase-reactie werken onder fijn-emulsie-condities. Zulke condities maken het verkrijgen van bruikbare spectra echter onmogelijk met elke zichtbare of infrarood spectroscopietechniek vanwege de verstrooiing van licht. Daardoor gaat bruikbare informatie over de samenstelling van beide fasen verloren. De methode die we hebben voorgesteld om deze uitdagingen op te lossen maakt gebruik van een pompsysteem dat de emulsie uit het twee-fase-mengsel opneemt en terwijl het door de buisjes stroomt waaruit het apparaat is opgebouwd, verandert het mengsel in een propstroom wat geanalyseerd kan worden met Ramanspectroscopie. Omdat de verworven gegevens een willekeurige spreiding hebben van puur organische, waterige en gasvormige fases en mengsels van fases is er een algoritme ontwikkeld om gegevens te splitsen in 3 verschillende groepen: organisch, waterig en verworpen spectra, waardoor de analyse van de gegevens vrijwel ogenblikkelijk gedaan kan worden.

In hoofdstuk 7 wordt de gedeeltelijke synthese van (S, S, S)-cyclotrisproline gerapporteerd, gebruik makende van moderne technieken in tegenstelling tot de eerder beschreven methodes in de literatuur. Het uiteindelijke doel van deze synthese is het verkrijgen van het chirale ligand TP-TACN (een analoog van TMTACN) dat gebruikt kan worden om een dimangaancomplex met vele chirale centra te synthetiseren om hiermee vervolgens meer inzicht te krijgen in het mechanisme van substraatoxidatie en de bijbehorende actieve vorm van de katalysator.

Samenvattend laten de in dit proefschrift gebruikte spectroscopische en theoretische technieken zien hoe deze gecombineerde aanpak is gebruikt om de actieve vorm van overgangs-metaalkatalysatoren te beschrijven. Naast de berekeningen van de thermodynamisch haalbare routes bleek de simulering van spectroscopische gegevens een krachtige methode om de theoretische en experimentele gegevens te verbinden en wederzijdse bevestiging te geven. De conclusies die getrokken kunnen worden door het gebruik van zowel theorie als spectroscopie hebben geleid tot interessante variaties in mogelijke mechanismes waarmee non-heem-ijzercomplexen functioneren, en hebben een basis gelegd voor een meer uitgebreide theoretische studie van de Fe(III)-OOH en –OCl complexen in de reactie met alkenen en andere organische substraten. Daarnaast gaf de onverwachte stabiliteit van het ijzer-zuurstofcomplex een uitdaging om deze met behulp van spectroscopische technieken waar te nemen. De spectroscopische studie naar het mangaandimeer wat in dit proefschrift is onderzocht, zal baat hebben bij een gelijksoortige aanpak om mechanismen te onderbouwen met behulp van theoretische studies en het verband te leggen tussen de aanwezigheid van bicarbonaat/carbonaat en de katalytische activiteit van Mn^{2+} en, nog belangrijker, $[Mn(IV,IV)_2(\mu\text{-}O)_3(tmtacn)_2]^{2+}$. Echter, behalve de benodigdheden voor zulk onderzoek is de echte uitdaging in theoretische studies het gebrek aan een goed werkend model en een duidelijk beeld van de werking van de actieve vorm van de katalysator.

Ondanks de complexiteit van het mechanisme geeft het gebruik van zulke oxidatie katalysatoren in complexere reacties, d.w.z. twee-fase reacties, net zoveel uitdagingen om te bestuderen als mogelijkheden voor toepassingen. De validatie van de in dit proefschrift ontwikkelde methodes om twee-fase reacties te volgen is gerealiseerd, echter ondanks positieve resultaten (spectra van beide fasen met goede tijdsresolutie) is de belangrijkste uitdaging het verkrijgen van informatie uit de grote hoeveelheid verworpen gegevens. Verdere ontwikkeling zou gefocust moeten worden op zowel de praktische aspecten, bijvoorbeeld het gebruik van buisjes met een kleinere wanddikte en het compleet veranderen van de dataverwervingstechniek (bijvoorbeeld het gebruik van een meetruimte waar de emulsie opbreekt in twee fasen), als op het analytische aspect door het verbeteren van het sorteringsalgoritme met deconvolutie-algoritmes om meer informatie uit de anders verworpen spectra te halen.

Ten slotte de synthese van het chirale TP-TACN ligand. Ondanks dat deze niet voltooid is, is het een stap verder gebracht door het gebruik van moderne technieken ook al is de laatste en moeilijkste stap nog te nemen. Reductie van cyclotrisproline met THF-BH_3 is de aanbevolen volgende stap aangezien proeven (^{13}C-NMR spectroscopie) hebben aangetoond dat er geen epimerisatie plaatsvindt. Het verbeteren van de zuiveringsprocedure na de ringvormingsstap zal hoogstwaarschijnlijk de opbrengst en de kwaliteit van het eindproduct verhogen. Daarnaast moet niet worden vergeten dat de synthese van het ligand slechts de eerste stap in een lange rij is om de chemie van een opmerkelijke katalysator $[Mn\ (IV,IV)_2(\mu\text{-}O)_3(tmtacn)_2]^{2+}$ beter te kunnen begrijpen.

Acknowledgements

The work described in this thesis wouldn't be possible without the contribution, assistance and support of the people mentioned in this section.

I start by thanking my PhD supervisor, Wesley, for giving me the opportunity to start and complete, with a very eclectic work programme, this PhD and for his help in improving my skills as a scientist and for his patience in listening to my sometimes verbose talking.

I thank Marcel Swart for the guidance I received over the years on DFT, for the functional S12g and for involving me in his present/future scientific projects. Many thanks also to Sam de Visser, Matt Quesne and Thom Pijper for guiding (over Chapter 2) and introducing me to the Density Functional Theory world in the first place.

My deepest gratitude to the STW team, in particular Andrew Dennis, Antoine Varagnat and Achim Lienke, for the insightful discussion on biphasic reaction monitoring with Raman, and to Ronald Hage and Hans de Boer for their encyclopaedic knowledge of all things manganese and iron related and their support over the last 5 years.

I thank the assessment committee, Prof. Maja Gruden, Prof. Christine McKenzie and Prof. Gerard Roelfes, for reading and approving this manuscript – the errors contained herein are mine of course but lessened by their comments.

Dear Sandeep and Federico, I greatly appreciate your enthusiastic acceptance to be my paranimphs for the defense of this thesis and for being over these past years, always at hand and supportive; thank you!

Of course a great working environment played also a central role in this thesis; therefore I thank dearly all my colleagues and the staff at the University of Groningen with whom I have interacted:
Shaghayegh, thanks for all the help and contributing both with your unending enthusiasm and experience on dinuclear manganese based catalysis. Pattama, thanks for proofreading this manuscript and together with Massimo thanks for granting me an enjoyable one and half year as your flat mate. Luuk, thank you for joining me in many challenges: in the electrochemistry lab as well in board games (on the latter one I keep myself well trained thanks to Irene). Duenpen, thanks a lot for the insightful discussion about Fe dimers and for teaching me how to see small differences that allow to avoid big mistakes! Dear Hans K., thank you for helping me translate my summary into Dutch and for being a great moral support in the last stages of the editing, I hope you enjoy the stay in Girona. Thank you Juan for your help in setting up the actinometry/quantum yield experiments and for all the scientific discussions we had on rRaman of $Fe^{(III)}$ species. Tjalling, thank you for being a nice fumehood mate (for a short but intense period) and for taking care and giving advice on good lab practice. Dear Francesco, it was fun and interesting for me to apply the Raman in flow monitoring to one of your $Mn^{(II)}$ picolinate catalysed reactions, thank you for collaborating on the setup of the conditions and for being a careful but easy-going lab supervisor – your own fumehood was more of warning than an example though. Dear Florian, thanks for your help in running the massive amount of

experiments, discussing results, and debating on the right data treatment procedures. Thanks Peter for keeping alive the unifying traditions of the group and for amazing and inspiring me with all the fluorescent compounds you synthesised. Appu, thanks for all the fruitful discussions we had on FeN4Py and for accompanying me the most (by coincidence) romantic places in the world. Many thanks go to the rest of the Brownies for maintaining such a good harmony and cooperativity in the lab as in the offices: Nikki, Hella, Heloise, Jorn, Vera, Kasper, Jia Jia, Emma and Oleksii. In this respect our group is a microcosm for the bigger family that is the Stratingh Institute for Chemistry. Of course we cannot live on the science of manganese and iron alone and I thank deeply Pieter, Cristina, Hilda, Alphons and Tineke for their kindness and solutions to my many logistical and administrative problems over the last 4 years.

Of course, I would not have made it to Groningen were it not for the support and encouragement of my relatives, and especially my parents: Aldo and Anna Bruna, for being of great support especially in the crucial moments. Thanks also to Massimo and Anna, for making me feel like I am in my home region (not only via the regional cuisine) even in the darkest and wettest days in Groningen.

Part of this manuscript was finalised during my time in Girona, and I thank the Institute for computational chemistry and catalysis (IQCC) for helping me make the change to a warmer climate and later lunch and for welcoming me into as friendly working environment as I left behind in Groningen.

Laura, although this book is dedicated fully to you, I would like still to leave the final words to you also. Thank you for always encouraging and supporting me since the moment we entered each other's lives; I will always keep in heart your encouragement and kind words